**Title**
Electron-impact ionization of atomic hydrogen



**Author**
Baertschy, Mark D.

**Publication Date**
2000-02-14

LBNL-45210


ERNEST ORLANDO LAWRENCE
BERKELEY NATIONAL LABORATORY

# Electron-Impact Ionization of Atomic Hydrogen

Mark D. Baertschy

**Computing Sciences Directorate**

February 2000

Ph.D. Thesis

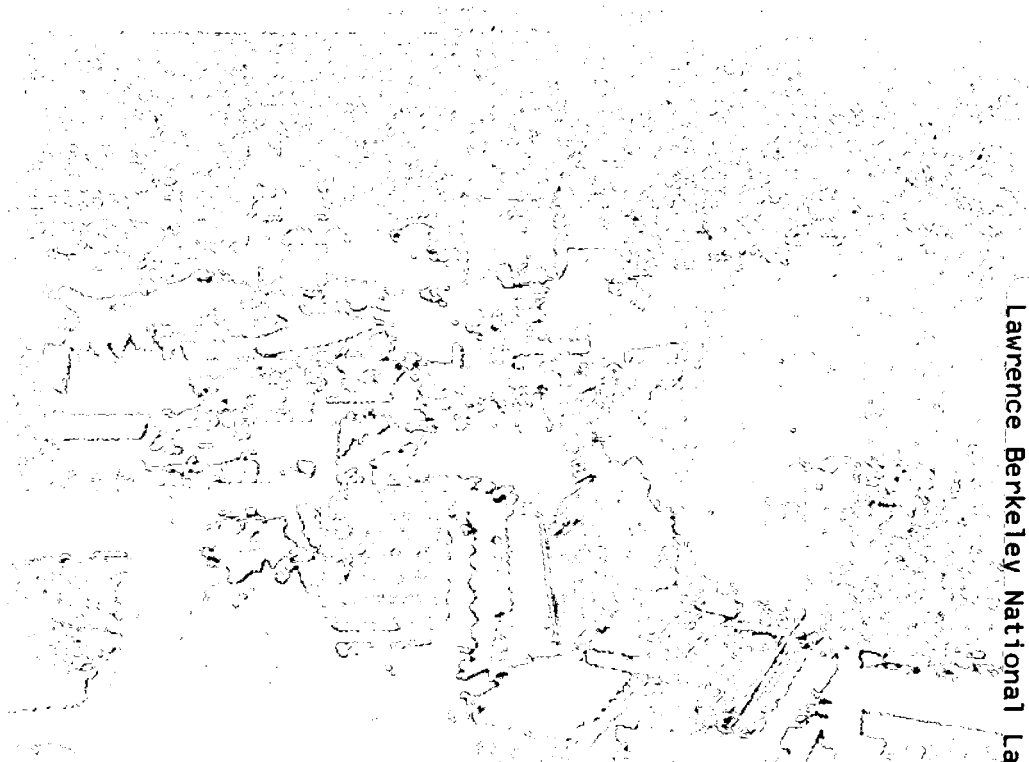

## DISCLAIMER

LBNL-45210

# Electron-Impact Ionization of Atomic Hydrogen

Mark D. Baertschy
Ph.D. Thesis

Department of Applied Science
University of California, Davis

and

Computing Sciences Directorate
Ernest Orlando Lawrence Berkeley National Laboratory
University of California
Berkeley, California 94720

February 2000

This work was supported by the LDRD and Assistant Secretary for Defense Programs at Lawrence Livermore National Laboratory, U.S. Department of Energy Contract No. W-7405-ENG-48, and printed by Ernest Orlando Lawrence Berkeley National Laboratory under Contract No. DE-AC03-76SF00098.

**Electron-Impact Ionization of Atomic Hydrogen**

by

MARK D. BAERTSCHY

B.S. (University of Puget Sound) 1994
M.S. (University of California at Davis) 1996

DISSERTATION
Submitted in partial satisfaction of the requirements for the degree of
DOCTOR OF PHILOSOPHY

in

Applied Science

in the

OFFICE OF GRADUATE STUDIES
of the
UNIVERSITY OF CALIFORNIA
DAVIS

Approved:

_____
Chair

_____

_____

Committee in Charge

2000

# Electron-Impact Ionization of Atomic Hydrogen



by

Mark D. Baertschy

Mark D. Baertschy

February 2000

Applied Science

Electron-Impact Ionization of Atomic Hydrogen

## Abstract

Since the invention of quantum mechanics, even the simplest example of collisional breakup in a system of charged particles, $\mathbf{e}^- + \mathbf{H} \rightarrow \mathbf{H}^+ + \mathbf{e}^- + \mathbf{e}^-$, has stood as one of the last unsolved fundamental problems in atomic physics. A complete solution requires calculating the energies and directions for a final state in which three charged particles are moving apart. Advances in the formal description of three-body breakup have yet to lead to a viable computational method. Traditional approaches, based on two-body formalisms, have been unable to produce differential cross sections for the three-body final state. Now, by using a mathematical transformation of the Schrödinger equation that makes the final state tractable, a complete solution has finally been achieved. Under this transformation, the scattering wave function can be calculated without imposing explicit scattering boundary conditions. This approach has produced the first triple differential cross sections that agree on an absolute scale with experiment as well as the first *ab initio* calculations of the single differential cross section [29].

Professor C. William McCurdy
Dissertation Committee Chair

To my parents
David and Donna Baertschy

# Contents

# List of Figures

# List of Tables

# Acknowledgements

First, I wish to acknowledge my two research advisers: Professor C. William McCurdy, LBNL Computing Sciences Directorate, and Dr. Thomas N. Rescigno, LLNL Physics Directorate. Together, they made my graduate experience both productive and enjoyable. Their guidance was essential to bringing this research to fruition and in preparing me for post-graduate work. My decision, five years ago, to work with them may prove to be one of the best of my career.

Dr. William A. Isaacs has been a valued colleague and friend at LBNL for the past three years. He provided much needed help at various stages along the way. I especially appreciate his assistance in deriving the more complicated finite difference formulas, helping me understand angular momentum, providing LaTeX pointers, and spending countless hours debugging.

This work could not have been completed without help from Dr. Xiaoye "Sherry" Li of NERSC. She provided a pre-release version of her SuperLU library routines for solving complex matrix equations. She also spent considerable time helping me incorporate them into my own application. Without SuperLU, these calculations would have been impossible. Also, Professor James Demmel of UC Berkeley provided some pointers on using iterative methods to solve linear systems.

Professor Anne E. Orel of the UC Davis Dept of Applied Science was an unofficial academic adviser throughout my graduate career. Other faculty and staff at the Department of Applied Science also provided academic and administrative support, particularly during my first few years as a graduate student.

Numerous staff at NERSC and LBNL helped me overcome various hardware and software difficulties, learn more about numerical linear algebra, and produce high-resolution graphics.

I should also mention Professor Alan Thorndike and Dr. Rand Worland of the Physics Department at the University of Puget Sound. They, along with other faculty and staff at UPS, provided me with a rich undergraduate experience which prepared me well for my graduate work.

Finally, I should acknowledge my family and friends outside of my graduate studies. Without them I might have become too one-dimensional. They provided timely escapes from the drudgery of my research and helped keep my life at least somewhat interesting. I especially appreciate those who have supported me in various ways and those who at least feigned an interest in my work. As we go our separate ways, let us never grow too far apart.

This work was carried out under the auspices of the US Department of Energy, primarily at the Lawrence Berkeley National Laboratory with support from Lawrence Livermore National Laboratory. Most computational resources were provided by the National Energy Research Scientific Computing center at LBNL. The ASCI Blue-Pacific machine at LLNL was also used.

# Chapter 1

# The Three-Body Nature of Electron-Impact Ionization

Electron-impact ionization is the process in which a target atom or molecule is ionized by a collision with an electron. Scattering theory calculations have progressed to the point of being able to accurately treat non-breakup processes for an electron scattering from relatively complicated target molecules. However, ionization represents a fundamentally different class of problems characterized by a final state in which three particles that interact via long-range Coulomb potentials are moving apart. Even the simplest example of this process, the electron-impact ionization of atomic hydrogen, has resisted numerical solution until now. This dissertation presents the first calculations to produce detailed information about electron-impact ionization that agrees, on an absolute scale, with experimentally measured values over a range of energies and final directions.

## 1.1 A three-body process in electron scattering

Collisions between electrons and atoms or molecules are governed by none of the selection rules that limit optical interactions with matter, primarily because the incident electron is indistinguishable from those of the target. Thus, electron impact is an efficient means of exciting or ionizing atoms and molecules. The relative probabilities of the elastic and various inelastic scattering processes following electron impact affect the energy distributions of atoms and molecules that determine the chemical dynamics of macroscopic systems. Furthermore, electron-impact ionization affects the populations of ions and free electrons and is the fundamental mechanism responsible for forming and sustaining low temperature plasmas. Detailed information about the energy and angular distributions of this process is important for understanding the dynamics of plasmas in a wide range of applications.

In a time-independent formalism the wave function simultaneously contains all the information for a scattering event initiated by a collision, at a particular energy, between an electron and the target in some specified initial state. Both the initial and final states are manifested in the asymptotic boundary conditions on the wave

function for large inter-particle separations. The objective of any scattering calculation is to obtain information about the final state following the collision. For electron scattering theory, this means determining the asymptotic boundary conditions of the wave function describing the motion of all electrons.

The final scattering state is typically analyzed in terms of individual "channel" components; each corresponding to a particular scattering process usually defined by the final state of the target. Scattering theory calculations and experimental measurements attempt to determine probabilities (expressed as scattering cross-sections) of the final state being in a particular channel. In calculations, we identify the channels by separating the asymptotic wave function into individual channel components each corresponding to a particular target state. Experimentally these channels are identified by the energy of the scattered electron and/or the state of the target.

Channels not corresponding to ionization are characterized by a single electron moving away from the target left behind in either the ground state or some excited state. Treatment of these "discrete" channels by various "two-body" formalisms, that specify the asymptotic form for each channel as two separate, non-interacting entities (the target atom or molecule and a free electron), has been possible for many years. Electron-impact ionization, on the other hand, is a three-body process characterized by two electrons separating from an ionized target.

The past 35 years have seen significant progress toward formulating an asymptotic form for this process, ranging from the early work of Rudge [34] and Peterkop [25] to the very cumbersome, but more complete, form derived by Alt *et al.* [1]. Despite this progress in the formal theory, efforts to explicitly use these asymptotic forms have not been successful. Consequently, complete numerical treatment of this process has continued to stand as an unsolved problem in electron-scattering theory.

## 1.2 Existing methods in scattering theory are designed for two-body processes

Scattering calculations are inherently more difficult than those for bound states with the same number of electrons because the wave functions that describe scattering extend over all space whereas the bound state wave functions are localized near the nucleus. Theoretical treatment of systems with two bound electrons began with the work of Hylleraas in the 1930s on the bound states of helium which were determined accurately by Pekeris in the late 1950s. Not until the 1961 work by Schwartz would even a rudimentary solution to the simplest two-electron scattering problem, an electron scattering from atomic hydrogen, be achieved.

For scattering of an electron from a target atom or molecule below the ionization threshold only two-body channels, characterized by one outgoing electron moving away from a neutral target, exist in the final state. In the elastic channel the outgoing electron has the same energy as the incident electron and the target is left behind in its original state. With the discrete excitation channels the outgoing electron has less energy than the incident electron and the target is left in some excited state. The

energy of the outgoing electron is limited to a set of discrete values that differ from the incident energy by the amount needed to raise the target to one of its excited states.

Below the ionization threshold the asymptotic wave function consists entirely of a finite set of discrete channels, corresponding to elastic scattering and electron-impact excitation, whose number is limited according to which target states are accessible with the energy available from the incident electron. These are referred to as the "open channels".

Calculations on electron-hydrogen scattering for the case where only a few channels are energetically allowed were carried out by Burke *et al.* [13] using the "close-coupling" method. This method uses a physically motivated expansion of the scattered wave function in terms of products of bound states and free-particle functions. If the expansion contains terms corresponding to every open channel then it can represent, exactly, the asymptotic wave function. By including additional short-range terms (corresponding to the closed channels) to form a more complete basis in the interaction region, accurate discrete channel cross sections could be calculated for scattering below the ionization threshold [17].

The expansion functions in close-coupling methods are obtained by diagonalizing the target Hamiltonian in some suitable numerical basis. As the numerical basis approaches completeness the negative eigenvalues converge to the physical bound state energies of the target and the corresponding eigenstates converge to the bound state wave functions. Diagonalization also produces eigenvalues not related to bound state energies. The corresponding eigenstates, known as "pseudostates", were thought to have no physical meaning themselves, but were included in close-coupling expansions to make the basis more complete. Pseudostates corresponding to positive eigenvalues are a discretization of what would be the continuum of free-particle states. However, since they come from representing the Hamiltonian in a set of finite-range basis functions they do not have infinite extent like true free-particle states.

In the early 1970's Burke and Mitchell [15, 14] showed that cross sections for the elastic and excitation channels could be calculated at energies above the ionization threshold by including positive-energy pseudostates in the expansion. This work was extended in the 1980's by Oza and Callaway [23, 22]. However, these calculations were marred by the presence of "pseudo-resonances" that prevented accurate calculations at certain energies. It was still broadly assumed that the positive-energy pseudostates did not give a meaningful representation of ionization. Therefore, they were used solely for improving the convergence of discrete channel cross sections and not for calculating information specific to electron-impact ionization.

In the early 1990's Bray and Stelbovics [10, 11] showed that by including increasing numbers of positive-energy pseudostates a "convergent" close-coupling (CCC) method, that eliminated the pseudo-resonances, could be developed for calculating not only discrete channel cross sections but total ionization cross sections as well. This method represented a significant step forward in treating electron scattering above the ionization threshold and has been applied successfully to atoms with several electrons. However, the CCC method has fallen short in its ability to provide details

about ionization such as how energy is shared between the two scattered electrons.

## 1.3 An entirely new approach designed to correctly treat ionization

In a sense, the ionization component of electron-hydrogen scattering contains a continuously infinite number of "channels" because the total available energy is shared continuously between the two free electrons. Consequently, ionization cannot be satisfactorily represented by a discrete sum of products of one-electron functions. In particular, two-body formalisms, such as CCC which attempts to attach physical meaning to positive-energy pseudostates, fail to accurately calculate information about how energy is shared between the two electrons. The difficulty lies in the intractable nature of the scattering boundary conditions for ionization. We will look more closely at the difficulties of representing ionization boundary conditions with the convergent close-coupling method in Chapter 2.

The failure of CCC, and other methods based on specifying the asymptotic form of the wave function, to accurately calculate detailed information about ionization points to the need for an entirely new formalism that does not require knowledge of the wave function's asymptotic form. The method of exterior complex scaling completely avoids the difficulties associated with the asymptotic form for ionization by using a mathematical transformation of the Schrödinger equation that simplifies the scattering boundary conditions so that the wave function can be calculated using standard numerical methods. Exterior complex scaling is introduced, in Chapter 3, within the context of a two-dimensional model of electron-hydrogen scattering that retains many of the numerical pathologies associated with ionization.

A method for calculating detailed ionization information for the model problem by analyzing the wave functions from Chapter 3 is introduced in Chapter 4. It is shown that wave functions calculated with exterior complex scaling produce energy-sharing differential cross sections that do not have the unphysical characteristics of the corresponding CCC results. Extension of the methods introduced in Chapter 3 to the full electron-hydrogen scattering problem is described in Chapter 5. By using exterior complex scaling, six-dimensional wave functions that include an ionization component are produced. Differential ionization cross sections, extracted from these wave functions by a procedure similar to the one described in Chapter 4, are presented in Chapter 6. These results are the first-ever differential cross sections for electron-impact ionization that agree, on an absolute scale, with experimentally determined values over a range of energies and directions.

# Chapter 2

# Barriers to Two-Body Reductions of Three-Body Breakup

Components of the wave function corresponding to elastic and excitation channels for scattering of an electron from a hydrogen atom have the asymptotic form of products of one-electron functions. This fact led to the development of several "two-body" formalisms for treating electron scattering from atoms and molecules. These methods have been able to calculate cross sections for discrete channels at collision energies both above and below the ionization threshold. The convergent close-coupling method, which is limited to atoms, also has succeeded in calculating *total*, but not *differential* cross sections for ionization. This inability to correctly describe the details of electron-impact ionization, such as the distribution of energy between the two outgoing electrons, indicates a fundamental problem with using two-body formalisms to describe a three-body final state.

## 2.1 Electronic collisions with hydrogen in a time-independent formalism

Although scattering is an intrinsically time dependent process, the interactions, themselves, depend only on distances and not explicitly on time. So, we can calculate complete scattering information using time-independent methods. The wave function $\Psi^+$ that describes the electron-hydrogen collision is the solution to the time-independent Schrödinger equation with appropriate boundary conditions.

$$\hat{H}\Psi^+ = E\Psi^+ \tag{2.1}$$

We will be considering an electron with momentum $\hbar k_i$ colliding with a hydrogen atom in its ground state so the total energy $E$ is the sum of the incident energy and the ground state energy $\varepsilon_1$ of hydrogen.

$$E \equiv \frac{\hbar^2}{2m}k_i^2 + \varepsilon_1 \tag{2.2}$$

By approximating the nucleus as infinitely massive, the Hamiltonian $\hat{H}$ describes the motion of only the two electrons. Their positions, relative to the nucleus, are denoted by two three-dimensional vectors $\vec{r}_1$ and $\vec{r}_2$. The wave function $\Psi^+(\vec{r}_1, \vec{r}_2)$ is a six dimensional function and the Hamiltonian, defined below, is a six dimensional differential operator.

$$\hat{H}(\vec{r}_1, \vec{r}_2) = -\frac{\hbar^2}{2m}\nabla_1^2 - \frac{\hbar^2}{2m}\nabla_2^2 - \frac{e^2}{r_1} - \frac{e^2}{r_2} + \frac{e^2}{|\vec{r}_1 - \vec{r}_2|} \tag{2.3}$$

The symbols $\nabla_1^2$ and $\nabla_2^2$ are the three-dimensional Laplacians for the coordinates $\vec{r}_1$ and $\vec{r}_2$ and represent the kinetic energies of the two electrons. The three particles interact via an attractive Coulomb potential between the nucleus and each electron and a repulsive Coulomb potential between the two electrons.

Electrons are indistinguishable, spin-$\frac{1}{2}$ particles so the overall wave function of both space and spin coordinates must be anti-symmetric with respect to interchange of the two electrons. Total spin $S$ of the system can be either zero or one. The "singlet" $S = 0$ spin eigenfunction is anti-symmetric while the three "triplet" $S = 1$ spin eigenfunctions are symmetric. Thus, the proper symmetry for the spatial wave function under interchange of electron coordinates is $\Psi^+(\vec{r}_2, \vec{r}_1) = (-1)^S \Psi^+(\vec{r}_1, \vec{r}_2)$. Since the Hamiltonian in Equation 2.3 does not depend on spin we can perform independent calculations for the singlet and the triplet cases. The $S$ index is usually suppressed, so it is to be understood that separate calculations are always performed for both spin symmetries. Ultimately, we will sum the results for the two values of $S$ with statistical weights of $\frac{1}{4}$ for singlets and $\frac{3}{4}$ for triplets.

Both the initial and final states are described in the asymptotic region of the wave function. The first step in simplifying the asymptotic boundary conditions for $\Psi^+$ is to remove a term $\Psi^0_{k_i}$, representing the initial state, from the total wave function leaving a function $\Psi^+_{\text{sc}}$ that is identified, asymptotically, as the scattered wave.

$$\Psi^+(\vec{r}_1, \vec{r}_2) = \Psi^0_{k_i}(\vec{r}_1, \vec{r}_2) + \Psi^+_{\text{sc}}(\vec{r}_1, \vec{r}_2) \tag{2.4}$$

We specify the initial state to be one electron in the hydrogen ground state $\Phi_{1s}(\vec{r})$ and the other to be a plane wave $e^{ik_i z}$ with momentum $\hbar k_i$ in the $\hat{z}$ direction.

$$\Psi^0_{k_i}(\vec{r}_1, \vec{r}_2) = \frac{1}{\sqrt{2}}\left(\Phi_{1s}(\vec{r}_1)e^{ik_i z_2} + (-1)^S \Phi_{1s}(\vec{r}_2)e^{ik_i z_1}\right) \tag{2.5}$$

To preserve the indistinguishability of the electrons, the initial state $\Psi^0_{k_i}$ is anti-symmetrized according to the total spin $S$.

We derive an inhomogeneous differential equation for $\Psi^+_{\text{sc}}(\vec{r}_1, \vec{r}_2)$ in terms of the known function $\Psi^0_{k_i}(\vec{r}_1, \vec{r}_2)$ by rearranging the Schrödinger equation (Equation 2.1).

$$\left(E - \hat{H}\right)\Psi^+_{\text{sc}}(\vec{r}_1, \vec{r}_2) = \left(\hat{H} - E\right)\Psi^0_{k_i}(\vec{r}_1, \vec{r}_2) \tag{2.6}$$

Since $\Psi^+_{\text{sc}}(\vec{r}_1, \vec{r}_2)$ represents the scattered part of the wave function at large distances it must be an outgoing wave in $r_1$ and $r_2$. Thus, we define $\Psi^+_{\text{sc}}(\vec{r}_1, \vec{r}_2)$ to be the outgoing solution to Equation 2.6.

## 2.2 Analyzing the asymptotic form of the scattered wave

We can separate the scattered wave into individual "channel" components that are identified according to the final state of the hydrogen atom. Hydrogen states can be written as $\Phi_{nlm}(\vec{r}) = \frac{1}{r}\phi_{nl}(r)\mathrm{Y}_{l,m}(\hat{r})$ where the $\mathrm{Y}_{l,m}$ is a spherical harmonic and $l$ and $m$ are the usual angular momentum quantum numbers. The functions $\phi_{nl}$ satisfy the radial Schrödinger equation for hydrogen with Hamiltonian $\hat{H}_l$ and energy $\varepsilon_n$.

$$\hat{H}_l(r) \equiv \left(-\frac{\hbar^2}{2m}\frac{d^2}{dr^2} + \frac{l(l+1)\hbar^2}{2mr^2} - \frac{\mathrm{e}^2}{r}\right) \tag{2.7}$$

Bound states of hydrogen are those $\Phi_{nlm}$ that are finite-range and have an energy that is one of the discrete values $\varepsilon_n = -\frac{13.6}{n^2}\mathrm{eV}$. The ground state, previously denoted by $\Phi_{1s}$, is $\Phi_{100}$ in this notation.

In the elastic scattering channel one electron is left bound in the hydrogen ground state while the other scatters away. Since no energy was exchanged in the collision the scattered electron will have the same energy as the incident electron. In the excitation channels one electron is left bound to the proton in some excited hydrogen state. The momentum $\hbar k_n$ of the outgoing electron is reduced according to the amount of energy required to raise the atom to its excited state. Since the bound state energies are quantized, the scattered momenta $\hbar k_n$ in the elastic and excitation channels are limited to a discrete set of values.

$$\frac{\hbar^2}{2m}k_n^2 = \frac{\hbar^2}{2m}k_i^2 + \varepsilon_1 - \varepsilon_n \tag{2.8}$$

For scattering below the ionization threshold *i.e.*, $\frac{\hbar^2}{2m}k_i^2 < |\varepsilon_1|$, the number of discrete channels that are "open" are limited to those for which the quantity $\frac{\hbar^2}{2m}k_n^2$, defined in Equation 2.8, is positive. In this case, the asymptotic form of the scattered wave is completely described by an expansion in terms of two-body functions, each corresponding to an energetically open channel.

$$\Psi_{\mathrm{sc}}^{+}(\vec{r}_1,\vec{r}_2) \underset{r_1,r_2\to\infty}{\longrightarrow} \sum_{n,l,m}\frac{1}{\sqrt{2}}\left(\Phi_{nlm}(\vec{r}_1)\frac{f_{nlm}(\hat{r}_2)}{r_2}e^{ik_ir_2} + (-1)^S\frac{f_{nlm}(\hat{r}_1)}{r_1}e^{ik_ir_1}\Phi_{nlm}(\vec{r}_2)\right) \tag{2.9}$$

In every term the scattered electron is represented by a radially outgoing wave with angular dependence determined by the channel scattering amplitude $f_{nlm}(\hat{r})$.

Equation 2.9 does not completely describe the asymptotic form of $\Psi_{\mathrm{sc}}^{+}$ for scattering above the ionization threshold. In this case, all excitation channels are open so the asymptotic form is an infinite sum over all $n$. More importantly, ionization is now possible so an additional term, $\Psi_{\mathrm{ion}}^{+}(\vec{r}_1,\vec{r}_2)$, must be included to describe ionization.

$$\Psi_{\mathrm{sc}}^{+}(\vec{r}_1,\vec{r}_2) \underset{r_1,r_2\to\infty}{\longrightarrow} \sum_{n,l,m}\frac{1}{\sqrt{2}}\left(\Phi_{nlm}(\vec{r}_1)\frac{f_{nlm}(\hat{r}_2)}{r_2}e^{ik_ir_2} + (-1)^S\,(1\longleftrightarrow 2)\right) + \Psi_{\mathrm{ion}}^{+}(\vec{r}_1,\vec{r}_2) \tag{2.10}$$

The ionization "channel" is really a continuum of final states that cannot be satisfactorily represented by a discrete sum of products of one-electron functions.

Many efforts have been made to derive the asymptotic form of $\Psi^+_{\rm ion}$, with the work of Alt *et al.* [1] being the most complete to date. We will, instead, look at the relatively simple form derived by Rudge [34] that is valid when *all three* particles are widely separated. This form is expressed in terms of hyperspherical coordinates where the two radial coordinates $r_1$ and $r_2$ are replaced by a hyperradius $\rho = \sqrt{r_1^2 + r_2^2}$ and a corresponding hyperangle $\alpha = \tan^{-1}(r_2/r_1)$.

$$\Psi^+_{\rm ion}(\vec{r}_1, \vec{r}_2) \underset{\rho\to\infty}{\longrightarrow} - f_i(\hat{r}_1, \hat{r}_2, \alpha)\sqrt{\frac{i\kappa^3}{\rho^5}} e^{i[\kappa\rho + (\zeta(\hat{r}_1,\hat{r}_2,\alpha)/\kappa)\ln(2\kappa\rho)]} \tag{2.11}$$

In Equation 2.11, the angular function multiplying the logarithmic phase is defined as $\zeta(\hat{r}_1, \hat{r}_2, \alpha) = (\sin\alpha)^{-1} + (\cos\alpha)^{-1} - (1 - \hat{r}_1 \cdot \hat{r}_2 \sin 2\alpha)^{-1/2}$. The scattering amplitude for ionization $f_i(\hat{r}_1, \hat{r}_2, \alpha)$ contains all of the angular distribution (the $\hat{r}_1, \hat{r}_2$ dependence) and energy sharing (related to the $\alpha$ dependence) information about the ionization final state. Equation 2.11 describes the asymptotic form of $\Psi^+_{\rm ion}$ as an outgoing wave in the hyperradius $\rho$ rather than in the two radial coordinates. This very fact indicates that $\Psi^+_{\rm ion}$ cannot be adequately represented by a finite sum of two-body terms *i.e.*, products of a function of $\vec{r}_1$ and a function of $\vec{r}_2$.

## 2.3 Two-body approach to calculating integral cross sections for ionization

The convergent close-coupling (CCC) method is a particular implementation of close-coupling that has been successfully applied to calculating discrete channel cross sections for electron-atom scattering over a wide range of energies. CCC does not correctly treat the details of ionization [30] but still has remarkable success at calculating *total* ionization cross sections, as well as cross sections for discrete channels, in atoms of several electrons [2]. In order to understand the shortcomings of CCC at calculating detailed ionization information we will look briefly at a simplified application of CCC specific to hydrogen [9].

Like all close-coupling formalisms, the CCC method is based upon a physically motivated expansion of the wave function. This expansion is in terms of products of one-electron functions similar to Equation 2.9, but the actual hydrogen states are replaced by functions $\Upsilon_{nlm}(\vec{r})$, called pseudostates. The $\Upsilon_{nlm}$ are generated by diagonalizing the hydrogen Hamiltonian represented in a set of square-integrable numerical basis functions.

$$\left(-\frac{\hbar^2}{2m}\nabla^2 - \frac{e^2}{r}\right)\Upsilon_{nlm}(\vec{r}) = \lambda_{nl}\Upsilon_{nlm}(\vec{r}) \tag{2.12}$$

As the size of the numerical basis is increased the negative eigenvalues and corresponding pseudostates in Equation 2.12 converge to the bound state energies and eigenfunctions of hydrogen *i.e.*, $\lambda_{nl} \approx \varepsilon_n$ and $\Upsilon_{nlm}(\vec{r}) \approx \Phi_{nlm}(\vec{r})$.

Within the CCC formalism, the wave function $\Psi^+_{\rm CCC}$ is expanded, analogously to Equation 2.9, in terms of the $\Upsilon_{nlm}$ rather than exact hydrogenic functions. The number of terms that are included in the expansion is increased until convergence of the cross-sections is observed.

$$\Psi^+_{\rm CCC}(\vec{r}_1,\vec{r}_2) = \sum_{n,l,m} \left( \Upsilon_{nlm}(\vec{r}_1) f^S_{nlm}(\vec{r}_2) + (-1)^S f^S_{nlm}(\vec{r}_1) \Upsilon_{nlm}(\vec{r}_2) \right) \tag{2.13}$$

The CCC expansion coefficients $f^S_{nlm}(\vec{r})$ for all energetically open ($\lambda_{nl} < E$) pseudostate channels have the asymptotic form of an outgoing wave similar to the individual terms in Equation 2.9. In the actual implementation, $\Psi^+_{\rm CCC}$ approximates the *total* wave function $\Psi^+$ rather than the scattered wave $\Psi^+_{\rm sc}$. This has little consequence on the discussion here since both the total and scattered wave functions can be expanded similarly with only the elastic channel terms being different.

Pseudostates with positive eigenvalues are a sort of discretization of the continuum of Coulomb waves representing the ionized hydrogen states. These positive-energy pseudostates, unlike true continuum functions, are finite-range because the underlying numerical basis is square-integrable. Although they do not, themselves, have physical meaning, the positive-energy pseudostates do "overlap" with true Coulomb waves. From a numerical point of view, all pseudostates, including those corresponding to closed channels and those with positive eigenvalues, must be included in the CCC expansion to form a complete set of basis functions.

Like other close-coupling formalisms, CCC is essentially exact below the ionization threshold. It can also produce accurate discrete channel cross sections for scattering at higher energies. The advantage of CCC over earlier close-coupling methods is that it has been shown to also produce convergent total ionization cross sections [10]. Convergence of the total ionization cross sections was considered by some to be a surprising result since ionization must be represented by the positive-energy terms in the pseudostate expansion and those were believed to have no physical meaning. However, success at calculating total ionization cross sections does not necessarily require that the the CCC basis accurately describe the details of the ionization component of the scattered wave.

The success of CCC in calculating total ionization cross sections is a consequence of the ability of the expansion to both represent, exactly, each of the discrete channel components of the wave function in the asymptotic region and to accurately describe the *entire* wave function within a finite interaction region. With an expansion basis that is effectively complete over the interaction region, we can assume that the CCC formalism is properly representing all of the collision dynamics. Since each energetically open term in the expansion is constructed to be an outgoing wave we know that any outgoing flux generated in the interaction region will successfully escape to infinity. Therefore, it is not as surprising as originally believed that the CCC method can calculate accurate *total* cross sections. Since we already know that the CCC method can accurately calculate discrete channel cross sections it is clear that by simply subtracting all discrete channel cross sections from the total cross section we can obtain a reasonably accurate estimate of the total ionization cross section.

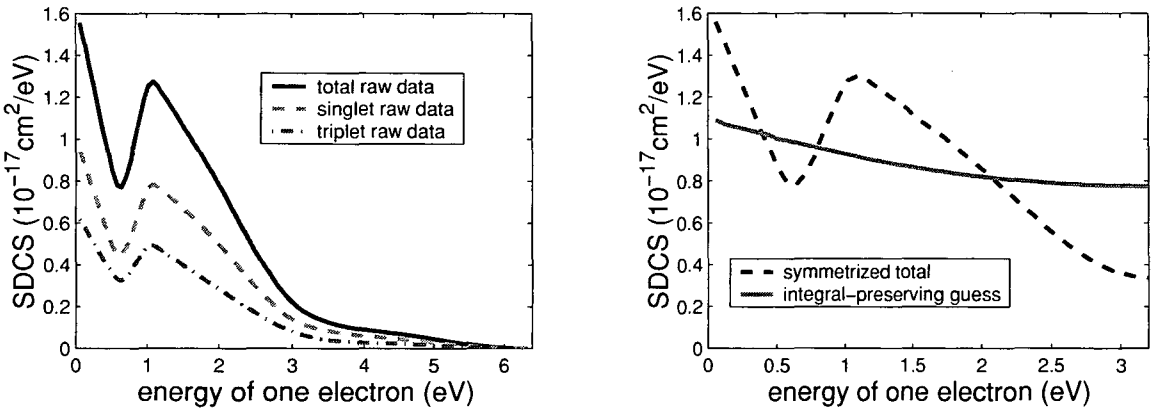


Figure 2.1: SDCS for e-H calculated by CCC at 20eV incident energy, so that the total energy is E=6.4eV. The actual calculated cross sections, which are not symmetric about E/2, are shown on the left. The total "raw" cross section is the sum of the singlet and triplet "raw" cross sections. A symmetrized SDCS is formed by adding the raw total to its mirror image. The CCC method removes the unphysical oscillations in the calculated cross sections by replacing the symmetrized SDCS with a smooth, integral-preserving guess.

## 2.4 Two-body approaches fail to provide detailed ionization information

Shortcomings of the CCC method in treating ionization are most evident in the energy-sharing or single differential cross section (SDCS) for ionization. The SDCS is a differential cross section with respect to the energy of one of the electrons $\varepsilon_1$ and describes how energy is shared between the two outgoing electrons. The energy $\varepsilon_1$ can range from zero to the total energy $E$. Because the two electrons are indistinguishable the SDCS should have the same value at $E - \varepsilon_1$ as at $\varepsilon_1$. It is, therefore, symmetric about $\varepsilon_1 = E/2$. By convention, the SDCS is normalized so that it gives the total ionization cross section when integrated from zero to $E/2$. An example SDCS calculated by Igor Bray with the CCC method [12] is plotted in Figure 2.1. The actual calculated cross sections are shown in the left panel. Two striking features of these curves are (1) they are definitely not symmetric about $E/2$ and (2) they contain large amplitude oscillations.

The asymmetry of the calculated SDCS is a consequence of the way the wave function is analyzed [30]. In the CCC method physical meaning is attached to the terms in the expansion with pseudostates $\Upsilon_{nlm}$ for which $0 < \lambda_{nl} < E$. Each of these terms is said to correspond to one electron being ejected from the target with energy $\lambda_{nl}$ and the other scattering away from the target with energy $E - \lambda_{nl}$. The SDCS is constructed over the continuous range of $\varepsilon_1$ by applying appropriate quadrature weights to the discrete set of positive pseudostate energies [8]. Since the scattered electron is actually represented in these terms by a plane wave, this assertion is based on the rather gross assumption that the slower, ejected electron completely shields the

nucleus from the faster, scattered electron. There is some controversy in the literature over whether the asymmetric method of extracting the SDCS in the CCC method imposes distinguishability of the two electrons [5], but it is claimed by Bray [7] that this issue is addressed by post-symmetrizing the result.

The more troubling aspect of the SDCS calculated by CCC is the oscillations. Since the true SDCS is known to be a very smooth function, Bray constructs a smooth curve, shown in the right panel of Figure 2.1, that is an integral-preserving average of the symmetrized oscillatory curve. It is claimed that this curve approximates what the CCC calculated SDCS would converge to in the limit of an infinite CCC basis [6]. Convergence of the calculated SDCS to a smooth function has never been demonstrated and there is much uncertainty about whether the smooth curve generated in this *ad hoc* fashion is correct. It is widely believed that the oscillations in the SDCS calculated by CCC indicate a fundamental problem with the formalism.

Looking for the source of the unphysical oscillations requires scrutinizing the ability of the CCC basis to adequately describe the ionization component of the scattered wave. The set of negative-energy pseudostates in the CCC expansion (Equation 2.13) generate the discrete channel terms in the expansion of the asymptotic form (Equation 2.10). It is then up to the positive-energy pseudostate terms to construct the ionization component in Equation 2.10. This is potentially a source of trouble in two ways. First, and most obvious, is the possibility that the CCC basis cannot adequately represent the ionization component of the scattered wave at large distances. Second, and probably most significant, is the way that the CCC wave function is analyzed by attaching physical meaning to the positive-energy pseudostates.

From the Rudge asymptotic form (Equation 2.11) it is clear that the ionization component is an outgoing wave in the hyperradius $\rho$. The positive-energy terms in Equation 2.13, on the other hand, are an outgoing wave for one electron (the required asymptotic form of $f^S_{nlm}$) and a positive-energy pseudostate for the other. It is claimed that in the limit of an infinite set of numerical basis functions we can think of the positive-energy pseudostates as true Coulomb waves. Even in this idealized case we have a task similar to trying to represent a spherical wave with a sum of products of plane waves. As the number of plane wave products increases the spherical wave will be represented fairly well over an increasingly large region of space. However, forming a spherical wave, in this manner, that is accurate over all space is a hopeless task. Knowing the asymptotic form of the wave function is effectively the ultimate goal of scattering calculations, so there is legitimate concern about the ability of the CCC basis to adequately represent the ionization component of the scattered wave.

The CCC method certainly has trouble correctly representing the ionization component of the scattered wave. It is conceivable, although by no means certain, that with a sufficiently large CCC basis the wave function may be adequately constructed over a large enough region of space to produce meaningful ionization information. However, there is still a problem with the analysis because the product of a plane wave and a Coulomb wave is not a very good representation of a state with two electrons in the continuum. Although the CCC basis could conceivably be used as an adequate numerical basis it is incorrect to attach physical meaning to the individual

positive-energy pseudostate terms. Another problem is that this analysis implicitly treats the electrons as distinguishable.

In a recent study [30] the effects of the CCC energy analysis for ionization were examined in isolation from other potential sources of error. Accurate scattering wave functions that contain an ionization component were constructed using the method presented in Chapter 3, thus removing the uncertainties associated with constructing a CCC wave function. These wave functions were constructed for several two-dimensional model problems and smooth, accurate single differential cross sections were extracted from them by using the method described in Chapter 4. However, a CCC style analysis produced oscillatory cross sections similar to those in the left panel of Figure 2.1. It was shown that, at least for examples with short range potentials, the CCC calculated SDCS at $\varepsilon_1 = E/2$ converges to exactly one fourth of the correct value. Although no formal proof has been given, it appears that this is at least approximately the case for electron-hydrogen scattering. However, the relationship between the CCC calculated SDCS and the correct SDCS for all other energy distributions is completely unpredictable.

The two-body formalism of CCC is very well suited for discrete channels, but not for ionization. Its shortcomings point to the need for an entirely new formalism to calculate differential cross sections for ionization that is not tied to *any* particular asymptotic form. The method of exterior complex scaling, introduced in the next chapter, can produce scattering wave functions that are accurate over a finite region of space and correctly describe the details of ionization without appeal to any asymptotic form. In Chapter 4, a procedure is introduced that extracts differential cross sections for ionization from these wave functions, again, without explicitly invoking any particular asymptotic form.

# Chapter 3

# Exterior Complex Scaling Avoids the Three-Body Asymptotic Form

The fundamental difficulty that traditional, "two-body" methods have with electron-impact ionization is in representing a wave function with two outgoing electrons. These methods have the same difficulty even when applied to the two-dimensional Temkin-Poet model of electron-hydrogen scattering that also supports an "ionization" final state with two electrons in the continuum. This model presents difficulties similar to those of the full problem of electron-hydrogen scattering. It is, therefore, a useful test-bed for any method intended to be applied to a true electron-impact ionization problem. Thus, the Temkin-Poet model is an ideal context for presenting the method of exterior complex scaling as a means of generating wave functions for electron-hydrogen scattering while avoiding, entirely, the difficulty in specifying the Coulomb three-body asymptotic form.

## 3.1 Temkin-Poet Model Problem

The $S$-wave, or Temkin-Poet, model of electron-hydrogen scattering has been used for many years to develop and test calculational methods intended for more realistic electron-scattering problems. This two-dimensional problem, that supports ionization, was first presented in 1962 by Aaron Temkin [38] in a variational study of the $S$-wave component of electron-hydrogen scattering. In 1978, R. Poet [26] produced the first accurate cross-sections for inelastic processes in the model. Just like the complete electron-hydrogen system, this model contains an infinite number of bound states as well as an ionization continuum, but without the complexities of angular dependence. Therefore, it allows one to isolate and study the difficulties arising from the radial dependence of three-body breakup.

The Temkin-Poet model can be thought of as a spherical average of the full electron-hydrogen problem. It is defined by a two-dimensional, radial Schrödinger equation.

$$\hat{H}(r_1, r_2)\psi^+(r_1, r_2) = E\psi^+(r_1, r_2) \tag{3.1}$$

The total energy $E$ is the sum of the kinetic energy of the incident electron and the

ground state energy of hydrogen *i.e.*, $E = \frac{\hbar^2}{2m}k_i^2 + \varepsilon_1$. With no angular dependence, the Laplacians from the Hamiltonian in Equation 2.3 reduce to second derivatives with respect to the two radial coordinates.

$$\hat{H}(r_1, r_2) \equiv -\frac{\hbar^2}{2m}\frac{d^2}{dr_1^2} - \frac{\hbar^2}{2m}\frac{d^2}{dr_2^2} - \frac{e^2}{r_1} - \frac{e^2}{r_2} + \frac{e^2}{r_>} \tag{3.2}$$

The quantity $r_>$ is defined below.

$$r_> \equiv \begin{cases} r_1, & r_1 > r_2 \\ r_2, & r_1 < r_2 \end{cases} \tag{3.3}$$

The attractive potentials between the nucleus and each electron are the same in the model Hamiltonian as they are in Equation 2.3. The repulsive potential between the two electrons is replaced by a non-analytic potential $\frac{e^2}{r_>}$ which is the zero angular momentum term in the multipole expansion of $\frac{e^2}{|\vec{r}_1 - \vec{r}_2|}$ (see Equation F.13). Just as in Equation 2.4 we separate the wave function $\psi^+$ in to two terms: $\psi^0_{k_i}$ representing the initial state and $\psi^+_{\mathrm{TP}}$ having outgoing wave boundary conditions.

$$\psi^+(r_1, r_2) = \psi^0_{k_i}(r_1, r_2) + \psi^+_{\mathrm{TP}}(r_1, r_2) \tag{3.4}$$

The Temkin-Poet scattered wave, $\psi^+_{\mathrm{TP}}$, is the outgoing wave solution to a scattered wave equation similar to Equation 2.6.

$$\left(E - \hat{H}(r_1, r_2)\right)\psi^+_{\mathrm{TP}}(r_1, r_2) = \left(\hat{H}(r_1, r_2) - E\right)\psi^0_{k_i}(r_1, r_2) \tag{3.5}$$

We want $\psi^+$ to represent an electron scattering from a hydrogen atom in the ground (1s) state. The bound electron is represented by the ground state radial function $\phi_1$.

$$\phi_1(r) = \frac{2r}{a_0^{3/2}}e^{-r/a_0} \tag{3.6}$$

An incident electron with momentum $\hbar k_i$ is represented by $\sin(k_i r)$ which comes from the zero angular momentum term of the multipole expansion of $e^{ik_i z}$ (see Equation F.17). The initial state $\psi^0_{k_i}$ is an anti-symmetrized product of these two functions.

$$\psi^0_{k_i}(r_1, r_2) = \tfrac{1}{\sqrt{2}}\left(\sin(k_i r_1)\phi_1(r_2) + (-1)^S\phi_1(r_1)\sin(k_i r_2)\right) \tag{3.7}$$

Singlet ($S = 0$) wave functions are symmetric with respect to interchange of the coordinates $r_1$ and $r_2$ while triplet ($S = 1$) wave functions are anti-symmetric. As mentioned in Chapter 2, we perform separate calculations for the two spin symmetries.

## 3.2 Asymptotic Form

We can write the asymptotic form of the Temkin-Poet scattered wave by direct analogy with Equation 2.10. It contains a sum of "two-body" terms corresponding to the discrete channels as well as an additional term for ionization.

$$\psi^+_{\mathrm{TP}}(r_1, r_2) \underset{r_1, r_2 \to \infty}{\longrightarrow} \sum_{n=1}^{\infty} \frac{f_n}{\sqrt{2}}\left(\phi_n(r_1)e^{ik_n r_2} + (-1)^S e^{ik_n r_1}\phi_n(r_2)\right) + \psi_{\mathrm{ion}}(r_1, r_2) \tag{3.8}$$

Since the Temkin-Poet model supports only the zero angular momentum states of hydrogen the discrete channels are restricted to elastic scattering and excitations into other $s$-states of hydrogen. The $s$-state radial functions $\phi_n$ satisfy the $l = 0$ radial equation for hydrogen bound states.

$$\left(-\frac{\hbar^2}{2m}\frac{d^2}{dr^2} - \frac{e^2}{r}\right)\phi_n(r) = \varepsilon_n\phi_n(r) \tag{3.9}$$

The energies $\varepsilon_n$ are the bound state energies of hydrogen, $\varepsilon_n = -\frac{13.6}{n^2}\text{eV}$. Energy conservation determines the momentum $\hbar k_n$ of the scattered electron.

$$\frac{1}{2}\hbar^2 k_n^2 + \varepsilon_n = \frac{1}{2}\hbar^2 k_i^2 + \varepsilon_0 = E \tag{3.10}$$

The ionization term $\psi_{\text{ion}}$ accounts for all of the "three-body" nature of the scattered wave. By analogy with the Rudge asymptotic form of the ionization wave function in Equation 2.11 we can write an asymptotic form in hyperspherical coordinates $\rho$ and $\alpha$ ($r_1 = \rho\sin\alpha, \quad r_2 = \rho\cos\alpha$) for $\psi_{\text{ion}}$, keeping in mind that the scattered wave radial function used here includes a factor of $r_1 r_2$.

$$\psi_{\text{ion}}(r_1, r_2) \underset{\rho\to\infty}{\longrightarrow} -f_i(\alpha)\sqrt{\tfrac{iK^3}{\rho}}e^{i[K\rho+(\zeta/K)\ln(2K\rho)]} \tag{3.11}$$

The ionization scattering amplitude $f_i$ and the phase factor $\zeta$ are both functions of only the hyperangle $\alpha$.

While the discrete channel components are outgoing waves in one of the radial coordinates, the ionization component is an outgoing wave in the hyperradius $\rho$ that cannot be written as a sum of products of one-dimensional functions of $r_1$ and $r_2$. The presence of both of these two very different types of outgoing waves in $\psi_{\text{ion}}$ provides the motivation for a calculational method that is applicable to *any* outgoing wave without regard to any specific asymptotic form.

## 3.3 Exterior Complex Scaling

The method of exterior complex scaling (ECS) uses a mathematical transformation of the scattered wave equation to simplify the outgoing wave boundary conditions. Here we will introduce ECS in the context of the Temkin-Poet model. In Appendix A, it is applied to the simpler problem of one-dimensional potential scattering. Under ECS, the scattered wave equation (Equation 3.5) is solved with the radial coordinates mapped on to a complex contour that is real for small values but, beyond a certain distance, is bent into the upper-half of the complex plane.

The simplest such contour is one where the coordinates are defined to be real out to some finite radius $R_0$ and beyond that are rotated into the upper-half of the complex plane at a scaling angle $\eta$ from the real axis. Let $R_0 \geq 0$ and $0 < \eta < 90^o$ define a complex contour $z(r)$ parametrized by the real coordinate $r$.

$$z(r) \equiv \begin{cases} r & r < R_0 \\ R_0 + (r - R_0)e^{i\eta} & r \geq R_0 \end{cases} \tag{3.12}$$

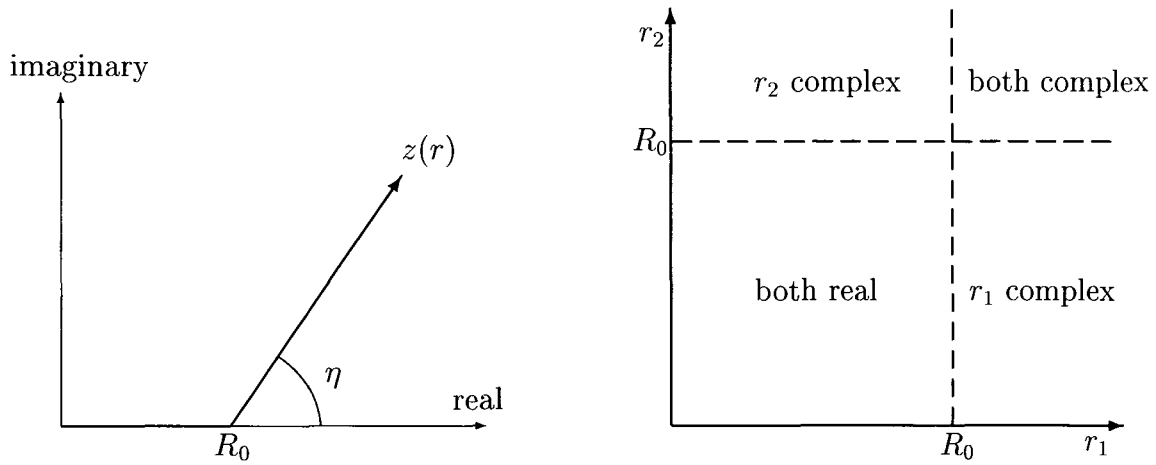


Figure 3.1: On the left is an illustration of the contour $z(r)$ rotated into the upper-half of the complex plane beyond $R_0$. On the right is a depiction of exterior complex scaling for two radial coordinates.

In the Temkin-Poet model this transformation is applied to both $r_1$ and $r_2$ as illustrated in Figure 3.1. Both coordinates are real on an interior box of length $R_0$. Outside that box there are three distinct regions where one or both of the coordinates is complex.

### 3.3.1 Outgoing waves become finite-range functions

We can most easily see the effect of ECS on an outgoing wave by considering an outgoing spherical wave $e^{ikr}$ evaluated on the contour $z(r)$ defined in Equation 3.12.

$$e^{ikr} \rightarrow e^{ikz(r)} = e^{kR_0 \sin\eta} e^{ikR_0(1-\cos\eta)} e^{ikr\cos\eta} e^{-kr\sin\eta} \qquad (\text{for } r > R_0) \qquad (3.13)$$

The infinite-range outgoing wave is transformed into a function that decays exponentially beyond $R_0$, provided that $\eta > 0$. Exterior complex scaling has the same effect on any outgoing wave (other one-dimensional examples are shown in Appendices A and C), including those with logarithmic phase terms, although the exact analytic expression is more complicated. As a result, every outgoing wave (including the two-dimensional scattered wave $\psi^+_{\mathrm{TP}}$) is transformed into a function that goes to zero at large distances.

In Figure 3.2 we see the effect of ECS on the eigenvalue spectrum of the Hamiltonian for a hydrogen atom. The characteristics of eigenvalue spectra under ECS were originally described by Barry Simon [36]. Bound state energies of hydrogen are unaffected by ECS because the bound state eigenfunctions remain bound under ECS. The positive eigenvalues, which correspond to the continuum of ionized states of hydrogen, have been rotated into the lower-half of the complex plane. This is directly linked to the transformation of the infinite-range continuum states to finite-range functions under ECS. The eigenvalue spectrum for the two-electron Hamiltonian is more complicated but, has these same general features.

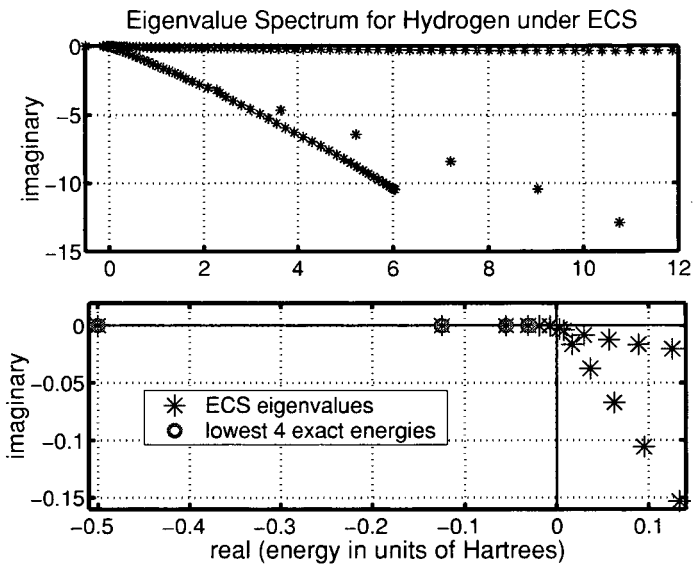


bound state energies

| $n$ | calculated | exact |
|---|---|---|
| 1 | -0.500159 | -0.500000 |
| 2 | -0.124931 | -0.125000 |
| 3 | -0.055580 | -0.055556 |
| 4 | -0.031235 | -0.031250 |
| 5 | -0.019046 | -0.020000 |
| 6 | -0.007272 | -0.013889 |

grid

| spacing | range |
|---|---|
| $0.01a_0$ | $0$—$0.1a_0$ |
| $0.05a_0$ | $0.1$—$2.0a_0$ |
| $0.2a_0$ | $2.0$—$55.0a_0$ |
| $0.5a_0$ | $55.0$—$80.0a_0$ |

Figure 3.2: The eigenvalue spectrum of an exterior complex scaled radial Hamiltonian for hydrogen. All of the eigenvalues with positive real parts lie below the real axis. Numerical values for the bound state eigenvalues are compared with the exact hydrogen bound state energies. The grid spacings used in this example are also given. The Coulomb potential was truncated at $50a_0$. Beyond $50a_0$ the coordinates are complex with a scaling angle of $30^o$ and extend another $30a_0$.

### 3.3.2 Application to long-range potentials

The presence of Coulomb, or any other long-range potentials, in the Hamiltonian precludes straight-forward application of ECS to the scattered wave equation. Under ECS, outgoing waves become finite-range functions and bound states remain bound. However, *incoming* waves become exponentially *increasing* functions as can be easily seen by changing the sign of $k$ in Equation 3.13. This is a problem because the definition of the initial state $\psi^0_{k_i}$ contains $\sin(k_i r)$ which can be written as the sum of an incoming and an outgoing wave. Thus, $\psi^0_{k_i}$, which appears in the driving term of the scattered wave equation, is an exponentially increasing function under ECS.

Since $\psi^0_{k_i}$ is acted on by the operator $(\hat{H} - E)$ in the scattered wave equation we need to consider the entire right-hand side of Equation 3.5.

$$\left(\hat{H} - E\right)\psi^0_{k_i} = \frac{1}{\sqrt{2}}\left(\frac{\mathrm{e}^2}{r_>} - \frac{\mathrm{e}^2}{r_1}\right)\sin(k_i r_1)\phi_1(r_2) + \frac{(-1)^s}{\sqrt{2}}\left(\frac{\mathrm{e}^2}{r_>} - \frac{\mathrm{e}^2}{r_2}\right)\phi_1(r_1)\sin(k_i r_2) \tag{3.14}$$

The unscaled right-hand side decays like $\frac{1}{r}$ due to the Coulomb potentials left over after $(\hat{H} - E)$ acts on $\psi^0_{k_i}$. The damping from the Coulomb potentials is not enough to counteract the exponential increase in $\psi^0_{k_i}$ after the ECS transformation. Thus, under ECS the driving term in Equation 3.5 diverges for large $r_1$ or $r_2$.

The prescription for getting around this limitation is demonstrated in Appendices A and B. Long-range potentials are truncated at $R_0$, effectively replacing them by

artificially short-range potentials and making the driving term in Equation 3.5 vanish where the coordinates are complex. Obviously, in order for the calculated results to be meaningful $R_0$ must be large enough that truncating the potentials has little effect on the collision dynamics. The purely outgoing nature of $\psi^+_{\mathrm{TP}}$ minimizes the error in the calculated wave function due to truncating the potentials.

### 3.3.3 Wave function unaffected where coordinates are real

In the region where the coordinates are real the scattered wave equation is unaffected by the ECS transformation. Assuming the numerical methods used are accurate, we expect the scaled wave function to be the same as the unscaled (physical) wave function in the region where both coordinates are real.

$$\psi^+_{\mathrm{TP}}(z(r_1), z(r_2)) \simeq \psi^+_{\mathrm{TP}}(r_1, r_2) \qquad (\text{for } r_1, r_2 < R_0) \tag{3.15}$$

However, we cannot claim true equality in Equation 3.15 because the Coulomb potentials are truncated at $r = R_0$. Since $\psi^+_{\mathrm{TP}}$ is an outgoing wave, we can expect that truncating the potentials at $R_0$ has little effect on $\psi^+_{\mathrm{TP}}$ for $r < R_0$. Truncating the potential does affect the higher-energy hydrogen bound states so $R_0$ needs to be large enough that all bound states that contribute significantly to $\psi^+_{\mathrm{TP}}$ are essentially confined to the region where the coordinates are real. For now, we will assume that the scaled wave function is physically meaningful on the real coordinates, provided that $R_0$ is sufficiently large, and that we may extract various physical quantities by analyzing the numerically generated wave function on the region inside $R_0$.

## 3.4 Finite Difference Implementation

Exterior complex scaling makes the scattered wave equation solvable. We now need a numerical implementation for accurately calculating the scaled wave function. The simple ECS contour described in Equation 3.12 has a discontinuous derivative at $R_0$. Consider what this means for an outgoing spherical wave. For $r < R_0$ the outgoing wave is $e^{ikr}$ and the second derivative as $r \to R_0$ from smaller $r$ is $-k^2 e^{ikR_0}$. However, for $r > R_0$ we must use the functional form given in Equation 3.13. The second derivative as $r \to R_0$ from larger $r$ is $-k^2 e^{i2\eta} e^{ikR_0}$. Thus, the second derivative is discontinuous at $r = R_0$ by a factor of $e^{i2\eta}$. Consequently, standard basis set methods that expand the wave function in some set of analytic functions cannot be used with this contour. As described in Appendix B, analytic basis set methods can be made to work if a "smooth" contour is used instead. However, using a smooth contour rather than the "sharp" contour from Equation 3.12 adds significantly to the cost of solving the scattered wave equation.

Two types of methods that can correctly represent a function under ECS with the sharp contour are finite difference and finite elements. Finite element methods divide space into finite regions and expand the wave function in each region with a set of basis functions that are defined to be zero outside their particular region. If $R_0$ lies on the boundary between two regions then finite element methods can

be designed to produce wave functions with exactly the right discontinuity in their first derivatives. Finite elements have been successfully applied to the Temkin-Poet model [20]. However, producing the matrices for this method is expensive, making it less suitable for the full electron-hydrogen problem.

Finite difference methods map the wave functions directly on to a numerical grid and can produce wave functions with the correctly discontinuous first derivatives. The matrices involved are much simpler to construct than those for finite elements. For this and other reasons, finite difference is more easily extended to the full electron-hydrogen problem and will be the method of choice throughout this dissertation.

### 3.4.1 ECS on a grid

Under ECS, the scattered wave $\psi^+_{\mathrm{TP}}(z(r_1), z(r_2))$ is a continuous function but has discontinuous first derivatives along the lines $r_1$ or $r_2$ equal to $R_0$. There is no problem representing the wave function on a two-dimensional grid in $r_1$ and $r_2$, but in order to correctly approximate its derivatives on each grid point we will require that $R_0$ be one of the grid points. The scattered wave will be calculated directly on to the ECS contour by solving Equation 3.5 on the two-dimensional, complex-scaled grid.

Functions whose analytic forms are known, such as the right-hand side of Equation 3.5 and the potentials in the Hamiltonian, are mapped on to the ECS contour by simply evaluating them on the contour $z(r)$ for both $r_1$ and $r_2$. The non-analytic two-electron potential $\frac{e^2}{r_>}$ is scaled in this way by noting that it is piece-wise analytic and scaling the $r_1 < r_2$ and $r_1 > r_2$ regions separately. The potential is unchanged on the real part of the grid and, as will be demonstrated later in this chapter, the potentials beyond $R_0$ have very little effect on the wave function in the interior region.

### 3.4.2 Finite difference approximations to derivatives

We replace the kinetic energy term in Equation 3.2 by finite difference formulas given in Appendix C. The second derivative with respect to $r_1$ or $r_2$ at some grid point is represented by a formula involving the value of the wave function at that point and at three points on either side. For a uniform grid, the seven-point finite difference formula is accurate to sixth order in the grid spacing. The sum of the two second derivatives forms the cross-shaped, 13-point "stencil" shown in Figure 3.3.

At one or two grid points away from $r_1 = 0$ or $r_2 = 0$ the seven-point formulas cannot be used because they would require terms for grid points at negative $r$. Less accurate five-point formulas are used at these points instead. A very small grid spacing near $r = 0$ is required because the Coulomb potentials are singular at zero, so five-point finite difference near $r = 0$ still provides good accuracy. There is no such issue at the large $r$ boundary, $r = R_{\mathrm{max}}$. If $(R_{\mathrm{max}} - R_0)$ is large enough that $\psi^+_{\mathrm{TP}}$ is effectively zero at $R_{\mathrm{max}}$ then we can define the wave function to be zero at $R_{\mathrm{max}}$ *and beyond* and thus implicitly include the value of the wave function at any point beyond the extent of the grid.

Application of exterior complex scaling to finite difference is very straight forward. To understand how ECS is applied to the kinetic energy term, let us consider what

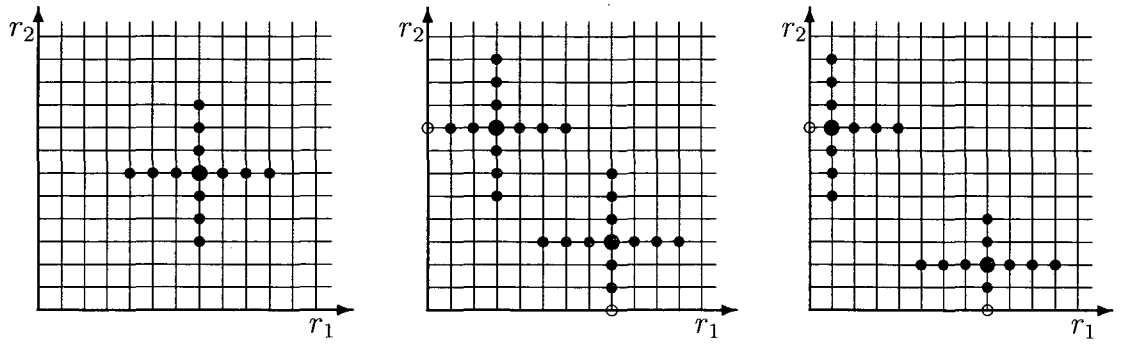


Figure 3.3: The sixth order finite difference representation of the two-dimensional Laplacian uses a 13-point stencil based on the 7-point formulas for the second derivative in one dimension as illustrated on the left. Along the grid boundaries the function's value is fixed to be zero and the edge points are included in the finite difference formulas implicitly. If the center of the stencil is two grid points from an edge then the 5-point formula replaces the 7-point formula in one dimension. If the center is one grid point from an edge then a special, asymmetric 5-point formula is used.

scaling the derivatives means.

$$\frac{d^2}{dr^2} \rightarrow \frac{d^2}{dz(r)^2} = \left(\frac{dz(r)}{dr}\right)^{-2} \frac{d^2}{dr^2} = e^{-i2\eta} \frac{d^2}{dr^2} \tag{3.16}$$

If all points included in the finite difference formula lie on the complex part of the grid then we simply multiply the formula by $e^{-i2\eta}$. By examining the formulas in Appendix C we see that this is equivalent to multiplying the grid spacings by $e^{i\eta}$. This view is consistent with the fundamental concept expressed in Equation 3.16 that after the ECS transformation the derivatives with respect to $r$ become derivatives with respect to the complex contour $z(r)$.

In general, we apply ECS to finite difference by multiplying all grid spacings for $r > R_0$ by $e^{i\eta}$. The finite difference formulas for $r < R_0$ and $r > R_0$ differ by a factor of $e^{i2\eta}$, exactly the discontinuity factor that we found when considering the outgoing spherical wave. This is why finite difference is well-suited for a sharp ECS contour provided that $R_0$ is one of the grid points. Finite difference formulas for grid points at or near $R_0$ will straddle $R_0$ so that some of the grid "spacings" in these formulas are real and some are complex. Therefore, we cannot assume a uniformly spaced grid when using ECS. Specialized finite difference formulas designed for the interface between two regions of different grid spacings are given in Appendix C.

### 3.4.3 System of linear equations

We will solve for $\psi^+_{\mathrm{TP}}(r_1, r_2)$ directly on to a two-dimensional Cartesian grid of discretized radial coordinates that is defined in terms of a one-dimensional grid of $n_g$ grid points spanning the space between zero and some radius $R_{\mathrm{max}} > R_0$. $R_{\mathrm{max}}$ must be large enough that the exterior complex scaled scattered wave can be assumed to be zero for $r_1, r_2 \geq R_{\mathrm{max}}$. Referring to Equation 3.13, we see that an outgoing wave with

momentum $\hbar k$ decays like $e^{-k \sin\eta(r-R_0)}$ for $r > R_0$. That means we should choose $\eta$ and $R_{\max}$ so that $e^{-k \sin\eta(R_{\max}-R_0)}$ is effectively zero.

The total number of grid points, and thus the number of values calculated for $\psi^+_{\rm TP}$, is $N = n_g^2$. We calculate the scattered wave by casting Equation 3.5 as a matrix equation of the form $\mathbf{Ax} = \mathbf{b}$ where $\mathbf{x}$ is a vector of the $N$ unknown values of $\psi^+_{\rm TP}$ on the grid, $\mathbf{b}$ is a vector of $N$ values obtained by evaluating Equation 3.14 on the grid, and $\mathbf{A}$ is the $N \times N$ matrix representation of the operator $(E - \hat{H})$. The vectors $\mathbf{x}$ and $\mathbf{b}$ are ordered so that the values of $\psi^+_{\rm TP}(r_1, r_2)$ for the same $r_2$ are stored contiguously. To form the matrix we add together the matrix representations of each individual term from the Hamiltonian definition in Equation 3.2. One consequence of using exterior complex scaling, or using any grid with multiple grid spacings, is that the Hamiltonian matrix will not be Hermitian or even complex-symmetric.

Potentials are simply evaluated on the grid and those $N$ values, along with the constant term $E$, are added to the diagonal. The finite difference formulas provide all of the non-zero off-diagonal matrix elements. As shown in Figure 3.3, the Laplacian at each grid point is determined by function values from no more than 13 grid points. This means that each row of the matrix will have at most 13 nonzero matrix elements, so the matrix is very sparse. The sparsity structure of the finite difference matrix representation of $(E - \hat{H})$ is shown in Figure D.1.

### 3.4.4 Dimension of the problem

The size of the calculation needed to obtain $\psi^+_{\rm TP}$ is governed by the total number of grid points. Deciding how to distribute a fixed number of grid points requires striking a balance between the higher accuracy of closely spaced grid points and the greater information content of a grid covering a larger region. An advantage of using the sixth order finite difference formulas is that we get a large payoff in accuracy from small increases in grid density. In general, we can represent $\psi^+_{\rm TP}$ accurately if there are several grid points per oscillation. Most of the calculations presented here used five grid points per atomic unit, sufficient for incident energies less than 50 eV.

However, the Coulomb potentials are singular at $r = 0$ so a spacing of $0.2a_0$ is inadequate for representing the potentials at small $r$. We can evaluate how well a particular grid represents the Coulomb potential by diagonalizing the finite difference approximation to the one-dimensional radial hydrogenic Hamiltonian of Equation 3.9 and comparing the negative real eigenvalues with the known bound state energies of hydrogen. A spectrum from a complex scaled Hamiltonian is shown in Figure 3.2. In this example a spacing of $0.01a_0$ near $r = 0$ and $0.05a_0$ out to $r = 2a_0$ gives the ground state energy and excited state energies up to $n = 4$ correct to better than 0.05% and we can assume that the corresponding eigenstates are good approximations to the true hydrogen states. Note that the calculated ground state energy is below the exact value. With finite difference there is no variational principle that forces the calculated ground state energy to be larger than the exact value.

Beyond $r = R_0$ the wave function is particularly insensitive to grid spacing and we can use very large (but still less than $1a_0$) grid spacings near $r = R_{\max}$. Specialized

finite difference formulas valid for "stencils" that span regions of two different grid spacings are listed in Appendix C. These formulas allow us to use grid spacings of $0.2a_0$ over most of the grid, a tight grid spacing for small $r$, and a very large grid spacing for large $r$ with only a moderate cost in accuracy. These specialized formulas also make application of ECS possible.

A typical grid that spans $100a_0$ in real coordinates and an additional $25a_0$ in complex coordinates requires 458 grid points in one dimension. The total number of grid points in two dimensions, and the dimension of the matrix equation, is then 209,764. The largest calculation presented here was for a grid that is real out to $450a_0$ with 1,339 grid points giving a system of 1,792,921 equations.

### 3.4.5 Solving linear equations

We have cast Equation 3.5 into a linear matrix equation that must be solved in order to generate the scattered wave. The size of the matrix for the Temkin-Poet model is large enough to warrant developing an efficient algorithm for solving the system of linear equations, especially since we ultimately want to solve the much larger six-dimensional problem of electron-hydrogen scattering.

Most of the matrix elements are zero and there is a huge savings in computer memory if the matrix representation of $(E-\hat{H})$ is stored in the sparse format described in Appendix D. In a sparse matrix storage scheme only the nonzero matrix elements are stored. Sparse matrix algorithms are more difficult to write and almost never generate impressive MFLOPS ratings. However, if the matrix is truly sparse then the reduction in the number of required arithmetical operations more than makes up for this and the sparse matrix algorithms typically take significantly less time than their dense matrix counterparts. Setting up the finite difference matrix equations is trivial so most of the computational time is used for solving the large matrix equations.

The canonical "direct method" for solving a system of linear equations is Gaussian elimination. Solving systems of equations of the size needed here requires highly optimized software running on modern, high-performance computers. At present, the only numerical software capable of directly solving matrix equations this large is a package of $LU$-factorization routines, called SuperLU [19], that is designed for sparse matrices. Time and memory costs of using SuperLU to solve linear equations with two-dimensional finite difference matrices are discussed in Appendix D.

The time and memory requirements for $LU$-factorization of the low-order finite difference matrix are much less than those for the high-order matrix. An iterative algorithm which arrives at the solution to the high-order equations by repeatedly using SuperLU to directly solve the low-order equations is described in Appendix E. This iterative algorithm gives substantial savings in memory and time compared with directly solving the high-order finite difference matrix equations.

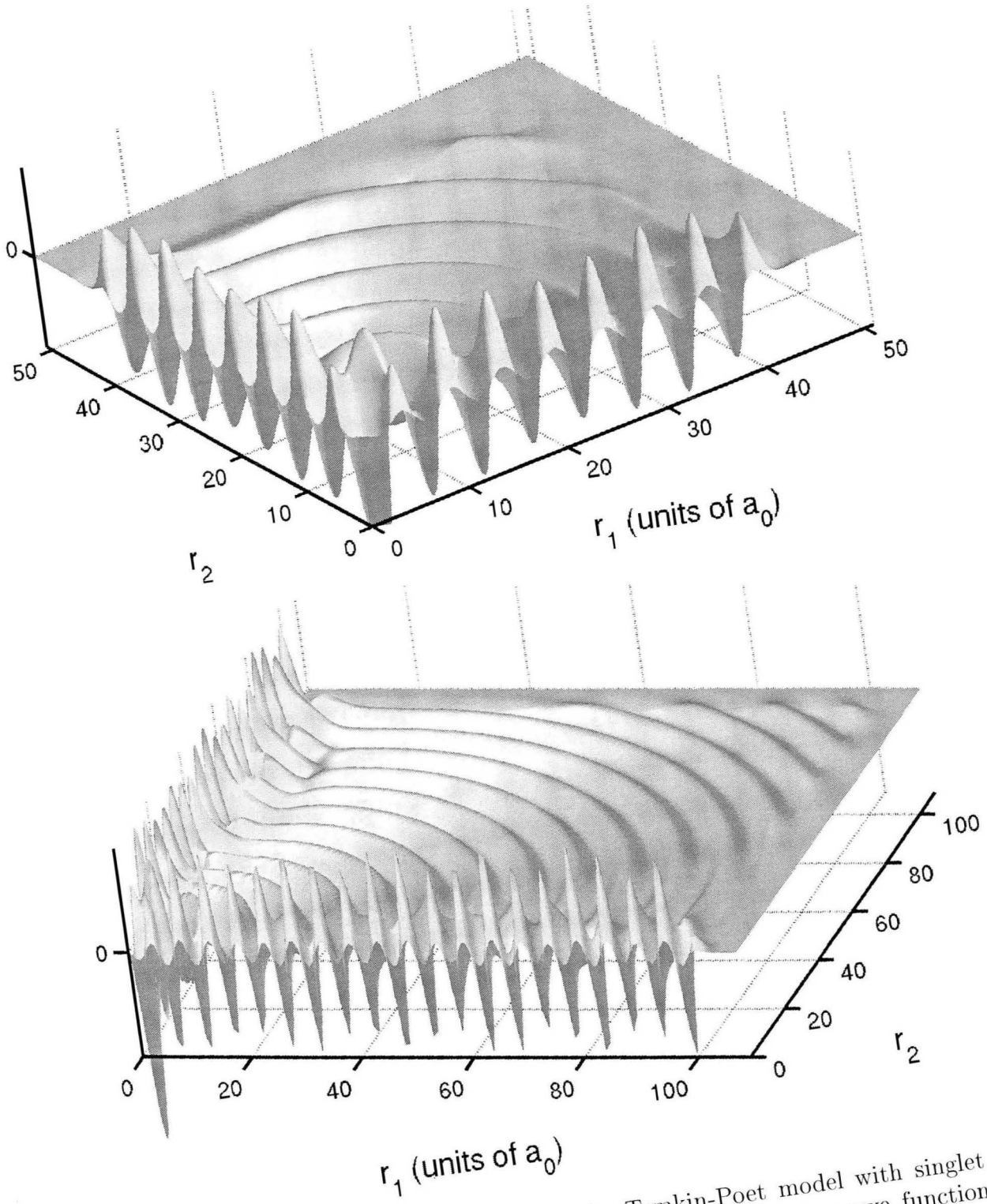


Figure 3.4: Sample scattered waves for the Temkin-Poet model with singlet spin symmetry at an incident energy of 20.4 eV. Real parts of the wave functions are shown. Upper picture shows a wave function calculated on a grid that was real to $40a_0$. Lower picture shows a wave function calculated on a grid that was real to $100a_0$.

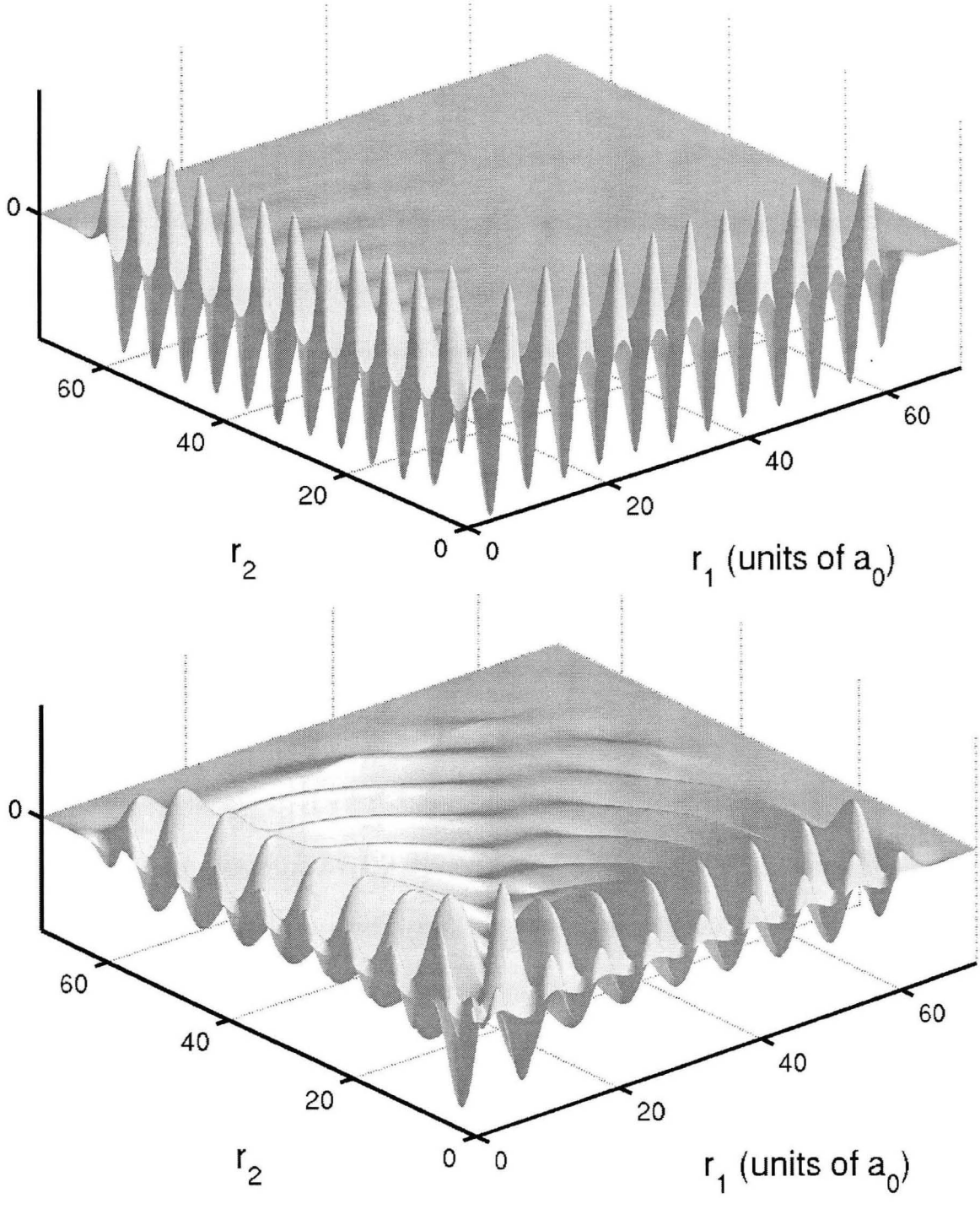


Figure 3.5: Sample scattered wave for the Temkin-Poet model with triplet spin symmetry at an incident energy of 20.4 eV. Real parts of the wave functions are shown. Upper picture shows wave function calculated on a grid that was real to $60a_0$. Lower picture shows the same wave function after projecting out the elastic channel.

## 3.5 Properties of the Calculated Wave Functions

Figures 3.4 on page 23 and 3.5 on page 24 show examples of the real part of the Temkin-Poet scattered wave for an incident energy 6.8 eV above the ionization threshold. The singlet wave function is symmetric while the triplet wave function is anti-symmetric with a characteristic "trough" down the ray $r_1 = r_2$. Different asymptotic components of the scattered wave, as identified in Equation 3.8, are visible. Discrete channel components are products of outgoing waves, which span the length of the grid, and bound states, which extend over small distances. These components appear as oscillations localized along the $r_1$ and $r_2$ axes. The ionization component has both electrons in the continuum and appears as circularly outgoing waves spanning the space between the two axes. It is this part of the wave function that is difficult to represent in traditional, "two-body" formalisms. The exponentially damped "fringe" where the coordinates are complex is visible in each picture.

Figure 3.4 shows the singlet wave function calculated on two different sized grids. Two distinct components of the singlet wave function are visible on the smaller grid. Peaks along the edges are due to elastic scattering. The wavelength of those oscillations is equal to the wavelength of the incident wave, and the shape of the peaks is proportional to the ground state radial function for hydrogen. Circular waves corresponding to ionization span the space between the two coordinate axes. These have a longer wavelength because ionization requires a loss of kinetic energy equal to the ionization potential of hydrogen (13.6 eV). More components of the wave function are visible on the larger grid. At larger distances, excitation channel components emerge. These look like products of excited states of hydrogen, which extend further from the axes, and plane waves with longer wavelengths. The presence of different wavelengths causes a "beat" pattern in the wave function along the edges of the grid.

The upper picture in Figure 3.5 shows the triplet wave function calculated on a grid that is real out to $60a_0$. Elastic scattering dominates this wave function so much that almost nothing else is visible. The lower picture in Figure 3.5 shows the same wave function but with the elastic scattering component projected out using the projection operators defined in Equations 4.10 and 4.11. With the elastic channel removed the wave function on the edges of the grid is dominated by excitation of the $n = 2$ state. By comparing the upper and lower pictures we can see the difference in the wavelengths of the elastic ($n = 1$) and the $n = 2$ components. Also, the shape of the peaks in the lower picture is proportional to the $n = 2$ radial function for hydrogen. Because the triplet wave function is anti-symmetric, the ionization waves have a "trough" along the ray $r_1 = r_2$.

In the examples shown in Figures 3.4 and 3.5 the ionization component forms well-defined outgoing waves in the hyperradius $\rho$ within about $20a_0$. As the scattered wave propagates away from the origin the discrete channel components remain confined to a certain distance from each edge so they occupy a continuously decreasing range of the hyperangle $\alpha$. The ionization wave, however, continues to span the full range of $\alpha$. Thus, as the scattered wave propagates outward the discrete channel components spatially separate from the ionization wave so that an increasingly larger fraction of the ionization wave is "uncovered" by the discrete channel components.

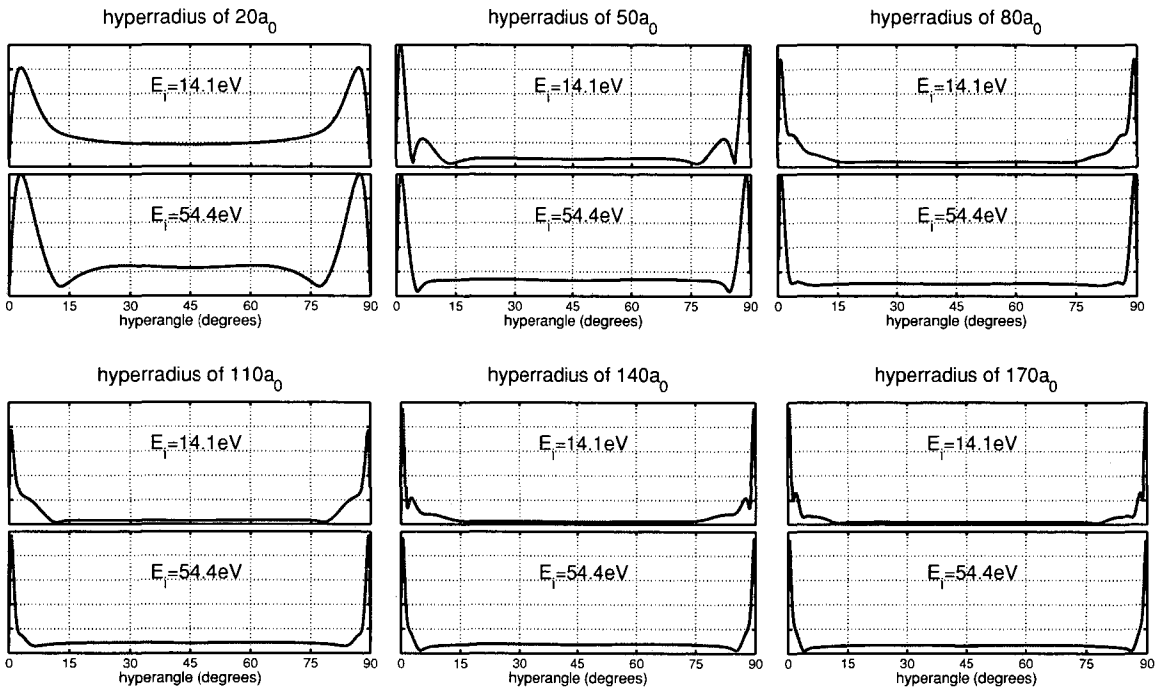


Figure 3.6: The absolute value of the scattered wave radial functions along arcs of a constant hyperradius. At each hyperradius two wave functions corresponding to incident energies $E_i$ = 14.1eV and 54.4eV are shown. For each energy the vertical scale is the same at every hyperradius.

This uncovering of the ionization wave is visible in Figure 3.6 which shows cross-sections of the scattered wave for two incident energies along six different arcs of constant hyperradius. Looking at either wave function, we can see initially that for a hyperradius of $20a_0$ there are two well-defined peaks corresponding to elastic scattering with a smooth curve between them. As the hyperradius increases the elastic scattering peak becomes confined to a smaller region of the hyperangle. Also, peaks corresponding to the excitation components begin to emerge as they, too, become confined to smaller regions of the hyperangle. The heights of the discrete channel peaks remain essentially constant, aside from small fluctuations due to the beat pattern mentioned previously, while the height of the ionization curve decreases monotonically with increasing hyperradius.

Although, formally, there are an infinite number of excitation channels present, their importance relative to ionization decreases for increasing energy quantum number. For a given incident energy there are a finite number of discrete channel components that need to be removed from the scattered wave to isolate the majority of the ionization wave to acceptable accuracy. The number of these components that cannot be ignored determines how far from the origin we must look in order to see the uncovered ionization wave. As can be seen in Figure 3.6, for incident energies near the ionization threshold the uncovering of the ionization wave happens much more slowly. This is because the ionization wave is much smaller relative to the discrete

channel components at scattering energies slightly above the ionization threshold.

## 3.6 Accuracy of the Calculated Wave Functions

Accuracy of the calculated wave functions can be affected by numerical error in the calculations as well as systematic error due to the formalism. Numerical error can come from round-off errors in solving the large systems of linear equations but is mainly due to error in the finite difference representation. The primary grid spacing is typically $0.2a_0$, so by using sixth order finite difference formulas the error should be no more than $10^{-4}$. Thus, we expect the numerical error in the wave functions to be better than a tenth of a percent.

In terms of systematic error, the main concern is the effect from truncating the Coulomb potentials. We are trying to use artificially short-range potentials to calculate information for systems with long-range potentials. In order for these calculations to be meaningful, it is necessary that on the interior region the wave function be unaffected by truncating the potentials. We can check this by comparing two wave functions calculated on different grids, with the size of the grid determining where the potentials are truncated.

Figure 3.7 shows several comparisons performed along arcs of constant hyperradius $\rho$, similar to Figure 3.6. For the most part, the relative differences in the wave functions are no more than 0.01% which is less than the estimated numerical error for a primary grid spacing of $0.35a_0$. The differences are somewhat greater for comparisons done at larger $\rho$ but are still acceptable, especially considering that the grid spacing used for these comparisons was wider than what would normally be used.

Plots in Figure 3.7 compare results from potentials truncated at different distances. Ideally, we would compare to results for truly infinite range Coulomb potentials. Of course, this is impossible. Instead, we can see if the calculated wave functions are approaching the asymptotic form for ionization given in Equation 3.11. This two-dimensional form was presented by analogy with the Rudge asymptotic form in

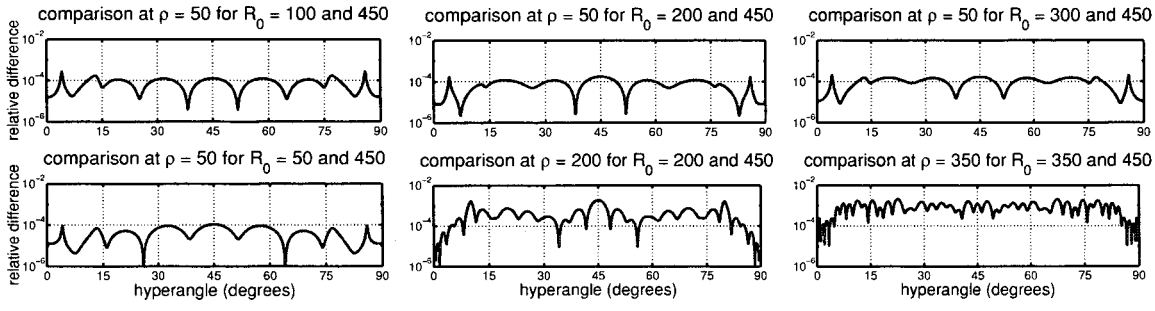


Figure 3.7: Comparison of 14.4eV incident energy, singlet, Temkin-Poet wave functions along a constant hyperradius $\rho$ for calculations using grids that were real out to different values of $R_0$. The primary grid spacing used in these calculations was $0.35a_0$. All distances are in units of $a_0$.

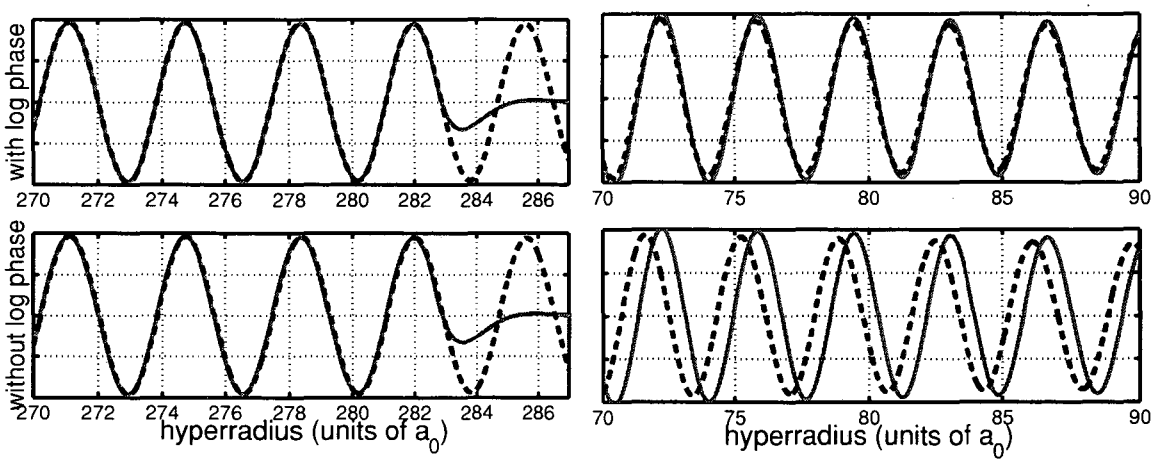


Figure 3.8: Demonstration of the logarithmic phase term in the singlet Temkin-Poet scattered wave for 54.4eV incident energy. All four figures show the real part of $\psi^+_{\rm TP}(r_1, r_2)$ (solid line) along the ray $r_1 = r_2$. The wave function is complex scaled beyond $283a_0$. The upper figures show a function (dashed line) with a logarithmic phase fit to $\psi^+_{\rm TP}$. The fit was done for large values of the hyperradius $\rho$ and the two curves are distinguishable only for $\rho > 283a_0$ where $\psi^+_{\rm TP}$ is complex scaled. The upper right compares the same functions for a region of smaller $\rho$ where there are slight differences in the amplitudes between the two. The lower figures make the same comparison, but fit to a functional form without a logarithmic phase. The fit is again done at large $\rho$, but this time there is a noticeable difference in phase at smaller $\rho$.

Equation 2.11 which is valid only when the two electrons are well separated from each other. It is unclear exactly what this means in the Temkin-Poet model so we certainly cannot use the form in Equation 3.11 to match to the entire wave function. However, if we look only along the ray $r_1 = r_2$ then we can expect $\psi^+_{\rm TP}$ to have the essential features of Equation 3.11: a logarithmic term in the phase and a $\frac{1}{\sqrt{\rho}}$ decay in the amplitude.

In Figure 3.8 the real part of the wave function along the ray $r_1 = r_2$ is compared to a function of the form $\frac{A}{\sqrt{\rho}} \sin(\kappa\rho + B \ln 2\kappa\rho + C)$ where $\frac{\hbar^2}{2m}\kappa^2 = E$, which in this example is 54.4 eV. The wave function was calculated on a grid that was real on a box of length $200a_0$ so the coordinates are real out to $\rho = 282.8a_0$ along the ray $r_1 = r_2$. Coefficients $A$, $B$, and $C$ were chosen to fit $\psi^+_{\rm TP}$ locally over a range of $\rho$ between $270a_0$ and $280a_0$. This functional form fits $\psi^+_{\rm TP}$ in this region so well that it is visible only beyond $283a_0$ where $\psi^+_{\rm TP}$ is exponentially damped by the complex coordinates. Even at smaller $\rho$ it fits $\psi^+_{\rm TP}$ very well, with only a slight difference in amplitude but still very good agreement in phase.

For comparison, the same type of fit was done without the logarithmic phase term *i.e.*, forcing the coefficient $B$ to be zero. Coefficients $A$ and $C$ were chosen to match $\psi^+_{\rm TP}$ over the same range of $\rho$ between $270a_0$ and $280a_0$. Even without the logarithmic phase we can match $\psi^+_{\rm TP}$ well over a small region, but there is a significant difference in phase when we examine a different range of $\rho$. Logarithmic phase terms are char-

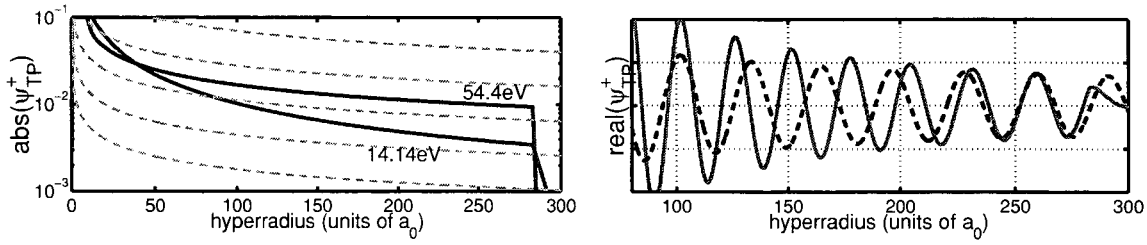


Figure 3.9: The figure on the left shows the absolute value of $\psi^+_{\rm TP}(r_1, r_2)$ along the ray $r_1 = r_2$ for incident energies of 54.4eV and 14.14eV. Several dashed lines proportional to $\frac{1}{\sqrt{\rho}}$ are provided for reference. On the right is an attempt to fit $\psi^+_{\rm TP}$ for 14.14eV to the same functional form as in Figure 3.8, with a logarithmic phase term.

acteristic of Coulomb potentials and the fact that a logarithmic phase is present in our calculated wave functions suggests that truncating the Coulomb potentials has not caused fundamental damage.

The other feature we expect to see in the wave function is a $\frac{1}{\sqrt{\rho}}$ decay in the amplitude. It is clear from Figure 3.8 that this is indeed the case, at least for 54.4 eV incident energy. The $\frac{1}{\sqrt{\rho}}$ decay is a consequence of having both electrons in the continuum. Discrete channel components have just one electron in the continuum and do not decay as the radial coordinate for the continuum electron increases. Thus, the $\frac{1}{\sqrt{\rho}}$ dependence requires the absence of discrete channel components. From Figure 3.6 we know that for very low incident energies the discrete channels contribute significantly to $\psi^+_{\rm TP}$ over a much larger region.

The absolute value of $\psi^+_{\rm TP}$ for incident energies of 54.4 eV and 14.14 eV is plotted on a logarithmic scale in Figure 3.9. We can see that along the ray $r_1 = r_2$ the 54.4 eV wave function decays like $\frac{1}{\sqrt{\rho}}$ beyond about $20a_0$. On the other hand, the 14.14 eV wave function does not exhibit this behavior even at $280a_0$. An attempt to fit the 14.14 eV wave function to the same functional form as in Figure 3.8 confirms that this wave function still has not reached its asymptotic form.

So, exterior complex scaling provides a means for calculating the scattering wave function to arbitrary accuracy, but only on a finite region. We can extract physical quantities from the calculated wave functions if we are able to limit our analysis to the region in which both coordinates are real. To get meaningful results for ionization we need to make the complex scaling point large enough so that a significant portion of the ionization wave has been "uncovered" before the coordinates become complex. Incident energies very near the ionization threshold will require huge calculations so there is an effective lower limit in energy for which this method works. In the next chapter we will investigate the validity of extracting scattering information from calculated wave functions that are known on only a finite region of space.

# Chapter 4

# Calculating Cross Sections for Electron-Impact Ionization

Having calculated wave functions that describe ionization, we need a procedure for extracting from them differential cross sections for ionization. The total scattering cross section is the sum of discrete cross sections for elastic scattering, for each excitation, and for ionization. In the elastic and excitation channels the energy of the outgoing electron is quantized. However, when ionization occurs energy is shared continuously between two outgoing electrons. Single differential cross sections describe this energy sharing. Although differential cross sections for ionization are intrinsically tied to the asymptotic form for three-body breakup, they can be extracted from a wave function known only over a finite region by directly calculating the scattered flux and then using an extrapolation procedure. This method has produced accurate single differential cross sections in the Temkin-Poet model [3].

## 4.1 Total Cross Section

Scattering cross sections are defined in terms of the probability current density for the scattered wave. For consistency with the full electron-hydrogen problem we will treat the Temkin-Poet wave $\psi^+_{\rm TP}(r_1, r_2)$ as the radial function for a six-dimensional scattered wave that happens to have no angular dependence. The six-dimensional scattered wave $\Psi^+_{\rm sc}$ and the three-dimensional ground state function $\Phi_{\rm 1s}$ are related, in the Temkin-Poet model, to their radial function counterparts (defined in Equations 3.4 and 3.6) by multiplication by appropriate factor(s) of $\frac{1}{r}{\rm Y}_{0,0}(\hat{r})$.

$$\Phi_{\rm 1s}(\vec{r}) = \tfrac{1}{r}\phi_1(r){\rm Y}_{0,0}(\hat{r}) \qquad \Psi^+_{\rm sc}(\vec{r}_1, \vec{r}_2) = \tfrac{1}{r_1 r_2}\psi^+_{\rm TP}(r_1, r_2){\rm Y}_{0,0}(\hat{r}_1){\rm Y}_{0,0}(\hat{r}_2) \tag{4.1}$$

Scattering processes are quantified by scattering cross sections defined as the scattered flux divided by the incident flux density. The flux density of some wave function $\Psi$ through a surface $\mathsf{S}$ is defined as the probability current density $\mathsf{j}_\mathsf{S}$ along the surface normal $\hat{n}_\mathsf{S}$.

$$\mathsf{j}_\mathsf{S} \equiv {\rm Im}\left\{\Psi^\star \vec{\nabla}\Psi\right\} \cdot \hat{n}_\mathsf{S} \tag{4.2}$$

The gradient in Equation 4.2 is the one appropriate for the coordinate space in which $\Psi$ is defined.

For a plane wave $e^{ik_i z}$ the flux density is $k_i$ in the $\hat{z}$ direction. We need to relate $\sin k_i r$ in the Temkin-Poet initial state (Equation 3.7) to the expansion of a plane wave in terms of Ricatti-Bessel functions $\hat{j}_l(k_i r)$.

$$e^{ik_i z} = \sum_{l=0}^{\infty} i^l \sqrt{4\pi(2l+1)} \frac{\hat{j}_l(k_i r)}{k_i r} \mathrm{Y}_{l0}(\hat{r}) \tag{4.3}$$

Since $\hat{j}_0(k_i r) = \sin(k_i r)$ the initial state defined in Equation 3.7, after multiplication by the $\frac{1}{r}\mathrm{Y}_{0,0}(\hat{r})$ factors, is equal to the $l = 0$ term of the expansion in Equation 4.3 anti-symmetrized with the hydrogen ground state and multiplied by $\frac{k_i}{\sqrt{4\pi}}$. Thus, the incident flux density in the Temkin-Poet model, with the initial state defined in Equation 3.7, should be $\frac{k_i^3}{4\pi}$.

Measuring the scattered flux requires a closed surface $\mathsf{S}$ in six-dimensional space that surrounds the interaction region. The discrete channel flux is outgoing in $r_1$ and $r_2$ while the ionization flux is outgoing in the hyperspherical radius $\rho$. Since discrete channel flux remains localized near the $r_1$ and $r_2$ axes in a two-dimensional radial coordinate system (see Figure 3.6) we can say that, in the limit $\rho \to \infty$, all scattered flux is outgoing in $\rho$. Thus, the appropriate surface $\mathsf{S}$ is a hypersphere of radius $\rho = \rho_0$ in the limit $\rho_0 \to \infty$.

We define the probability current density $\mathsf{j}_{\rho_0}$ through a hypersphere of radius $\rho_0$ by Equation 4.2 with surface normal $\hat{n}_{\mathsf{S}} = \hat{\rho}$. In general, $\mathsf{j}_{\rho_0}$ is a function of the two sets of angular coordinates $\hat{r}_1$ and $\hat{r}_2$ and the hyperspherical angle $\alpha$.

$$\mathsf{j}_{\rho_0}(\hat{r}_1, \hat{r}_2, \alpha) = \mathrm{Im}\left\{ \left(\Psi^+_{\mathrm{sc}}(\vec{r}_1, \vec{r}_2)\right)^\star \frac{d}{d\rho} \left(\Psi^+_{\mathrm{sc}}(\vec{r}_1, \vec{r}_2)\right) \right\} \Bigg|_{\rho=\rho_0} \tag{4.4}$$

The total cross section is obtained by integrating $\mathsf{j}_{\rho_0}$ (in the limit $\rho_0 \to \infty$) over the surface of the hypersphere and dividing by the incident flux.

$$\sigma_{\mathrm{total}} = \lim_{\rho_0 \to \infty} \frac{4\pi}{k_i^3} \int_{\mathsf{S}} \mathsf{j}_{\rho_0}(\hat{r}_1, \hat{r}_2, \alpha) d\mathsf{S} \tag{4.5}$$

The differential $d\mathsf{S}$ represents the surface differential of a hypersphere such that it is related to the full six-dimensional volume element by $d\mathsf{S}d\rho = dr_1^3 dr_2^3 = r_1^2 r_2^2 d\hat{r}_1 d\hat{r}_2 dr_1 dr_2$.

$$d\mathsf{S} \equiv r_1^2 r_2^2 d\hat{r}_1 d\hat{r}_2 \rho d\alpha \tag{4.6}$$

We can now write an expression for the total cross section as a surface integral in terms of the scattered wave $\Psi^+_{\mathrm{sc}}$. For later convenience, the Jacobian factor $(r_1, r_2)^2$ is associated with the scattered wave. We will take Equation 4.7 as our working definition of the total cross section.

$$\sigma_{\mathrm{total}} = \frac{4\pi}{k_i^3} \int_{\mathsf{S}} \mathrm{Im}\left\{ \left(r_1, r_2 \Psi^+_{\mathrm{sc}}(\vec{r}_1, \vec{r}_2)\right)^\star \frac{d}{d\rho} \left(r_1, r_2 \Psi^+_{\mathrm{sc}}(\vec{r}_1, \vec{r}_2)\right) \right\} \rho d\hat{r}_1 d\hat{r}_2 d\alpha \Bigg|_{\rho \to \infty} \tag{4.7}$$

The normalization in Equation 4.7 is for the initial state defined in Equation 3.7.

A more numerically stable method for calculating the total cross section comes from converting the surface integral in Equation 4.7 to a volume integral by applying Green's theorem.

$$\sigma_{\text{total}} = \frac{4\pi}{k_i^3} \int \text{Im} \left\{ \left( \Psi_{\text{sc}}^{+}(\vec{r}_1, \vec{r}_2) \right)^{\star} \nabla^2 \Psi_{\text{sc}}^{+}(\vec{r}_1, \vec{r}_2) \right\} dr_1^3 dr_2^3 \tag{4.8}$$

The operator $\nabla^2$ is the 6-dimensional Laplacian and the integration is over all space for both coordinates. For the case of the Temkin-Poet model, integration over the angular coordinates merely removes the spherical harmonics contained in $\Psi_{\text{sc}}^{+}$ leaving just the radial scattered wave $\psi_{\text{TP}}^{+}$.

$$\sigma_{\text{total}} = \frac{4\pi}{k_i^3} \int_0^{\infty} \text{Im} \left\{ \left( \psi_{\text{TP}}^{+}(r_1, r_2) \right)^{\star} \left( \frac{d^2}{dr_1^2} + \frac{d^2}{dr_2^2} \right) \psi_{\text{TP}}^{+}(r_1, r_2) \right\} dr_1 dr_2 \tag{4.9}$$

Equation 4.9 is the volume integral expression for the Temkin-Poet total cross section. Integration is from zero to infinity in both radial coordinates.

## 4.2 Channel Cross Sections

Channel cross sections $\sigma_n$ correspond to elastic scattering or excitations with one electron left behind in the $\phi_n$ bound state. To define them we will use the two-dimensional projection operator $\mathsf{P}_n(r_1, r_2)$.

$$\mathsf{P}_n(r_1, r_2) \equiv \mathsf{P}_n(r_1) + \mathsf{P}_n(r_2) - \mathsf{P}_n(r_1)\mathsf{P}_n(r_2) \tag{4.10}$$

Each one-dimensional projection operator $\mathsf{P}_n(r)$ projects on to the bound state $\phi_n(r)$.

$$\mathsf{P}_n(r) f(r) \equiv \phi_n(r) \int_0^{\infty} \phi_n(r') f(r') dr' \tag{4.11}$$

As indicated in Equation 3.8, the scattered wave can be completely described asymptotically as components for ionization and each bound state. Thus, the ionization component is the piece of the wave function that remains after all bound state components have been removed so we can *in principle* define a projection operator corresponding to ionization.

$$\mathsf{P}_{\text{ion}}(r_1, r_2) \equiv \mathbf{1} - \sum_{n=1}^{\infty} \mathsf{P}_n(r_1, r_2) \tag{4.12}$$

In order to use the projection operators we need an alternate expression for the total cross section. Any real potential can be added to the second derivatives inside the integrand in Equation 4.9 without changing the value of the cross section. For

1s $\rightarrow$ 1s elastic cross section (units of $a_0^2$)

| incident energy (eV) | 16.5 | 19.6 | 23.1 | 27.2 | 30.6 |
|---|---|---|---|---|---|
| ECS ($R_0 = 100a_0$) | 3.093 | 2.433 | 1.978 | 1.644 | 1.449 |
| Poet [26] | 3.103 | 2.443 | 1.987 | 1.651 | 1.456 |
| Burke and Mitchell [14] | 2.878 | 2.428 | 1.938 | 1.663 | 1.509 |

1s $\rightarrow$ 2s excitation cross section (units of $a_0^2$)

| incident energy (eV) | 16.5 | 19.6 | 23.1 | 27.2 | 30.6 |
|---|---|---|---|---|---|
| ECS ($R_0 = 100a_0$) | 0.441 | 0.355 | 0.277 | 0.211 | 0.172 |
| Poet [26] | 0.444 | 0.356 | 0.276 | 0.211 | 0.172 |
| Burke and Mitchell [14] | 0.627 | 0.347 | 0.302 | 0.211 | 0.157 |

Table 4.1: Elastic and first excitation cross sections for the Temkin-Poet model with singlet spin symmetry. Values calculated using exterior complex scaling (ECS) beyond $R_0 = 100a_0$ are given along with "exact" values calculated by Poet using a method specialized for the Temkin-Poet model. Results from an early close-coupling calculation by Burke and Mitchell are also shown. These values have not been multiplied by spin statistics factors.

instance, we can write an equivalent expression in terms of the $S$-wave hydrogen radial Hamiltonian in Equation 3.9 which will be denoted here by $\hat{H}_0$ so that $\hat{H}_0\phi_n = \varepsilon_n\phi_n$.

$$\sigma_{\text{total}} = -\frac{8\pi m}{\hbar^2 k_i^3}\int_0^\infty \text{Im}\left\{\left(\psi^+_{\text{TP}}(r_1,r_2)\right)^\star\left[\hat{H}_0(r_1)+\hat{H}_0(r_2)\right]\psi^+_{\text{TP}}(r_1,r_2)\right\}dr_1^3dr_2^3 \quad (4.13)$$

To arrive at the channel cross sections, we insert the identity operator $\mathbf{1}$ as the sum of all projection operators $\mathsf{P}_n$ including the ionization projection operator $\mathsf{P}_{\text{ion}}$. Since the projection operators all commute with the hydrogen Hamiltonian $\hat{H}_l$ and $\mathsf{P}_n(r_1,r_2)\mathsf{P}_{n'}(r_1,r_2) = \delta_{n,n'}\mathsf{P}_n(r_1,r_2)$ the total cross section is now a sum of individual "channel" cross sections.

$$\sigma_{\text{total}} = \sum_{n=1}^{\infty}\sigma_n + \sigma_{\text{ion}} \quad (4.14)$$

Each discrete channel cross section $\sigma_n$ can be calculated via an expression analogous to Equation 4.9 but with the projection operator $\mathsf{P}_n$ acting on the scattered wave.

$$\sigma_n \equiv \frac{4\pi}{k_i^3}\int_0^\infty \text{Im}\left\{\left(\mathsf{P}_n\psi^+_{\text{TP}}(r_1,r_2)\right)^\star\left[\frac{d^2}{dr_1^2}+\frac{d^2}{dr_2^2}\right]\left(\mathsf{P}_n\psi^+_{\text{TP}}(r_1,r_2)\right)\right\}dr_1dr_2 \quad (4.15)$$

We can immediately identify $\sigma_1$ as the elastic scattering cross section and each $\sigma_n$ for $n > 1$ as the cross section for excitation into the $\phi_n$ bound state.

The channel cross sections provide our first opportunity to judge the accuracy of the scattered wave calculated by exterior complex scaling. Accurate values for the channel cross sections have been calculated by R. Poet [26, 27]. Table 4.1 lists

singlet $\sigma_n$ (in units of $a_0^2$) for 14.14eV incident energy

| ECS beyond $R_0 =$ | $40a_0$ | $50a_0$ | $70a_0$ | $100a_0$ | $150a_0$ |
|---|---|---|---|---|---|
| total : | 4.53915 | 4.53914 | 4.53914 | 4.53913 | 4.53914 |
| $n = 1$ : | 3.88524 | 3.88523 | 3.88523 | 3.88522 | 3.88523 |
| $n = 2$ : | 0.50096 | 0.50096 | 0.50097 | 0.50096 | 0.50096 |
| $n = 3$ : | 0.09453 | 0.09453 | 0.09453 | 0.09453 | 0.09453 |
| $n = 4$ : | 0.02781 | 0.02839 | 0.02844 | 0.02844 | 0.02844 |
| $n = 5$ : | 0.00483 | 0.00963 | 0.01131 | 0.01134 | 0.01134 |
| $n = 6$ : | 0.00190 | 0.00152 | 0.00473 | 0.00544 | 0.00545 |

triplet $\sigma_n$ (in units of $a_0^2$) for 14.14eV incident energy

| ECS beyond $R_0 =$ | $40a_0$ | $50a_0$ | $70a_0$ | $100a_0$ | $150a_0$ |
|---|---|---|---|---|---|
| total : | 11.6240 | 11.6240 | 11.6241 | 11.6240 | 11.6241 |
| $n = 1$ : | 11.6142 | 11.6142 | 11.6143 | 11.6142 | 11.6143 |
| $n = 2$ : | 0.00938 | 0.00938 | 0.00939 | 0.00939 | 0.00939 |
| $n = 3$ : | 0.00027 | 0.00027 | 0.00027 | 0.00027 | 0.00027 |
| $n = 4$ : | 0.00003 | 0.00003 | 0.00003 | 0.00003 | 0.00003 |

Table 4.2: Total and several discrete channel cross sections for 14.14eV incident energy. Results are given for both singlet and triplet spin symmetries (spin statistics factors not included) from calculations using different size grids.

some of these for the elastic channel and first excitation channel along with values calculated using complex scaling beyond $100a_0$. Values are given for several energies above the ionization threshold. In all cases, the difference between Poet's values and those calculated here is better than 0.1%. This suggests that at least some scattering information can be obtained from a finite range, ECS transformed scattered wave.

The only systematic error in the ECS formalism comes from truncating the Coulomb potentials where the coordinates become complex. We expect that truncating the potentials might affect only those channels corresponding to bound states that extend beyond the range of the real coordinates. Total and several channel cross sections for an incident energy just 0.5 eV above the ionization threshold are listed in Table 4.2. Results from calculations using several values of the complex scaling point $R_0$ are given. The total and elastic scattering ($n = 1$) cross sections as well as the excitation cross sections up to $n = 3$ are essentially identical for $R_0 = 40a_0$ and beyond. For the singlet case the $n = 4$ cross section changes slightly for $R_0$ larger than $40a_0$ while the $n = 5$ and $n = 6$ cross sections change significantly.

Error in the wave function is mainly in the excitation channels for states that extend beyond where the Coulomb potential is truncated. Looking at Table 4.2, we see that if $R_0$ is $100a_0$ or larger the discrete channels up to $n = 5$ are accurately represented. The relative contributions of the excitation channels to the total wave function decrease rapidly as $n$ increases. Note that this decrease in the relative

contribution from the excitation channels is especially rapid in the triplet case. This is a unique characteristic of the Temkin-Poet model and will not be a feature of electron-hydrogen scattering. Channel cross sections converge rapidly as $R_0$ increases and we can assume that for $R_0$ of at least $100a_0$ the error from truncating the potentials is no worse than numerical error from using finite difference.

The rapid decrease in the channel cross sections as $n$ increases suggests that we might obtain accurate total ionization cross sections by subtracting the elastic and excitation channel cross sections from the total cross section. As we will see later, the ionization cross section is a small fraction of the total and, in some cases, subtracting channel cross sections up to $n = 6$ may not be enough to produce an accurate ionization cross section. If enough discrete channels can be accurately represented on the grid then subtracting channel cross sections from the total is the most accurate way to calculate a *total* ionization cross section. However, this does not lead to a method for producing differential cross sections. For that we will need a different approach.

## 4.3 Differential Cross Section for Ionization

The surface integral expression for the total cross section in Equation 4.7 provides a natural means for defining a differential cross section with respect to the four angular coordinates and the hyperspherical angle $\alpha$. We will soon see that the angle $\alpha$ parametrizes energy sharing between the two outgoing electrons. Consequently, the integrand in Equation 4.7 will lead to a cross section that is differential with respect to the energy of one electron as well as the directions of both electrons.

The greatest challenge in treating ionization is correctly describing energy sharing between the two outgoing electrons. Since there is no directional dependence in the Temkin-Poet model we can perform the trivial integration over the angular coordinates in Equation 4.7 and look at just the $\alpha$ dependence.

$$\sigma_{\text{total}} = \frac{4\pi}{k_i^3} \int_0^{\pi/2} \text{Im}\left\{ \left(\psi^+_{\text{TP}}(r_1, r_2)\right)^\star \frac{d}{d\rho} \left(\psi^+_{\text{TP}}(r_1, r_2)\right) \right\} \rho d\alpha \Bigg|_{\rho\to\infty} \tag{4.16}$$

The integrand in Equation 4.16 defines a differential cross section with respect to $\alpha$, but only in the limit $\rho \to \infty$. Under exterior complex scaling we know the wave function only on a finite region, so we need a means of extracting the $\rho \to \infty$ limit from a finite region of space. To this end, let us first define a generalized flux $\mathsf{f}_{\rho_0}(\alpha)$ evaluated at a finite hyperradius $\rho_0$.

$$\mathsf{f}_{\rho_0}(\alpha) = \text{Im}\left\{ \rho \left(\psi^+_{\text{TP}}(r_1, r_2)\right)^\star \frac{d}{d\rho} \left(\psi^+_{\text{TP}}(r_1, r_2)\right) \right\} \Bigg|_{\rho=\rho_0} \tag{4.17}$$

The $\mathsf{f}_{\rho_0}(\alpha)$ are always symmetric about $\alpha = 45^o$ just like the absolute value of the scattered wave plotted along arcs of constant $\rho$ in Figure 3.6. Examples of $\mathsf{f}_{\rho_0}(\alpha)$ calculated from the same wave function, but at different values of $\rho_0$ are shown in Figure 4.1. The plots in Figure 4.1 show the behavior of the two distinctive components of

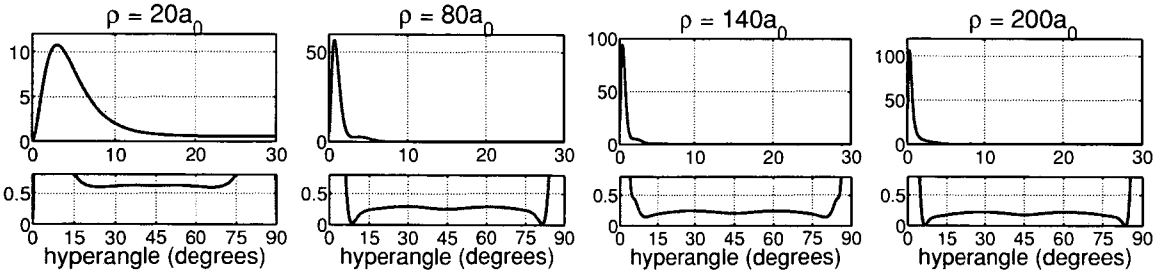


Figure 4.1: Flux, as a function of the hyperangle, calculated for various values of the hyperradius $\rho$ in the Temkin-Poet model with incident energy of 20.4 eV. The flux is symmetric about $45^o$. The upper figures zoom in on the discrete channel contributions near the edges while the lower figures show the smaller ionization component.

the flux (discrete channel peaks near the edges and the ionization component in the middle) as the flux surface moves outward in the hyperradius.

As $\rho_0$ increases the width of the discrete channel peaks decrease and more of the ionization component is uncovered. Unlike the peaks shown in Figure 3.6, the peaks in the flux increase monotonically with $\rho_0$ due to the factor of $\rho$ in Equation 4.17. This must be so because conservation of flux in each channel requires that the areas under the peaks remain constant. In the limit $\rho_0 \to \infty$ the discrete channel flux will become delta functions in $\alpha$ at zero and $90^o$ and $\mathsf{f}_{\rho_0}$ will consist only of ionization flux except for infinitesimally small regions near the edges. Thus, we can use $\mathsf{f}_{\rho_0}(\alpha)$ to define a differential cross section $\frac{d\sigma_{\rm ion}(\alpha)}{d\alpha}$ for ionization that is valid everywhere except very near $\alpha$ equals zero and $90^o$.

$$\sigma_{\rm ion} = \int_0^{\pi/2} \frac{d\sigma_{\rm ion}(\alpha)}{d\alpha} d\alpha \,, \qquad \frac{d\sigma_{\rm ion}(\alpha)}{d\alpha} \simeq \lim_{\rho_0 \to \infty} \frac{4\pi}{k_i^3} \mathsf{f}_{\rho_0}(\alpha) \tag{4.18}$$

This differential cross section is supposed to give the total ionization cross section when integrated over the full range of $\alpha$. The conditional equality in the definition of $\frac{d\sigma_{\rm ion}(\alpha)}{d\alpha}$ reflects the fact that $\mathsf{f}_{\rho_0}(\alpha)$ formally contains discrete channel contributions at $\alpha$ equals zero and $90^o$. In principle, we could eliminate the discrete channel contributions by forcing $\frac{d\sigma_{\rm ion}(\alpha)}{d\alpha}$ to be zero at $\alpha$ equal to zero and $90^o$ *after* taking the $\rho_0 \to \infty$ limit.

To obtain the differential cross section defined in Equation 4.18 we need to somehow take the $\rho_0 \to \infty$ limit of the flux from a wave function known only on a finite region of space. If we substitute the asymptotic form for the ionization part of the scattered wave given in Equation 3.11 for $\psi^+_{\rm TP}$ in Equation 4.17 we see that the ionization part of the flux $\mathsf{f}_{\rho_0}(\alpha)$ approaches its asymptotic limit like $\frac{1}{\rho_0}$.

$$\text{for large } \rho: \qquad \mathsf{f}_\rho(\alpha) \sim \mathsf{f}_\infty(\alpha) + \frac{A(\alpha)}{\rho} \tag{4.19}$$

Thus, if we calculate $\mathsf{f}_{\rho_0}(\alpha)$ for two or more values of $\rho_0$ that are large enough for this form to apply we can estimate the flux in the $\rho_0 \to \infty$ limit by fitting Equation 4.19 to the calculated $\mathsf{f}_{\rho_0}$.

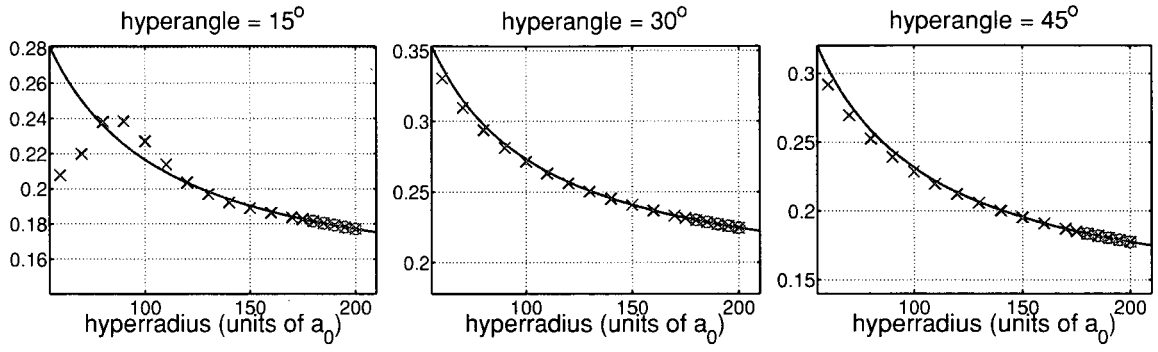


Figure 4.2: Comparison of calculated flux to a $\frac{1}{\rho}$ extrapolation curve in the Temkin-Poet model with incident energy of 20.4 eV. The comparision is done for three different values of the hyperangle. The solid line is the $\frac{1}{\rho}$ least-squares fit and the markers are the values of the flux from the wave function. The values of the flux that were used to produce the least-squares fit are circled.

Examples of fitting the functional form in Equation 4.19 to the $f_{\rho_0}$ from a particular scattered wave are shown in Figure 4.2. In this example the function $A(\alpha)$ and the $\rho_0 \to \infty$ limit of the flux were estimated by a least-squares fit using $f_{\rho_0}$ calculated at five evenly spaced values of $\rho_0$ ranging from $180a_0$ to $200a_0$. The curves in Figure 4.2 are the resulting fits, as functions of $\rho$, plotted for three different values of $\alpha$. For comparison, $f_{\rho_0}$ calculated at several values of $\rho_0$ are also shown. Only the last five directly calculated $f_{\rho_0}$ shown in Figure 4.2 were used for the least-squares fit.

Other $f_{\rho_0}$ (evaluated at smaller $\rho_0$) are plotted to show how well the $f_{\rho_0}$ fit Equation 4.19 for different hyperangles. At hyperangles of $30^o$ and $45^o$ the flux fits the form in Equation 4.19 very well beyond $\rho \approx 100a_0$. However, at a hyperangle of $15^o$ the flux does not reach this form until somewhere beyond $150a_0$. In general, the form in Equation 4.19 is reached more slowly for $\alpha$ near zero and $90^o$. This is primarily due to "contamination" from discrete channels, which do not extrapolate in this way, near the edges of the grid.

In the true $\rho \to \infty$ limit, as $\rho_0$ increases the discrete channel peaks in the $f_{\rho_0}$ become confined to infinitesimal regions of $\alpha$ near the endpoints. This behavior cannot be replicated by extrapolation. Consequently, the region over which $\frac{d\sigma_{\text{ion}}(\alpha)}{d\alpha}$ is valid is restricted to the range of $\alpha$ over which the $f_{\rho_0}$ used for the extrapolation do not contain appreciable amounts of discrete channel contributions. In other words, extrapolation does not provide a means for further "uncovering" the ionization flux. Thus, we cannot calculate $\frac{d\sigma_{\text{ion}}(\alpha)}{d\alpha}$ in this manner over the full range of $\alpha$. Figure 4.3 shows three different $\frac{d\sigma_{\text{ion}}(\alpha)}{d\alpha}$ obtained by extrapolation from $f_{\rho_0}$ from three different, disjoint ranges of $\rho_0$. They all have large oscillations near the edges that come from trying to extrapolate the discrete channel components using Equation 4.19. Each extrapolated curve is valid only over the region of $\alpha$ where it is smooth.

One might think that we could use the projection operators defined in Equation 4.10 to remove the discrete channel components from the scattered wave leaving behind a pure ionization wave. However, if we were to actually try projecting out

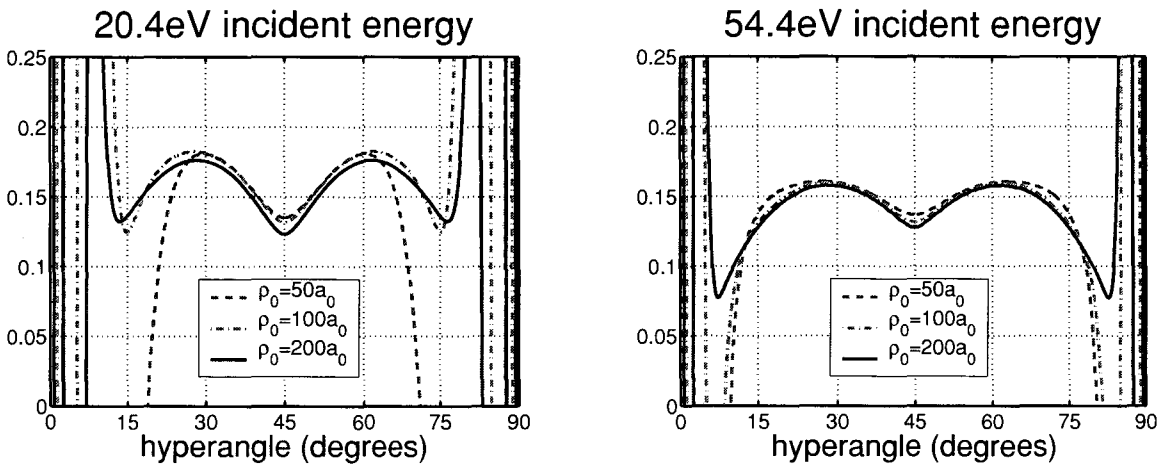


Figure 4.3: Comparision of flux extrapolated from different ranges of the hyperradius in the Temkin-Poet model at two different incident energies. Each extrapolation was from flux calculated at three different values of the hyperradius over a $10a_0$ range. The curves are identified by the largest hyperradius that was used for the extrapolation.

all of the discrete channel components (or, at least all of those that fit on the grid) we would find that the remaining wave function does not have the expected smooth behavior over the full range of $\alpha$. This is because the discrete channel projection operators project out states that are not eigenfunctions of the full Hamiltonian. They are, instead, eigenfunctions of an "asymptotic" Hamiltonian describing a hydrogen atom and a free electron. All of the dynamics of the true ionization wave are governed by the full Hamiltonian and it cannot be assumed to be orthogonal to the asymptotic forms for the discrete channels. For this reason, distinguishing between the ionization wave and the discrete channels really does rely on spatial separation of the different components. Because we know the wave function only over a finite region of space, projecting out discrete channels from the scattered wave will not improve our ability to calculate $\frac{d\sigma_{\rm ion}(\alpha)}{d\alpha}$ near $\alpha$ equals zero and $90^o$.

Formally, there are an infinite number of discrete channels present in the scattered wave. The larger the energy quantum number $n$ the greater the extent of the bound state. That means for any finite grid, no matter how large, we can always find a maximum $n$ for which the $n^{th}$ and higher bound states extend beyond the range of the grid. These bound states cannot be correctly represented on the grid and the corresponding discrete channel components of the scattered wave cannot be accurately removed using projection operators.

Removing the first few discrete channel components would certainly make the oscillations in Figure 4.3 much less dramatic, but they would still exist over the same range of $\alpha$ because it is actually the higher excitation channels that are the limiting factor. Furthermore, the rate at which the ionization component reaches the asymptotic form in Equation 3.11 is no faster than the rate at which the discrete channel components "uncover" the ionization wave. This means that even after as many discrete channels as possible are removed, the flux from the "uncovered" ionization wave

may still not fit Equation 4.19.

We can see in Figure 4.3 that the size of the region over which $\frac{d\sigma_{\text{ion}}(\alpha)}{d\alpha}$ is valid depends on the distance at which the $\mathsf{f}_{\rho_0}$ used in the extrapolation were calculated. For the lower energy example in Figure 4.3 the $\frac{d\sigma_{\text{ion}}(\alpha)}{d\alpha}$ extrapolated from $100a_0$ and $200a_0$ are valid between $\alpha = 15^o$ and $\alpha = 75^o$, while the $\frac{d\sigma_{\text{ion}}(\alpha)}{d\alpha}$ extrapolated from $50a_0$ is valid only between $\alpha = 30^o$ and $\alpha = 60^o$. In the higher energy example the regions of validity are somewhat larger. Over the range of $\alpha$ in which all of the $\frac{d\sigma_{\text{ion}}(\alpha)}{d\alpha}$ are valid there is quite good agreement among the different extrapolated results. The plots in Figure 4.3 suggest that, within the range of $\alpha$ that extrapolation is valid, the error due to extrapolation in $\rho$ is about 5%.

## 4.4 Single Differential Cross Section

The hyperspherical angle $\alpha$ has no direct physical meaning so differential cross sections with respect to $\alpha$ are of little practical use. Instead, we are interested in a differential cross section that describes how energy is shared between the two outgoing electrons. The single differential cross section (SDCS) is a differential cross section with respect to the energy of one electron. It is directly related to $\frac{d\sigma_{\text{ion}}(\alpha)}{d\alpha}$ because $\alpha$ parametrizes the energy distribution between the two electrons.

We associate two momenta $k_1$ and $k_2$ with the two outgoing electrons. The momenta are constrained by conservation of energy so that $\frac{\hbar^2}{2m}(k_1^2 + k_2^2) = E$. Looking at the final state semi-classically, we know that the electron with the larger momentum is moving faster so, at some time following ionization, that electron will be further from the nucleus than the "slow" electron will be. If we trace the trajectory at large distances for this semi-classical picture in the two-dimensional radial plane it should follow a fixed ray for some hyperspherical angle $\alpha$.

So, intuitively we expect that for large $\rho$ the hyperspherical angle $\alpha$ parametrizes the energy sharing between the two outgoing electrons.

$$\lim_{\rho\to\infty} \tan^{-1}\left(\frac{k_2}{k_1}\right) \to \tan^{-1}\left(\frac{r_2}{r_1}\right) = \alpha \tag{4.20}$$

The relation in Equation 4.20 was shown formally by Rudge [34] by a stationary phase argument. Using this relation, a differential cross section for electron-impact ionization that is a function of $\alpha$ can be converted to a cross section that is differential in the energy of one of the two electrons.

The individual electrons' momenta are proportional to $\sin\alpha$ and $\cos\alpha$ for large $\rho$ and their kinetic energies are $\varepsilon_1 = E\cos^2\alpha$ and $\varepsilon_2 = E\sin^2\alpha$. To convert from a differential with respect to $\alpha$ to a differential with respect to the energy of the second electron we divide $\frac{d\sigma_{\text{ion}}(\alpha)}{d\alpha}$ by the quantity $\frac{d\varepsilon_2}{d\alpha} = 2E\sin\alpha\cos\alpha$. Energy differential cross sections $\frac{d\sigma_{\text{ion}}(\varepsilon)}{d\varepsilon}$ will be symmetric about $\varepsilon = \frac{E}{2}$ just as the $\frac{d\sigma_{\text{ion}}(\alpha)}{d\alpha}$ are symmetric about $\alpha = 45^o$. By convention, the SDCS is the energy differential cross section

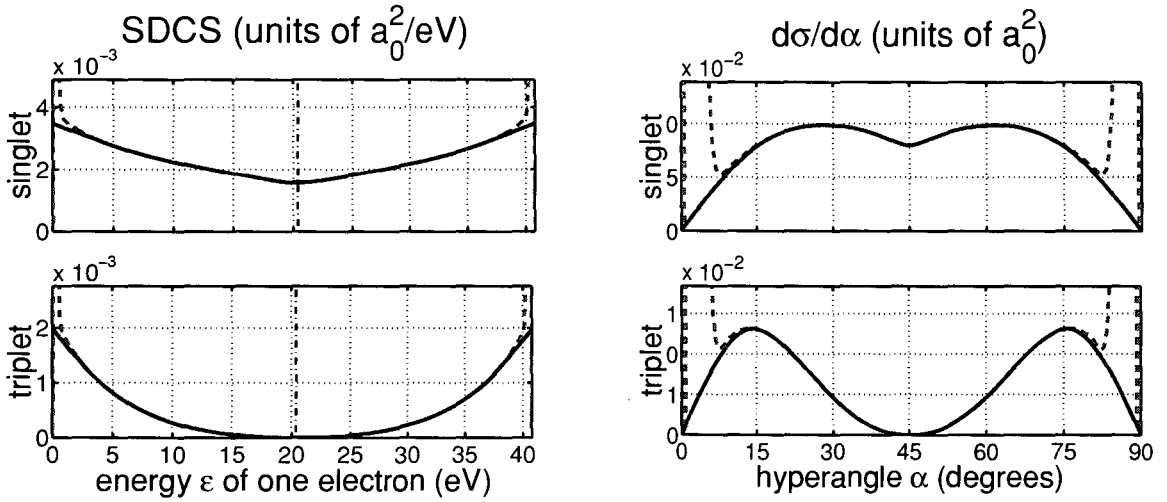


Figure 4.4: Differential cross sections in the Temkin-Poet model for 54.4 eV incident energy. The upper plots are the singlet cross section multiplied by a spin statistics factor of $\frac{1}{4}$, the lower are the triplet multiplied by $\frac{3}{4}$. The "raw" $\frac{d\sigma}{d\alpha}$ (dashed lines on the right) come directly from extrapolating the flux in $\rho$ and are converted to "raw" $\frac{d\sigma}{d\varepsilon}$ (dashed lines on the left). The noise at the edges of the "raw" $\frac{d\sigma}{d\varepsilon}$ is replaced by a linear extrapolation in $\varepsilon$ to produce the final SDCS (solid lines on the left). The final SDCS were transformed back to a final $\frac{d\sigma_{\rm ion}(\alpha)}{d\alpha}$ (solid lines on the right).

defined for $\varepsilon$ between zero and $\frac{E}{2}$.

$$\sigma_{\rm ion} = \int_0^{E/2} \frac{d\sigma_{\rm ion}(\varepsilon)}{d\varepsilon} d\varepsilon \tag{4.21}$$

The total ionization cross section is obtained by integrating the SDCS over half of the energy range so there is an additional factor of two contained in the conversion from $\frac{d\sigma_{\rm ion}(\alpha)}{d\alpha}$ to the SDCS, $\frac{d\sigma_{\rm ion}(\varepsilon)}{d\varepsilon}$.

$$\left.\frac{d\sigma_{\rm ion}(\varepsilon)}{d\varepsilon}\right|_{\varepsilon = E\sin^2\alpha} = \frac{1}{E\sin\alpha\cos\alpha}\frac{d\sigma_{\rm ion}(\alpha)}{d\alpha} \tag{4.22}$$

Equation 4.22 along with Equations 4.18 and 4.17 define the energy sharing SDCS in terms of a flux calculated as a function of $\alpha$.

We are still faced with the problem that extrapolation in $\rho$ produces a differential cross section that is invalid near $\alpha = 0$ and $\alpha = 90^o$. This means that we cannot calculate the SDCS for the case where one of the electrons carries most of the energy. We know that the correct SDCS should be a very smooth function of $\varepsilon$. In fact, the SDCS can be assumed to be linear near $\varepsilon = 0$.

The two differential cross sections $\frac{d\sigma_{\rm ion}(\varepsilon)}{d\varepsilon}$ and $\frac{d\sigma_{\rm ion}(\alpha)}{d\alpha}$ for both singlet and triplet spin symmetries at an incident energy of 54.4 eV are shown in Figure 4.4. The dashed lines are the "raw" results obtained directly from extrapolation in $\rho$. These lines contain large amplitude noise from the discrete channels near the edges. In both

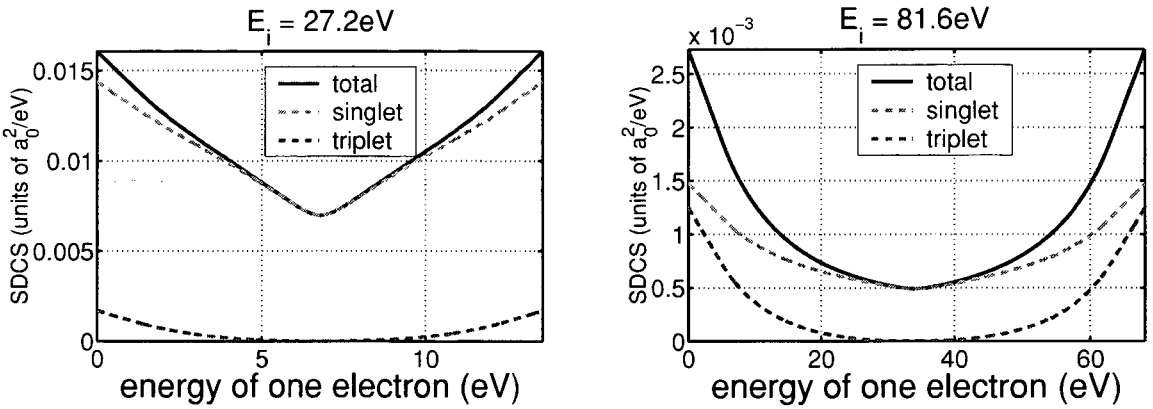


Figure 4.5: Examples of the singlet, triplet, and total SDCS at incident energies of 27.2 eV and 81.6 eV. The singlet and triplet cross sections have been multiplied by the appropriate spin statistics factors.

spin symmetries the SDCS is essentially linear near where the discrete channel noise begins. This suggests that we can estimate the SDCS for small $\varepsilon$ by replacing the discrete channel noise with a linear extrapolation in $\varepsilon$. The solid lines in the left panels of Figure 4.4 are the final SDCS obtained by replacing the "raw" SDCS for small $\varepsilon$ with a linear fit in $\varepsilon$ that is matched to the "raw" SDCS at the lowest value of $\varepsilon$ where the extrapolated results can be assumed to be reasonably accurate.

Choosing the value of $\varepsilon$ at which to perform the linear match is, admittedly, a somewhat arbitrary process and there is really no way to quantify the accuracy of the procedure. In practice, we choose the matching point by looking at plots similar to Figure 4.4 and choosing a value of $\varepsilon$ just inside where the oscillations are visible.

In Figure 4.4 we see that the fraction of the energy range occupied by discrete channel noise in the "raw" SDCS is much smaller than the fraction of the total $\alpha$ range occupied by the noise in the "raw" $\frac{d\sigma_{\rm ion}(\alpha)}{d\alpha}$. This is because converting from a function of $\alpha$ to a function of $\varepsilon$ compresses the function near the ends. Consequently, the fraction of the SDCS that comes from the linear fit is much smaller than might be expected from looking at plots of the "raw" $\frac{d\sigma_{\rm ion}(\alpha)}{d\alpha}$. Converting the final SDCS back to a differential with respect to $\alpha$ shows what the true $\frac{d\sigma_{\rm ion}(\alpha)}{d\alpha}$ should look like over the full range of $\alpha$.

## 4.5 Temkin-Poet Results

Examples of the final SDCS for both singlet and triplet spin symmetries are shown in Figure 4.5. The total SDCS is the sum of the singlet and triplet SDCS with statistical weights of $\frac{1}{4}$ multiplying the singlet cross section and $\frac{3}{4}$ multiplying the triplet cross section. All of the SDCS are symmetric and very smooth with the minimum value at $\frac{E}{2}$ and the maximum value at zero and $E$. These general characteristics of the SDCS will carry over to electron-hydrogen scattering. The SDCS for the triplet case are zero at $\varepsilon = \frac{E}{2}$ because the triplet radial wave functions are anti-symmetric.

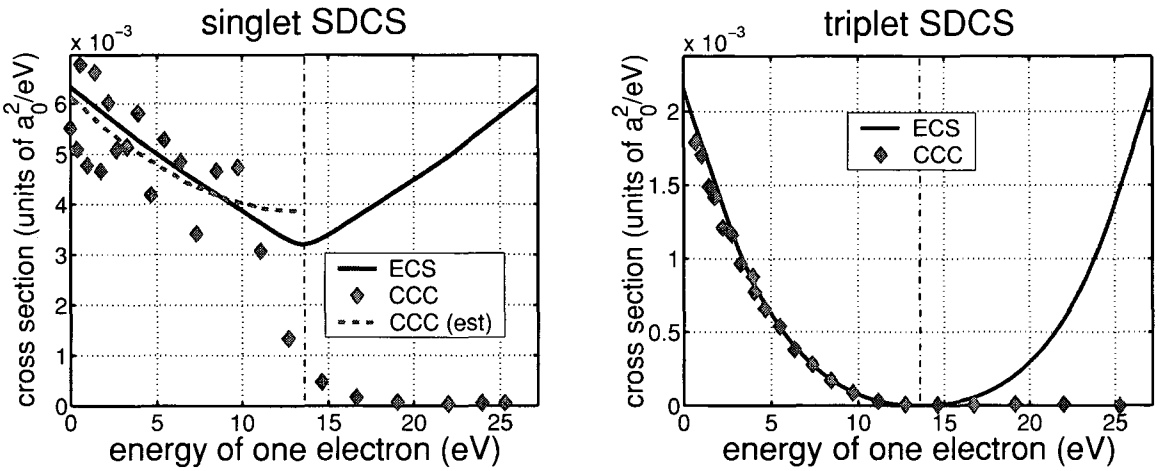


Figure 4.6: Comparison of convergent close-coupling [6] and exterior complex scaling results for the singlet and triplet SDCS in the Temkin-Poet model at 40.8 eV incident energy. The ECS results (solid lines) are shown over the full energy range (0 to 27.2 eV) to illustrate the symmetry in the method. They are normalized so that the total ionization cross section is the integral from 0 to $E/2 = 13.6$ eV. The CCC data (diamonds) are not symmetric about $E/2$. In the singlet case the CCC data has large oscillations so it is replaced by an integral preserving estimate (dashed line) which is defined between 0 and $E/2$.

Overall, the triplet SDCS is much smaller than the singlet SDCS. In fact, all inelastic processes, including ionization, in the Temkin-Poet model are dominated by the singlet spin symmetry. This characteristic is unique to two-dimensional models such as Temkin-Poet and will not carry over to electron-hydrogen scattering.

Singlet and triplet SDCS for 40.8 eV incident energy are compared in Figure 4.6 with results calculated by Igor Bray [6] using the convergent close-coupling (CCC) method. CCC is very good for calculating discrete channel cross sections for electron-atom scattering. It also has shown promise for calculating total ionization cross sections. However, it has, so far, been unable to produce correct differential ionization cross sections, even in the Temkin-Poet model, for incident energies below 100 eV. The SDCS produced by CCC are always asymmetric. If the method produced SDCS that were correct only from zero to $\frac{E}{2}$ then the calculated cross section in the upper-half of the energy range would be irrelevant. This is the case for the triplet spin symmetry, but not for the singlet spin symmetry.

Bray claims that the calculated values in the singlet case oscillate about the correct SDCS and he replaces them with a smooth estimate of the true SDCS between zero and $\frac{E}{2}$. The properties of the singlet and triplet SDCS calculated in the CCC method for two-dimensional models is discussed in reference [30]. The ability of the CCC method to calculate the triplet SDCS is made possible only because the triplet SDCS is zero at $\frac{E}{2}$. This does not provide much hope for CCC being generally successful at calculating differential ionization cross sections because no SDCS in a real system is zero for equal energy sharing.

| $E_0$ | 20.4eV | 27.2eV | 40.8eV | 54.4eV | 68.0eV | 81.6eV |
|---|---|---|---|---|---|---|
| $\sigma_{\text{total}}$ | 2.9989 | 2.2373 | 1.4816 | 1.0842 | 0.8381 | 0.6713 |
| $\sigma_1$ | 2.3077 | 1.6437 | 1.0826 | 0.8106 | 0.6421 | 0.5256 |
| $\sigma_2$ | 0.3354 | 0.2113 | 0.1008 | 0.0580 | 0.0375 | 0.0263 |
| $\sigma_3$ | 0.0865 | 0.0565 | 0.0267 | 0.0151 | 0.0096 | 0.0067 |
| $\sigma_4$ | 0.0343 | 0.0223 | 0.0109 | 0.0061 | 0.0039 | 0.0027 |
| $\sigma_5$ | 0.0170 | 0.0116 | 0.0055 | 0.0031 | 0.0019 | 0.0013 |
| $\sigma_6$ | 0.0097 | 0.0066 | 0.0031 | 0.0018 | 0.0011 | 0.0008 |
| $\sigma_{\text{total}} - \sum_{n=1}^{6} \sigma_n$ | 0.2083 | 0.2846 | 0.2520 | 0.1896 | 0.1420 | 0.1080 |
| $\int_0^{E/2} \frac{d\sigma_{\text{ion}}(\varepsilon)}{d\varepsilon} d\varepsilon$ | 0.2028 | 0.2849 | 0.2520 | 0.1899 | 0.1423 | 0.1077 |

Table 4.3: Integral cross sections for the Temkin-Poet model with singlet spin symmetry, spin statistcs factors are not included. Total and discrete channel cross sections are shown. Also listed are total ionization cross sections calculated both by subtracting discrete channel cross sections from the total and by integrating the SDCS.

Having calculated the SDCS we can now integrate them to obtain total ionization cross sections. First, it should be noted that volume integral formulations for calculating integral cross sections are much less susceptible to numerical error than first producing, then integrating differential cross sections. Still, integrating the calculated SDCS allows for interesting comparisons using the channel cross sections discussed earlier in this chapter.

Total cross sections $\sigma_{\text{total}}$ and channel cross sections $\sigma_n$ up to $n = 6$ for several incident energies are listed in Table 4.3. As mentioned before, we can obtain the total ionization cross section $\sigma_{\text{ion}}$ by subtracting all of the $\sigma_n$ from $\sigma_{\text{total}}$. The remainders after subtracting the first six $\sigma_n$ from the $\sigma_{\text{total}}$ are listed in Table 4.3. These provide an upper bound for the $\sigma_{\text{ion}}$, assuming the $\sigma_n$ themselves are accurate. We can see from Table 4.3 that in order to obtain the $\sigma_{\text{ion}}$ to three or more significant figures we will probably need $\sigma_n$ beyond $n = 6$. However, for $n$ this high the accuracy of the $\sigma_n$ is in doubt. For comparison, the $\sigma_{\text{ion}}$ obtained by integrating the SDCS are also listed. The $\sigma_{\text{ion}}$ obtained in the two different ways compare quite well with most differences being less than 0.3% and the largest difference being less than 3%.

# Chapter 5

# Six-Dimensional Wave Function for Electron-Hydrogen Scattering

Theoretical treatment of electron-hydrogen scattering requires computing a six-dimensional scattered wave function with outgoing wave boundary conditions. As in the two-dimensional Temkin-Poet model, the scattering boundary conditions can be simplified by using exterior complex scaling of the radial coordinates. Methods used to calculate the Temkin-Poet wave function are readily extended to a partial wave expansion of the six-dimensional scattered wave. Computing the scattered wave requires calculating a large number of two-dimensional radial functions to form its partial wave expansion. These are solutions to sets of coupled differential equations that are solved using an iterative algorithm on a distributed memory parallel computer.

## 5.1 Coupled Equations for the Scattered Wave

Scattering of an electron from a hydrogen atom is described by the six-dimensional, two-electron scattered wave $\Psi^+_{\rm sc}(\vec{r}_1, \vec{r}_2)$ defined in Equation 2.6. Just as in the Temkin-Poet model, the asymptotic boundary condition on $\Psi^+_{\rm sc}$ (Equation 2.10) can be simplified by exterior complex scaling (ECS) of the radial coordinates. Extending the methods from Chapter 3 to the six-dimensional scattered wave equation is straightforward after first expanding the wave functions in partial waves.

### 5.1.1 Partial wave expansion of the wave function

We expand the wave functions $\Psi^0_{k_i}$ and $\Psi^+_{\rm sc}$ in terms of two-particle, coupled spherical harmonics $\mathcal{Y}^{LM}_{l_1,l_2}$ which are functions of the four angular coordinates. The $\mathcal{Y}^{LM}_{l_1,l_2}$ are eigenfunctions of total angular momentum, $L$, of the system and its projection, $M$, along the $z$ axis as well as the individual electron angular momenta $l_1$ and $l_2$.

$$\mathcal{Y}^{LM}_{l_1,l_2}(\hat{r}_1, \hat{r}_2) = \sum_{m_1,m_2} \langle l_1 l_2 m_1 m_2 | LM \rangle \mathrm{Y}_{l_1 m_1}(\hat{r}_1) \mathrm{Y}_{l_2 m_2}(\hat{r}_2) \tag{5.1}$$

They are related to ordinary spherical harmonics by the Clebsch-Gordan coefficients $\langle l_1 l_2 m_1 m_2 | LM \rangle$. Clebsch-Gordan coefficients are discussed in Zare [39] and most quan-

tum mechanics text books. Some properties of the $\mathcal{Y}^{LM}_{l_1,l_2}$ useful for this particular application are mentioned in Appendix F.

The term representing the initial state is $\Psi^0_{k_i}$, defined in Equation 2.5 as the anti-symmetrized product of a plane wave and the ground state of hydrogen. Using the expansion, in ordinary spherical harmonics, of a plane wave (Equation 4.3) we immediately write an analytic expression for the partial wave expansion of $\Psi^0_{k_i}$.

$$\Psi^0_{k_i}(\vec{r}_1,\vec{r}_2) = \sum_{L=0}^{\infty} \frac{i^L\sqrt{2\pi(2L+1)}}{r_1 r_2 k_i} \begin{pmatrix} \phi_{nl}(r_1)\hat{j}_L(k_i r_2)\mathcal{Y}^{L0}_{0,L}(\hat{r}_1,\hat{r}_2) + \\ (-1)^S \hat{j}_L(k_i r_1)\phi_{nl}(r_2)\mathcal{Y}^{L0}_{L,0}(\hat{r}_1,\hat{r}_2) \end{pmatrix} \tag{5.2}$$

Since the coordinate system is chosen so the $z$ axis lies along the incident direction, only $m = 0$ spherical harmonics are present in Equation 4.3. Also, the ground state of hydrogen $\Phi_{1s}$ (see Equation 4.1) is spherically symmetric. So, the projections along the $z$ axis of both individual electron angular momenta $l_1$ and $l_2$ as well as the total angular momentum $L$ are zero and Equation 5.2 contains only terms with $M = 0$. This is a consequence of the cylindrical symmetry of the system for scattering from a spherically symmetric target.

Solving the scattered wave equation means calculating the two-dimensional radial functions $\psi^L_{l_1 l_2}$ in a partial wave expansion of $\Psi^+_{sc}$. This expansion also contains only terms for which $M = 0$ because $M$ is a conserved quantum number of the system.

$$\Psi^+_{sc}(\vec{r}_1,\vec{r}_2) = \frac{1}{r_1 r_2} \sum_{L,l_1,l_2} \psi^L_{l_1 l_2}(r_1,r_2)\mathcal{Y}^{L0}_{l_1,l_2}(\hat{r}_1,\hat{r}_2) \tag{5.3}$$

Four continuous angular variables have been replaced by three discrete angular momentum quantum numbers $l_1$, $l_2$, and $L$. That leaves only two continuous variables, $r_1$ and $r_2$, the same as for the model problem in Chapter 3. However, there are an infinite number of the radial functions $\psi^L_{l_1 l_2}$ and they will be solutions to sets of *coupled*, two-dimensional differential equations.

Since $\Psi^+_{sc}(\vec{r}_1,\vec{r}_2)$ is an outgoing wave each individual radial function $\psi^L_{l_1 l_2}(r_1,r_2)$ in its partial wave expansion has outgoing wave boundary conditions similar to those in the Temkin-Poet model. Application of exterior complex scaling, as given in Equation 3.12 and illustrated in Figure 3.1, to the partial wave expansion simplifies the boundary conditions on each individual radial function. Under ECS, every $\psi^L_{l_1 l_2}(r_1,r_2)$ is transformed in to a function that decays exponentially for either $r_1$ or $r_2$ larger than the complex scaling point $R_0$.

### 5.1.2 Coupled differential equations

Total angular momentum of the system is a conserved quantity so there will be no coupling between partial waves with different values of $L$. For each total angular momentum $L$ and spin $S$ there is a separate, independent set of coupled equations. In most of what follows the quantum numbers $L$ and $S$ are treated as parameters that are frequently suppressed. Calculating physical quantities requires assembling all of the separate $L$ and $S$ components of the wave functions and/or cross sections.

To arrive at the coupled equations we substitute the partial wave expansions for $\Psi^+_{sc}$ (Equation 5.3) and $\Psi^0_{k_i}$ (Equation 5.2) into the scattered wave equation in Equation 2.6. We then multiply both sides of the equation on the left by some spherical harmonic $\mathcal{Y}^{L0}_{l_1',l_2'}$ and integrate over the four angular variables. The attractive potentials between the nucleus and each electron have no angular dependence and the $\mathcal{Y}^{L0}_{l_1,l_2}$ are eigenfunctions of the kinetic energy operators. So, integration is trivial for all terms of the operator $(E-\hat{H})$ except the repulsive, two-electron potential. Since the $\mathcal{Y}^{L0}_{l_1,l_2}$ are orthonormal all of the one-electron terms are non-zero only when $l_1' = l_1$ and $l_2' = l_2$. Together, when acting on a radial function, they can be expressed as a partial wave radial Hamiltonian for hydrogen, $\hat{H}_l(r) \equiv -\frac{\hbar^2}{2m}\frac{d^2}{dr^2} + \frac{l(l+1)\hbar^2}{2mr^2} - \frac{e^2}{r}$.

$$\langle l_1' l_2' L0|\hat{H}|l_1 l_2 L0\rangle = \left(\hat{H}_{l_1}(r_1) + \hat{H}_{l_2}(r_2)\right)\delta_{l_1 l_1'}\delta_{l_2 l_2'} + \langle l_1 l_2||l_1' l_2'\rangle_L \tag{5.4}$$

Dirac notation is used to represent integration over only the angles and not over the radial coordinates. Shorthand notation $\langle l_1 l_2||l_1' l_2'\rangle_L$ in the last term of Equation 5.4 represents the multipole expansion of the two-electron potential $\frac{e^2}{|\vec{r}_1-\vec{r}_2|}$. It is a function of both $r_1$ and $r_2$ and is discussed, in more detail, in Appendix F.

$$\langle l_1 l_2||l_1' l_2'\rangle_L \equiv \langle l_1 l_2 L0|\frac{e^2}{|\vec{r}_1-\vec{r}_2|}|l_1' l_2' L0\rangle = e^2\sum_\lambda C^{L,\lambda}_{l_1 l_2 l_1' l_2'}\frac{r_<^\lambda}{r_>^{\lambda+1}} \tag{5.5}$$

Here, $r_<$ refers to the smaller and $r_>$ to the larger of $r_1$ or $r_2$. Formulas for calculating the coefficients $C^{L,\lambda}_{l_1 l_2 l_1' l_2'}$ are given by Percival and Seaton [24]. The index $\lambda$ ranges over a finite subset of the non-negative integers. For the special case $l_1 = l_1' = l_2 = l_2' = 0$, $\langle 00||00\rangle_0 = \frac{e^2}{r_>}$ which is the two-electron potential in the Temkin-Poet model.

Two radial functions $\psi^{L'}_{l_1' l_2'}$ and $\psi^L_{l_1 l_2}$ are coupled only if $\langle l_1 l_2 L0|\frac{e^2}{|\vec{r}_1-\vec{r}_2|}|l_1' l_2' L'0\rangle$ is nonzero. This term is nonzero only if $L' = L$. When $L' = L$ it is always nonzero for any $(l_1, l_2)$ and $(l_1', l_2')$ pairs for which the sums $l_1 + l_2$ and $l_1' + l_2'$ are either both even or both odd integers. So, all partial waves for a particular $L$ with the same parity are coupled together. Using Equations 5.4 and 5.5 we write, for each $L$, the coupled radial differential equations that come from the scattered wave equation.

$$\left(E - \hat{H}_{l_1}(r_1) - \hat{H}_{l_2}(r_2)\right)\psi^L_{l_1 l_2}(r_1, r_2) - \sum_{l_1', l_2'}\langle l_1 l_2||l_1' l_2'\rangle_L \psi^L_{l_1', l_2'}(r_1, r_2) = \chi^L_{l_1 l_2}(r_1, r_2) \tag{5.6}$$

We now define the radial functions $\psi^L_{l_1 l_2}$ as the outgoing solutions to the coupled equations in Equation 5.6. The functions $\chi^L_{l_1 l_2}$, defined in Equation 5.7, are radial functions from the partial wave expansion of $\left(\hat{H} - E\right)\Psi^0_{k_i}$.

$$\chi^L_{l_1 l_2} = \frac{i^L}{k_i}\sqrt{2\pi(2L+1)}\left\{\left(\langle l_1 l_2||0L\rangle_L - \frac{e^2}{r_2}\delta_{l_1 0}\delta_{l_2 L}\right)\phi_{nl}(r_1)\hat{j}_L(k_i r_2) + (-1)^S\,(1 \Longleftrightarrow 2)\right\} \tag{5.7}$$

Since only $\chi^L_{l_1 l_2}$ with even parity exist (see Appendix F), the $(l_1, l_2)$ pairs that contribute to the expansion of $\Psi^+_{sc}$ are restricted to those for which $l_1 + l_2 + L$ is an even integer. The sum in Equation 5.6 involving the coupling potential $\langle l_1 l_2||l_1' l_2'\rangle_L$ is over all $l_1', l_2'$ pairs in the expansion, including the case $l_1' = l_1$ and $l_2' = l_2$.

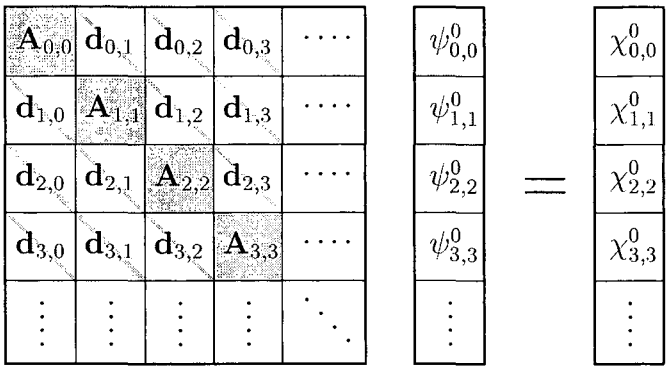

Block-matrix structure of the coupled equations (Equation 5.6) using $L = 0$ as an example. The off-diagonal blocks $\mathbf{d}_{l_1,l_2}$ are diagonal matrices representing the coupling potential. The diagonal blocks $\mathbf{A}_{l,l}$ are sparse, not diagonal, matrices similar to those in the Temkin-Poet problem.

Figure 5.1: Block structure for the coupled equations

## 5.2 Iterative Solution of the Coupled Equations

There is an infinite number of sets of coupled equations for the different values of $L$ and each of these couples an infinite number of partial waves with different $(l_1, l_2)$ pairs. In practice, of course, we solve the coupled equations for only as many $L$ values as needed for numerical convergence. Likewise, each individual $L$ coupled equation is limited to a finite number of $(l_1, l_2)$ pairs. Coupling even a few partial waves produces a very large system of linear equations that must be solved by an iterative algorithm.

### 5.2.1 Matrix equation

Just as was done for the Temkin-Poet wave function in Chapter 3, each complex scaled radial function is calculated directly onto a two-dimensional radial grid using finite difference approximations for the differential operators. The finite difference representation of the coupled equations forms a matrix with the block structure illustrated in Figure 5.1. That example shows the case $L = 0$ where $l_1 = l_2$ for all partial waves and there is an obvious ordering for the $(l_1, l_2)$ pairs. Each block in the array of radial functions corresponds to the values of $\psi^L_{l_1 l_2}$ on the two-dimensional radial grid for a particular $(l_1, l_2)$ pair. Likewise, the blocks in the array on the right-hand side are the $\chi^L_{l_1 l_2}$, defined in Equation 5.7, evaluated on the grid.

The diagonal blocks are finite difference matrix representations of the operators $E - \hat{H}_{l_1}(r_1) - \hat{H}_{l_2}(r_2) - \langle l_1 l_2 || l_1, l_2 \rangle_L$. These matrices have exactly the same sparsity structure, shown in Figure D.1, as the Temkin-Poet matrix. In fact, the $L = l_1 = l_2 = 0$ diagonal block is the Temkin-Poet matrix. The off-diagonal blocks, on the other hand, are just the coupling potentials evaluated on the grid so each of these is a diagonal matrix.

If we remove the off-diagonal blocks *i.e.*, set $\langle l_1 l_2 || l_1' l_2' \rangle_L = 0$ for $(l_1', l_2') \neq (l_1, l_2)$, then the matrix is block diagonal and we have a large set of *uncoupled* equations for each $\psi^L_{l_1 l_2}$. Solving each of these uncoupled equations is comparable to solving the Temkin-Poet model problem. In Chapter 4 we found that we need the radial functions at distances of at least $100 a_0$ to get meaningful ionization information. Calculating accurate radial functions that extend this far requires on the order of 240,000 grid

points. Solving a Temkin-Poet problem of this size already uses substantial computational resources. Solving the entire set of *uncoupled* equations is merely a matter of performing multiple calculations of that same size. However, keeping ten or so partial waves in a set of *coupled* equations forms a linear system of two or three million.

### 5.2.2 Iterative algorithm with pre-conditioner

Linear systems this large must be solved using an iterative algorithm. Convergence properties of iterative algorithms are governed largely by the eigenvalue spectrum of the matrix. Since the six-dimensional Hamiltonian should have a spectrum similar to that of the Temkin-Poet Hamiltonian we can apply the lessons learned in using an iterative algorithm for solving the Temkin-Poet model toward developing a method for iteratively solving the coupled equations. In particular, it is reasonable to expect the conjugate gradient squared (CGS) algorithm to converge to the solution provided an effective pre-conditioner is used.

The matrix structure shown in Figure 5.1 suggests using the uncoupled equations as a block-diagonal pre-conditioner. That means that each pre-conditioning step in the CGS algorithm, given in Figure E.2, requires solving the uncoupled equations, but with different right-hand sides. The effectiveness of using the uncoupled equations as a pre-conditioner depends upon the two-dimensional radial Hamiltonians in the diagonal blocks having an eigenvalue spectrum similar to that of the six-dimensional Hamiltonian. This is a reasonable expectation because the basic characteristics of the eigenvalue spectrum is determined by the radial dependence of the Hamiltonian. For instance, the bound state energies of hydrogen are determined solely by the one-dimensional radial Hamiltonians for hydrogen. With exterior complex scaling, the movement of the continuum spectrum into the lower-half of the complex plane is determined by the scaling of the radial coordinates. Therefore, the uncoupled equations should have the same inelastic thresholds as, and a similar eigenvalue spectra to, the coupled equations.

### 5.2.3 Convergence of iterative algorithm

Indeed, the uncoupled equations are a sufficiently robust pre-conditioner to make the CGS algorithm converge to solution to the coupled equations for any value of $L$ over the range of incident energies considered here. Convergence of the CGS algorithm on the coupled equations for a few representative $L$ at two different energies is shown in Figure 5.2.

Error in the iterative solutions is measured by substituting the calculated radial functions at each iteration into the left side of Equation 5.6. The difference between the left and right sides of Equation 5.6 gives a two-dimensional "residual" function for each partial wave. Integrating the modulus-square of each residual produces "partial wave errors". Total error for a set of coupled partial waves is defined to be the sum of these partial wave errors. In all cases, convergence of the CGS algorithm is well behaved with very little sign of instability and the solution can be improved to arbitrary accuracy.

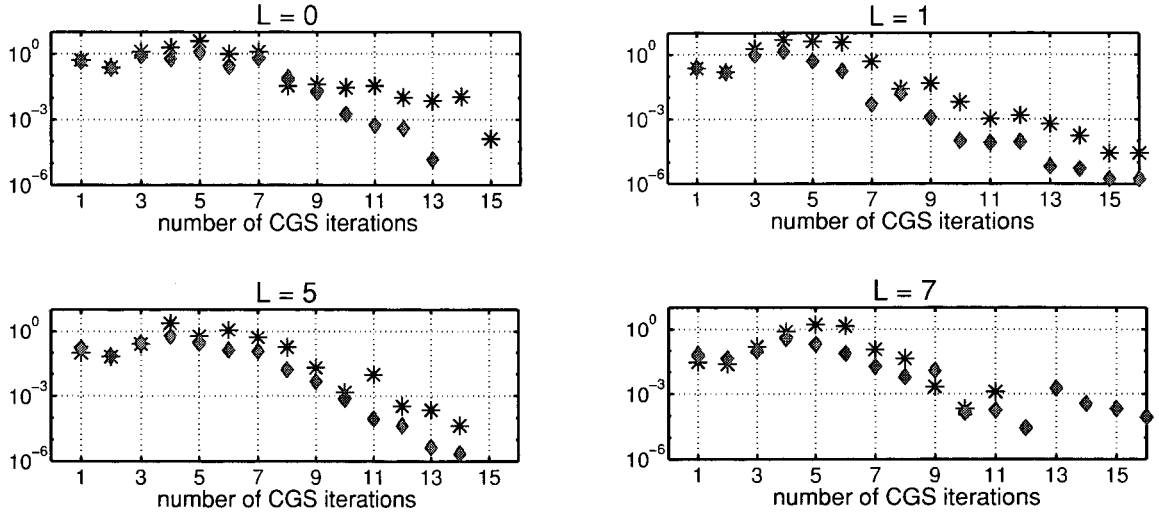


Figure 5.2: Convergence of the CGS algorithm for the coupled equations with singlet spin symmetry for various total angular momenta $L$. Error of the calculated scattered wave is plotted for incident energies of 17.6 eV (asterisks) and 25 eV (diamonds).

In principle, the convergence rate depends on the number of partial waves kept in the coupled equations. However, once the most important partial waves are included adding a few more that are less important has little effect on convergence. All of the coupling potentials are built from terms that look like $\frac{r_<^\lambda}{r_>^{\lambda+1}}$ and are peaked along the ray $r_1 = r_2$. Therefore, the strength of the coupling depends on the magnitudes of the radial functions near $r_1 = r_2$ as well as on the coupling potentials themselves.

Less important radial functions *i.e.*, ones with relatively small magnitudes near $r_1 = r_2$, add only a small amount of coupling to the other partial waves. Triplet radial functions with $l_1 = l_2$ have significantly smaller ionization components than do their singlet counterparts. For this reason, convergence of the coupled equations is typically more rapid for the triplet spin symmetry. Convergence also tends to be faster at higher energies.

Solution to the uncoupled equations with the original right-hand side is used as the starting point for the iterative algorithm. Typically, the error actually increases slightly for the first few iterations before reaching a point where it then decreases fairly reliably. This is due to an initial redistribution of flux in the ionization region of the radial functions. This can be seen in Figure 5.3 which shows solutions to the uncoupled equations along with converged solutions to the coupled equations.

In the $L = 0$ *uncoupled* equations the $(l_1, l_2) = (0, 0)$ radial function (*i.e.*, the Temkin-Poet wave function) carries most of the ionization flux. Iterating to arrive at a solution to the *coupled* equations removes flux from this partial wave and redistributes it to the higher angular momentum partial waves. Ultimately, the $(1, 1)$ radial function has the largest ionization component of the singlet, $L = 0$ partial waves. We see similar behavior for $L = 2$ where the $(1, 1)$ radial function is largest initially. The magnitude of the $(1, 1)$ radial function decreases while the magnitudes

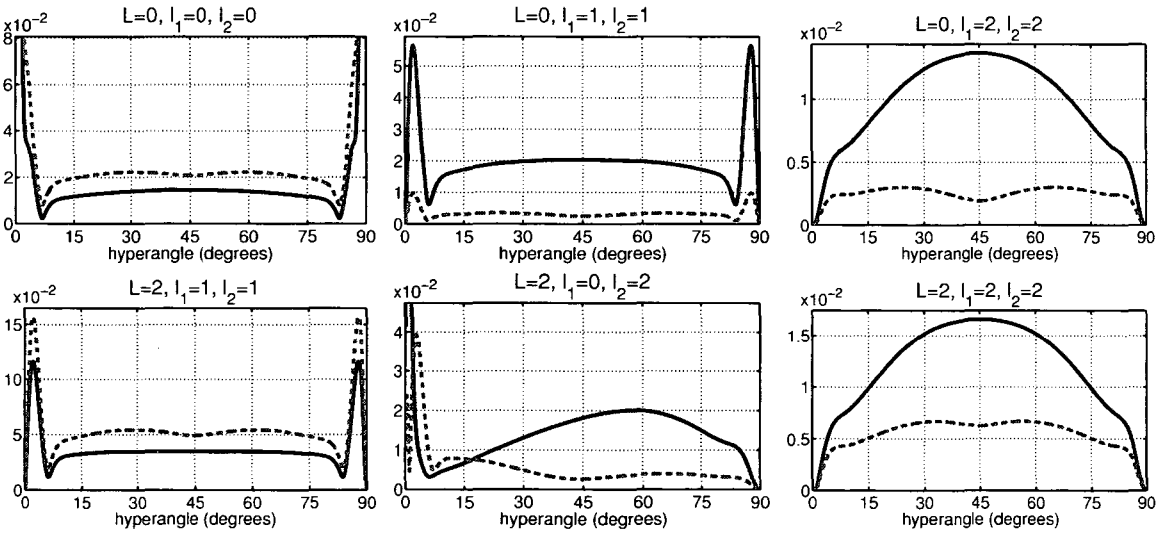


Figure 5.3: Comparison of solutions to the coupled and uncoupled equations for singlet spin symmetry and 25 eV incident energy. The magnitudes of the radial functions at a hyperradius of $100a_0$ are shown. Dashed lines are the solutions to the uncoupled equations and solid lines are the solutions to the coupled equations.

of the others increase. Eventually the combination of $(0,2)$ and its mirror image $(2,0)$ is the dominate $L = 2$ partial wave.

### 5.2.4 Parallel implementation

Each iteration of the CGS algorithm requires two applications of the pre-conditioner and two matrix-vector multiplies with the full matrix representation of the coupled equations. A key advantage of solving for the radial functions directly onto a grid is that potentials are represented by diagonal matrices. This means that inclusion of the coupling potentials in the full matrix-vector multiply is relatively inexpensive. Each coupling term requires exactly $N$ (complex) multiplies and adds, where $N$ is the number of two-dimensional radial grid points.

Most of the time used for solving the coupled equations is spent on applying the pre-conditioner. Each application of the pre-conditioner is equivalent work to solving the Temkin-Poet model problem for each partial wave. As mentioned in Chapter 3 and Appendix E, the Temkin-Poet model was also solved using the CGS iterative algorithm. Therefore, the method for solving the coupled equations actually uses the CGS algorithm at two levels. The coupled equations are solved iteratively using the CGS algorithm with the two pre-conditioning steps for each outer iteration requiring solutions to two-dimensional radial equations. These are, themselves, solved using low-order finite difference matrices as pre-conditioners to iteratively solve high-order finite difference matrix equations.

Since the work needed to couple partial waves is a small fraction of the total work, this method makes efficient use of distributed memory, massively parallel supercom-

puters. The block structure of the full matrix suggests a natural level of parallelism for solving the coupled equations. Each partial wave is assigned to a separate group of processors. Application of the pre-conditioner and the block-diagonal portion of the matrix-vector multiply are then accomplished independently within each group of processors. Significant communication between groups of processors is needed only when adding the coupling terms in the full matrix-vector multiplies.

By solving the uncoupled equations in parallel, application of the pre-conditioner takes the same amount of time required to solve just one uncoupled equation. According to the table in Figure E.1 the most time-consuming step in solving each uncoupled equation is the $LU$ factorization. The $LU$ factors depend only on the matrix and not on the right-hand side so they will be the same for each iteration. Saving the $LU$ factors after the first pre-conditioning step significantly reduces the work required for each subsequent application of the pre-conditioner.

## 5.3 Partial Wave Radial Functions

Formally, calculating the complete wave function requires solving an infinite number of coupled equations, each of which couples an infinite number of partial waves. In practice, of course, we must put a maximum on the values of $L$ for which we solve the coupled equations and we must limit the number of partial waves coupled for each individual $L$. The number of partial waves coupled together determines the cost of solving the coupled equations. It is, therefore, beneficial to make sure that the most important partial waves are the ones included first in the calculation. For this reason, we want to choose partial waves, at least roughly, in their order of relative importance. To choose an ordering for the partial waves we should understand the basic properties of the different radial functions.

In the Temkin-Poet model the scattered wave was either symmetric or anti-symmetric with respect to interchange of the radial coordinates. The same symmetry property for the six-dimensional scattered wave, $\Psi^+_{\rm sc}(\vec{r}_2,\vec{r}_1) = (-1)^S\Psi^+_{\rm sc}(\vec{r}_1,\vec{r}_2)$, leads to more complicated symmetry rules for the radial functions (see Appendix F).

$$\psi^L_{l_2l_1}(r_2,r_1) = (-1)^S\psi^L_{l_1l_2}(r_1,r_2) \tag{5.8}$$

When $l_1 = l_2$ the radial function $\psi^L_{l_1l_2}$ has the same symmetry property as the Temkin-Poet wave function. A symmetric and an anti-symmetric example of $L = 2$ radial functions are shown in Figure 5.4. For both examples $l_1 = l_2 = 2$ so the dominant discrete channel component that can be seen along the $r_1$ and $r_2$ axes is excitation of the 3d state of hydrogen. As in the Temkin-Poet model, any triplet partial wave with $l_1 = l_2$ contributes negligibly to ionization because of a "trough" that exists along the ray $r_1 = r_2$. Since $l_1 = l_2$ for every $L = 0$ partial wave, the entire set of $L = 0$ triplet partial waves plays an insignificant role in ionization.

Unlike the Temkin-Poet model, there exist radial functions in the partial wave expansion of $\Psi^+_{\rm sc}(\vec{r}_1,\vec{r}_2)$ that have no symmetry themselves. Examples of these are shown in Figure 5.5. In these examples the discrete channels are noticeably different on the two axes. The dominant discrete channel component along the $r_2$ axis is

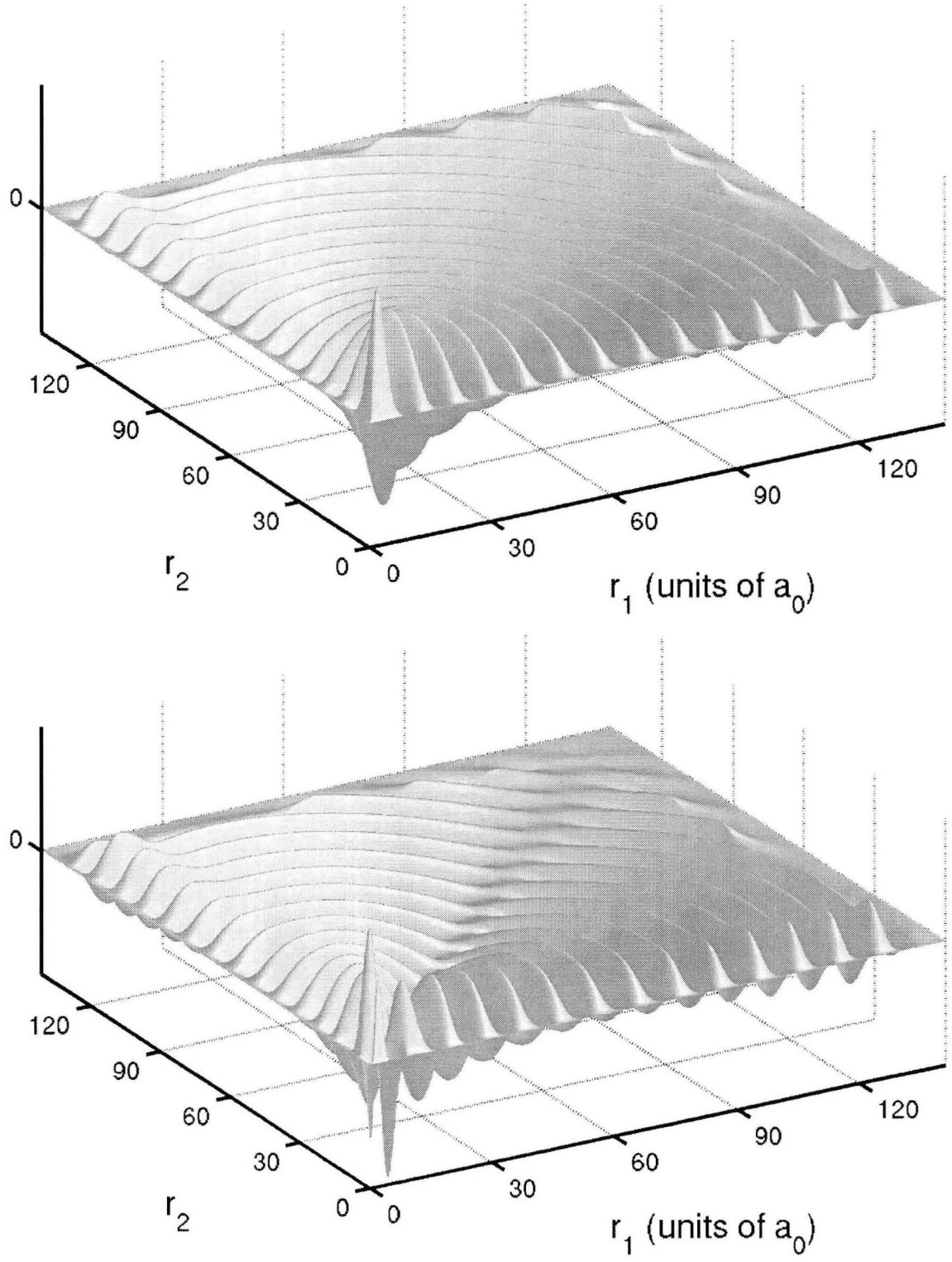


Figure 5.4: $L = 2$ and $l_1 = l_2 = 2$ radial functions for electron-hydrogen scattering at 17.6 eV incident energy. The upper picture shows the symmetric singlet radial function and the lower picture shows the anti-symmetric triplet radial function.

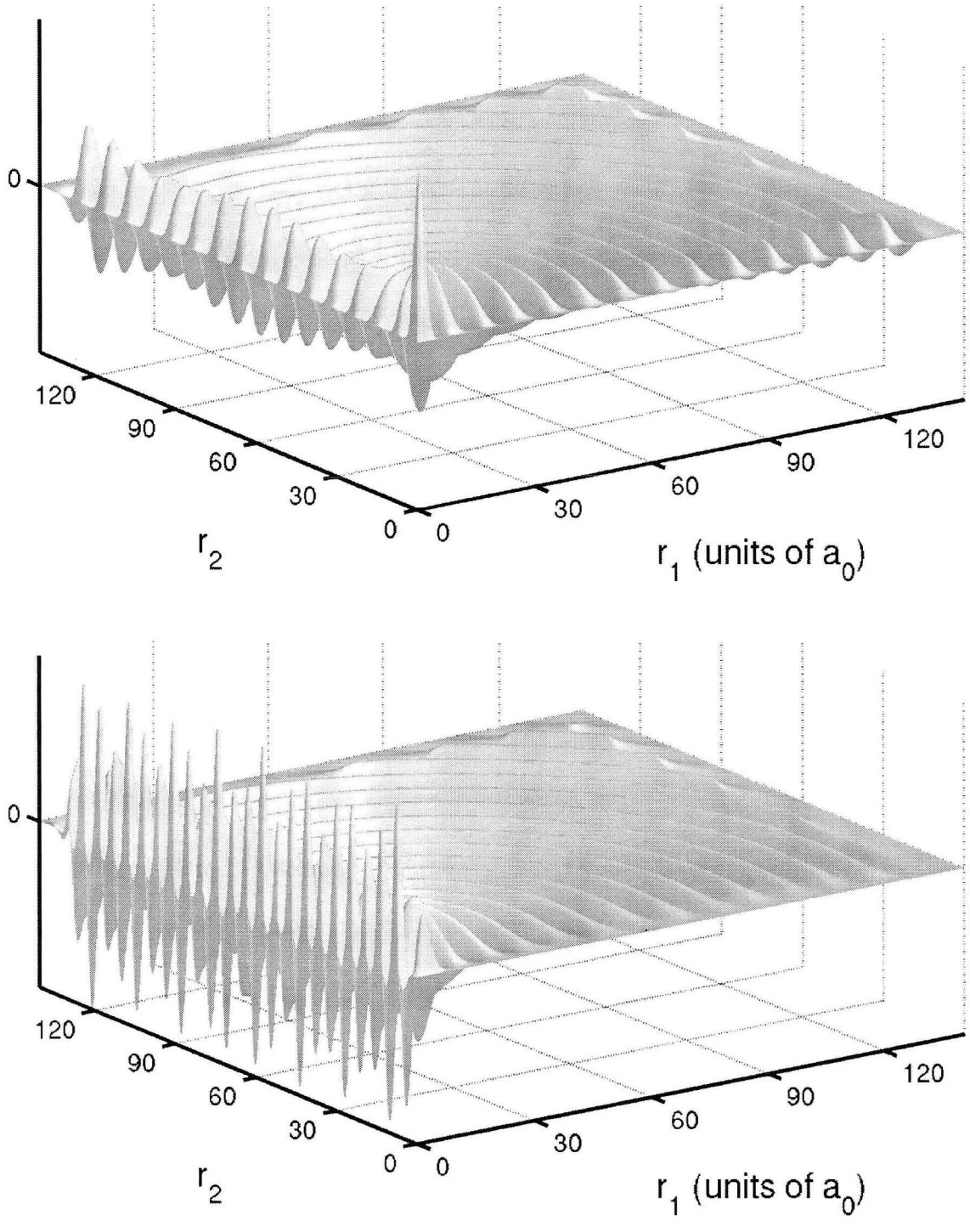


Figure 5.5: Asymmetric radial functions for electron-hydrogen scattering at 17.6 eV incident energy and singlet spin symmetry. The upper picture shows $L = 1$, $l_1 = 1$, $l_2 = 2$ and the lower picture shows $L = 3$, $l_1 = 0$, $l_2 = 3$.

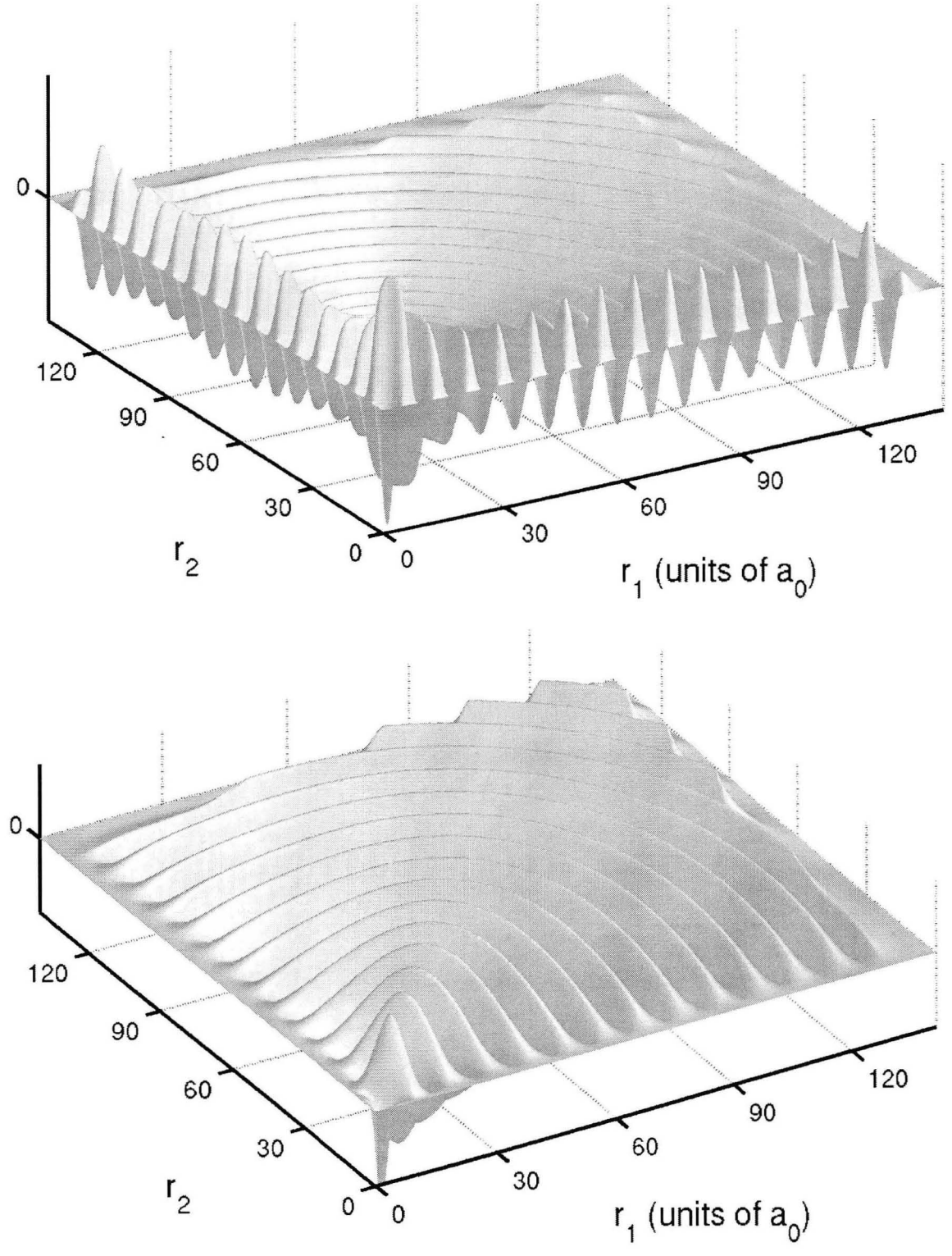


Figure 5.6: $L = 2$ symmetric radial functions for electron-hydrogen scattering at 17.6 eV incident energy. The upper picture shows the $l_1 = l_2 = 1$ radial function and the lower picture shows the $l_1 = l_2 = 3$ radial function.

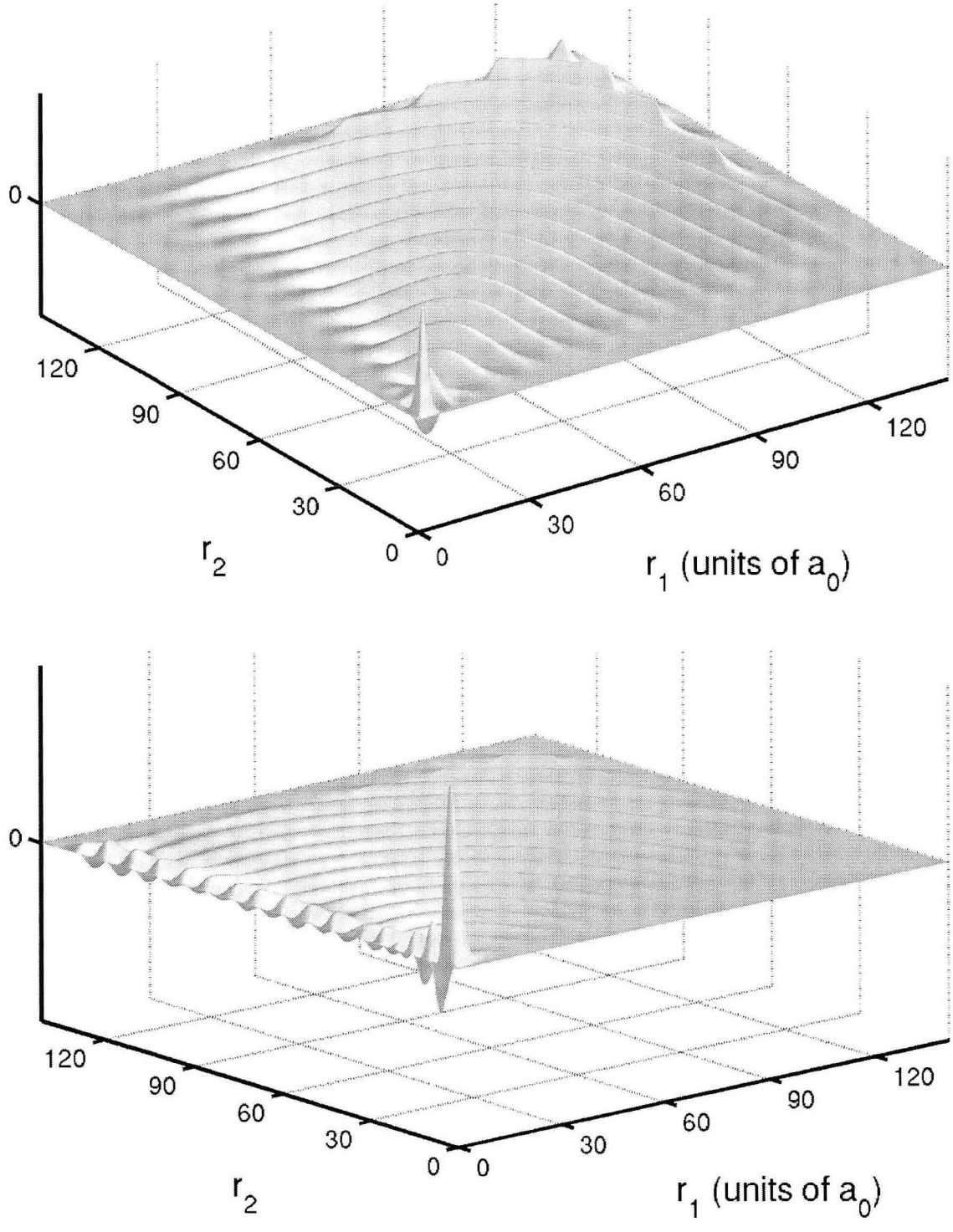


Figure 5.7: $L = 4$ radial functions for electron-hydrogen scattering at 17.6 eV incident energy and singlet spin symmetry. The upper picture shows the $l_1 = l_2 = 5$ radial function and the lower picture shows the $l_1 = 1$, $l_2 = 5$ radial function.

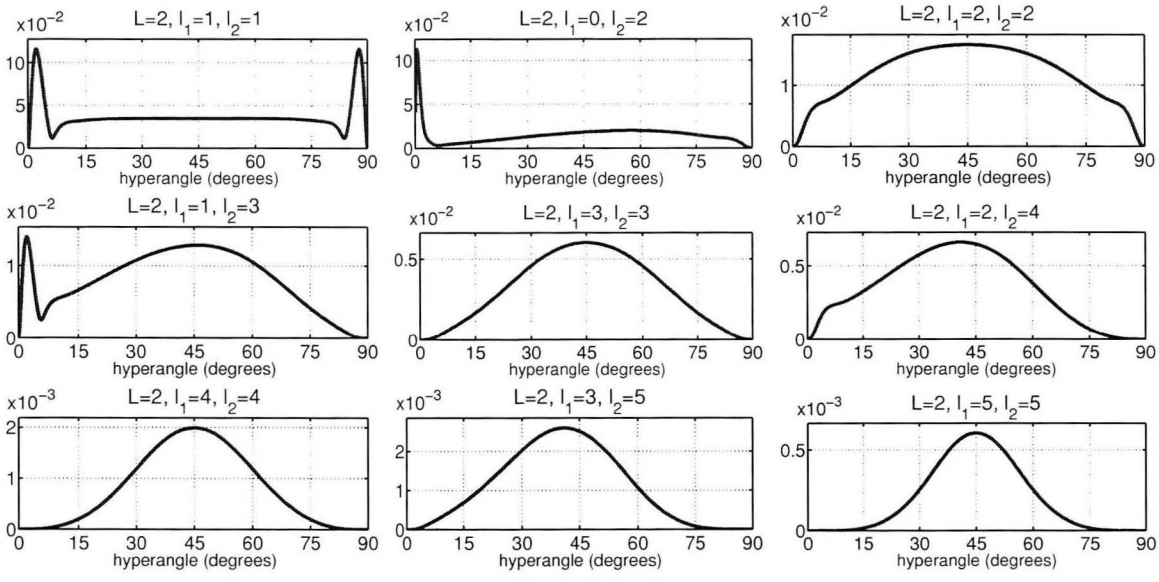


Figure 5.8: Magnitudes of several $L = 2$ radial functions along an arc of hyperradius $100a_0$. Examples shown are for singlet spin symmetry and 25 eV incident energy.

determined by the value of $l_1$ and vice-versa. For instance, the upper picture in Figure 5.5 corresponds to $l_1 = 1$ and $l_2 = 2$ so excitation of the 2p state is visible along the $r_2$ axis and excitation of the 3d state is visible along the $r_1$ axis. Similarly, the lower picture with $l_1 = 0$ and $l_2 = 3$ has an elastic scattering component along the $r_2$ axis with an emerging 4f excitation component barely visible along the $r_1$ axis.

For any $\psi^L_{l_1 l_2}$ with $l_1 \neq l_2$ there is a complementary radial function $\psi^L_{l_2 l_1}$ such that the *sum* of the two is either symmetric or anti-symmetric. If we include some $\psi^L_{l_1 l_2}$ for $l_1 \neq l_2$ then we must be sure to also include $\psi^L_{l_2 l_1}$ in order to maintain the symmetry of the entire partial wave expansion. However, the radial functions $\psi^L_{l_1 l_2}$ and $\psi^L_{l_2 l_1}$ contain the same information so there is no need to explicitly store both.

When solving the coupled equations on a parallel computer each group of processors is assigned an $(l_1, l_2)$ pair with $l_1 \leq l_2$. If $l_1 \neq l_2$ then that group is responsible for adding the couplings from both $\psi^L_{l_1 l_2}$ and $\psi^L_{l_2 l_1}$ Thus, except for $L = 0$, the number of partial wave terms coupled is actually larger than the number of processor groups used for the calculation. Also, when gauging the importance of an $(l_1, l_2)$ partial wave with $l_1 \neq l_2$ it is best to consider the combined contribution from $\psi^L_{l_1 l_2}$ and $\psi^L_{l_2 l_1}$.

The relative importance of different partial waves for $L = 2$ is illustrated in Figure 5.8. A "rule-of-thumb" for ordering partial waves is that those corresponding to larger angular momentum have less importance, this does not necessarily hold for very small angular momenta. This "rule" applies similarly to both the total and the individual angular momenta. For the energies considered here, the $L = 2$ sets of partial waves contribute most for the singlet spin symmetry and the $L = 3$ sets contribute most for triplet spin symmetry. As $L$ increases beyond these maxima the relative importance of the corresponding sets of partial waves decreases monotonically. This suggests that ordering sets of partial waves for each $L$ by increasing $L$ is reasonable assuming that

more than the first four values of $L$ will be used.

Obtaining each set of $L$ partial waves is an independent calculation so, deciding where to truncate the expansion in $L$ is a matter of adding calculations for increasingly large $L$ until sufficient convergence is achieved. Deciding which $(l_1, l_2)$ pairs to keep in the coupled equations for each $L$ requires more thought. All partial waves for a particular $L$ are coupled so one cannot easily add another term to the expansion to see if the results change. If more partial waves are added to an already converged set then the iterative algorithm must be re-applied to the full, larger set of partial waves.

If an individual angular momentum for a partial wave is large then the dominant discrete channel component along the appropriate axis is excitation to a high-energy state. These components have much smaller magnitudes than those for elastic scattering and excitation of low-energy states. Examples of symmetric radial functions for two different individual angular momenta are pictured in Figure 5.6. The $l_1 = l_2 = 1$ case has excitation of the 2p state clearly visible along both axes while the $l_1 = l_2 = 3$ case does not appear to have any discrete channel components. In actuality, excitation of the 4f state is present, but is not strong enough to have "emerged" from the ionization component before $120a_0$. Examples with individual angular momenta of five are shown in Figure 5.7. In the symmetric case ($l_1 = l_2 = 5$) no discrete channels are visible and the radial function appears to be purely ionization. The asymmetric example has $l_1 = 1$ so excitation of the 2s state is visible along the $r_2$ axis.

The ordering used for $L = 2, 3$ and 4 is indicated in Figure 5.9. Two selection rules, that govern which $(l_1, l_2)$ partial waves exist for a particular $L$, determine the patterns formed on the $l_1, l_2$ matrices. First, the sum of $l_1$ and $l_2$ must have the same even/odd parity as $L$ (see Appendix F). Second, the difference between $l_1$ and $l_2$ must not exceed $L$ *i.e.*, $|l_2 - l_1| \leq L$. The parity rule means there are never pairs with $l_1 = l_2$ for any odd value of $L$, while the second rule requires that only $l_1 = l_2$ pairs exist for $L = 0$. For even values of $L$ greater than zero the coupled equations will contain some partial waves with $l_1 = l_2$ and some with $l_1 \neq l_2$. For $L = 0$ the pattern in the $l_1, l_2$ matrix is particularly simple, only the "diagonal" ($l_1 = l_2$) partial waves exist. In this case, as well as for $L = 1$, there is an obvious ordering for the partial

$L = 1$

| | 0 | 1 | 2 | 3 | 4 |
|---|---|---|---|---|---|
| 0 | | 1 | | | |
| 1 | 1 | | 2 | | |
| 2 | | 2 | | 3 | |
| 3 | | | 3 | | 4 |
| 4 | | | | 4 | |

$L = 2$

| | 0 | 1 | 2 | 3 | 4 |
|---|---|---|---|---|---|
| 0 | | | 2 | | |
| 1 | | 1 | | 4 | |
| 2 | 2 | | 3 | | 6 |
| 3 | | 4 | | 5 | |
| 4 | | | 6 | | 7 |

$L = 3$

| | 0 | 1 | 2 | 3 | 4 |
|---|---|---|---|---|---|
| 0 | | | | 2 | |
| 1 | | | 1 | | 4 |
| 2 | | 1 | | 3 | |
| 3 | 2 | | 3 | | 5 |
| 4 | | 4 | | 5 | |

$L = 4$

| | 0 | 1 | 2 | 3 | 4 |
|---|---|---|---|---|---|
| 0 | | | | | 4 |
| 1 | | | | 2 | |
| 2 | | | 1 | | 5 |
| 3 | | 2 | | 3 | |
| 4 | 4 | | 5 | | 6 |

Figure 5.9: Illustration of how partial waves were chosen for $L = 1, 2, 3$ and 4. The rows and columns of each matrix correspond to the values of $l_1$ and $l_2$. Empty matrix cells indicate $(l_1, l_2)$ pairs that do not exist for that value of $L$. Non-empty cells indicate $(l_1, l_2)$ pairs that are included and the numbers in those cells give the orderining in which the pairs were chosen.

| $L=$ | 0 | 1 | 2 | 3 | 4 | 5 | 6 | 7 | 8 | 9 |
|---|---|---|---|---|---|---|---|---|---|---|
| 1 | 0,0 | 0,1 | 1,1 | 1,2 | 2,2 | 2,3 | 0,6 | 0,7 | 0,8 | 0,9 |
| 2 | 1,1 | 1,2 | 0,2 | 0,3 | 1,3 | 1,4 | 1,5 | 1,6 | 1,7 | 1,8 |
| 3 | 2,2 | 2,3 | 2,2 | 2,3 | 3,3 | 3,4 | 2,4 | 2,5 | 2,6 | 2,7 |
| 4 | 3,3 | 3,4 | 1,3 | 1,4 | 0,4 | 0,5 | 3,3 | 3,4 | 3,5 | 3,6 |
| 5 | 4,4 | 4,5 | 3,3 | 3,4 | 2,4 | 2,5 | 1,7 | 1,8 | 4,4 | 4,5 |
| 6 | 5,5 | 5,6 | 2,4 | 2,5 | 4,4 | 4,5 | 2,6 | 2,7 | 1,9 | 1,10 |
| 7 | 6,6 | 6,7 | 4,4 | 4,5 | 1,5 | 1,6 | 3,5 | 3,6 | 2,8 | 2,9 |
| 8 | 7,7 | 7,8 | 3,5 | 3,6 | 3,5 | 3,6 | 4,4 | 4,5 | 3,7 | 3,8 |
| 9 | 8,8 | 8,9 | 5,5 | 5,6 | 5,5 | 5,6 | 2,8 | 2,9 | 4,6 | 4,7 |
| 10 | 9,9 | 9,10 | 4,6 | 4,7 | 2,6 | 2,7 | 3,7 | 3,8 | 5,5 | 5,6 |
| 11 | 10,10 | 10,11 | 6,6 | 6,7 | 4,6 | 4,7 | 4,6 | 4,7 | 2,10 | 2,11 |
| 12 | 11,11 | 11,12 | 5,7 | 5,8 | 6,6 | 6,7 | 5,5 | 5,6 | 3,9 | 3,10 |
| 13 | 12,12 | 12,13 | 7,7 | 7,8 | 3,7 | 3,8 | 3,9 | 3,10 | 4,8 | 4,9 |
| 14 | 13,13 | 13,14 | 6,8 | 6,9 | 5,7 | 5,8 | 4,8 | 4,9 | 5,7 | 5,8 |
| 15 | 14,14 | 14,15 | 8,8 | 8,9 | 7,7 | 7,8 | 5,7 | 5,8 | 6,6 | 6,7 |
| 16 | 15,15 | 15,16 | 7,9 | 7,10 | 4,8 | 4,9 | 6,6 | 6,7 | 3,11 | 3,12 |

Table 5.1: The order in which partial waves were chosen for each value of $L$.

waves. Since including $(l_1, l_2)$ implicitly means also including $(l_2, l_1)$, complementary matrix cells are assigned the same number.

In deciding which $(l_1, l_2)$ partial waves to keep in the coupled equations we need to order them according to their relative importance. This can be done precisely only after actually calculating the radial functions. Relative magnitudes of several radial functions for $L = 2$ are compared in Figure 5.8. Of course, we need to choose the ordering before calculating the radial functions. The basic algorithm, which should be reasonable if enough partial waves are coupled, is to select partial waves in the order of increasing individual angular momenta. This ordering is complicated when highly asymmetric radial functions with a large $l_2$ and small $l_1$ are involved.

The orders in which the $(l_1, l_2)$ pairs were chosen for calculations at particular values of $L$ are listed in Table 5.1. In general, the pairs are ordered so that smaller angular momentum terms are included first. The ordering in Table 5.1 was computer generated by an algorithm that sometimes chooses the pairs in the order of increasing $\min(l_1, l_2)$ and sometimes in order of increasing $\max(l_1, l_2)$ and is probably not

| total angular momentum | 0 | 1 | 2 | 3 | 4 | 5 | 6 | 7 | 8 | 9 |
|---|---|---|---|---|---|---|---|---|---|---|
| number of $(l_1, l_2)$ pairs | 6 | 6 | 10 | 10 | 16 | 16 | 14 | 13 | 10 | 10 |

Table 5.2: The number of $(l_1, l_2)$ pairs that were included for each value of $L$ using the ordering in Table 5.1. Each pair with $l_1 \neq l_2$ actually adds two partial waves.

optimal. Handpicking which terms to include, or perhaps using a different algorithm, might provide a better ordering. Usually, the number of different pairs to include is chosen so that all pairs with either $l_1$ or $l_2$ below some minimum are included.

The number of partial waves that need to be kept depends upon the physical quantity being calculated. The more detailed the scattering information, the more partial waves that must be included to converge the results. In the next chapter we will extract differential cross sections for ionization from the radial functions calculated here. It was found that generating radial functions up through $L = 9$ was sufficient. The numbers of partial waves (with $l_1 \leq l_2$) that needed to be included for each $L$ in order to converge the most detailed cross sections are listed in Table 5.2.

# Chapter 6

# Differential Cross Sections for Electron-Impact Ionization

A complete theoretical treatment of electron-impact ionization means obtaining differential cross sections that give detailed information about the two outgoing electrons. The triple differential cross section gives angular distributions for both electrons and describes how energy is shared between them. Results presented in this chapter represent the first calculated triple differential cross sections that agree, on an absolute scale, with experiment [29]. The single differential cross section provides information only about how energy is shared between the two electrons. Both types of differential cross sections are obtained from the outgoing flux of the scattered wave. Since the wave function is known only on a finite region, an extrapolation procedure is used to calculate the asymptotic limit of the flux.

## 6.1 Scattered Flux

Differential cross sections for electron-impact ionization of hydrogen can be calculated from the scattered flux by a straightforward extension of the procedure developed for the Temkin-Poet model problem. The same characteristics and limitations encountered in Chapter 4 will apply here. In addition, there are further complications due to the directional dependence of the flux.

### 6.1.1 Flux at finite distances

The total cross section is related to the integral of the probability current density $\mathrm{j}_{\rho_0}$ through a hypersphere of radius $\rho_0$ in the limit $\rho_0 \to \infty$. For electron-hydrogen scattering, $\mathrm{j}_{\rho_0}$ is a function of the scattering directions $\hat{r}_1$ and $\hat{r}_2$ for both electrons as well as the hyperspherical angle $\alpha$.

$$\mathrm{j}_{\rho_0}(\alpha, \hat{r}_1, \hat{r}_2) \equiv \hat{\rho} \cdot \mathrm{Im}\left\{ \left(\Psi^+_{\mathrm{sc}}(\vec{r}_1, \vec{r}_2)\right)^\star \vec{\nabla} \Psi^+_{\mathrm{sc}}(\vec{r}_1, \vec{r}_2) \right\} \Big|_{\rho=\rho_0} \tag{6.1}$$

Equation 4.5 gives the total cross section in terms of an integral over the probability current density in the Temkin-Poet model. A similar expression gives the total cross

section for electron-hydrogen scattering.

$$\sigma_{\text{total}} = \frac{1}{k_i} \int_0^{\pi/2} \int_{4\pi} \int_{4\pi} \mathsf{j}_{\rho_0}(\alpha, \hat{r}_1, \hat{r}_2)\, r_1^2 r_2^2 d\hat{r}_1 d\hat{r}_2 \rho_0 d\alpha \Bigg|_{\rho_0 \to \infty} \tag{6.2}$$

Equation 6.2 differs from Equation 4.5 in that it is an integral over the hyperangle and both directions. Also, the normalization factor is different because the initial state $\Psi^0_{k_i}$, defined in Equation 2.5, is normalized differently from the one used for the Temkin-Poet model. In Equation 2.5 the incident electron is represented by $e^{ik_i z}$ so the incident flux density consistent with Equation 6.1 is simply $k_i$.

We will work with a generalized, dimensionless flux $\mathsf{f}_{\rho_0}(\alpha, \hat{r}_1, \hat{r}_2)$ that includes a factor of $k_i$ and the Jacobian factor $r_1^2 r_2^2 \rho$ from the volume element in Equation 6.2.

$$\mathsf{f}_{\rho_0}(\alpha, \hat{r}_1, \hat{r}_2) \equiv \text{Im}\left\{ k_i \rho \left( r_1 r_2 \Psi^+_{\text{sc}}(\vec{r}_1, \vec{r}_2) \right)^\star \frac{d}{d\rho} \left( r_1 r_2 \Psi^+_{\text{sc}}(\vec{r}_1, \vec{r}_2) \right) \right\} \Bigg|_{\rho=\rho_0} \tag{6.3}$$

Total scattered flux is related to $\mathsf{f}_{\rho_0}$ in the limit $\rho_0 \to \infty$ by integration over the hyperspherical angle and both directions.

$$\sigma_{\text{total}} = \frac{1}{k_i^2} \int_0^{\pi/2} \int_{4\pi} \int_{4\pi} \mathsf{f}_{\rho_0}(\alpha, \hat{r}_1, \hat{r}_2)\, d\hat{r}_1 d\hat{r}_2 d\alpha \Bigg|_{\rho_0 \to \infty} \tag{6.4}$$

Just as in the two-dimensional model problem, the flux is directly related to differential cross sections for ionization, except in the cases where one of the electrons carries nearly all of the energy (see Section 4.4).

Equation 6.4 shows that, in the limit $\rho_0 \to \infty$, $\mathsf{f}_{\rho_0}(\alpha, \hat{r}_1, \hat{r}_2)$ gives the distribution of the scattering probability over the directions $\hat{r}_1$ and $\hat{r}_2$ and the hyperangle $\alpha$. We will need the asymptotic limit of the flux to calculate differential cross sections for ionization. With exterior complex scaling we know the wave function only on a finite region so we can directly calculate $\mathsf{f}_{\rho_0}$ only for finite $\rho_0$. That means we will need to employ an extrapolation procedure similar to the one used in Chapter 4 to obtain the $\rho_0 \to \infty$ limit. Unlike in Chapter 4, the scattered wave is a function of the hyperradius and five angles and it must be constructed from as many of the partial wave terms from Equation 5.3 as necessary to converge the final results.

$$\mathsf{f}_{\rho_0}(\alpha, \hat{r}_1, \hat{r}_2) = \text{Im}\left\{ k_i \rho \sum_{L', l_1, l_2'} \sum_{L, l_1, l_2} \left( \psi^{L'}_{l_1' l_2'} \right)^\star \frac{d}{d\rho} \left( \psi^{L}_{l_1 l_2} \right) \left( \mathcal{Y}^{L'0}_{l_1', l_2'} \right)^\star \mathcal{Y}^{L0}_{l_1, l_2} \right\} \Bigg|_{\rho=\rho_0} \tag{6.5}$$

### 6.1.2 Coplanar geometry

The flux is a function of five variables: the hyperangle $\alpha$ and the four spherical polar angles $\theta_1$, $\phi_1$, $\theta_2$, and $\phi_2$. In examining properties of the calculated flux we will restrict the two final directions so that they and the incident direction all lie within a plane. This "coplanar" geometry is illustrated in Figure 6.1. All available

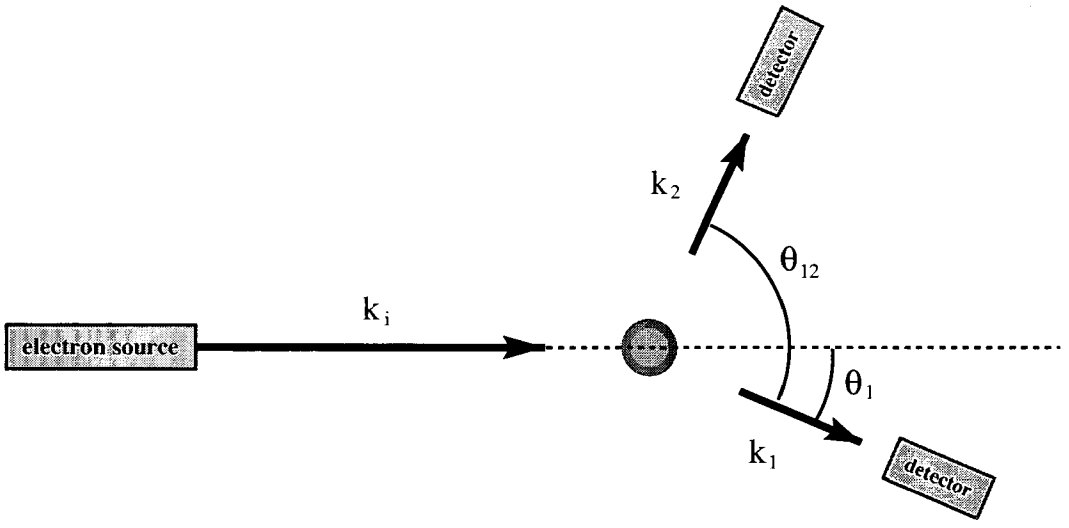


Figure 6.1: Diagram of coplanar geometry. Two electron detectors and the incident electron beam all lie within a plane.

experimental data is for these types of geometries. In an experiment, the two electron detectors and the incident electron beam all lie in a single plane. The angle between one of the detectors and the incident beam is denoted by $\theta_1$ and the angle between the two detectors by $\theta_{12}$.

### 6.1.3 Adding partial waves

Computing the flux requires constructing the complete scattered wave from its partial wave terms as shown in Equation 6.5. That means we need to be concerned about the convergence of the calculated flux with respect to the number of partial waves kept in the expansion of $\Psi^+_{sc}$. This is an issue at two levels: the number of $(l_1, l_2)$ pairs kept for each total angular momentum $L$ and the maximum value of $L$ kept in the expansion. The minimum number of $(l_1, l_2)$ pairs kept for each particular $L$ is shown in Table 5.2. These numbers were chosen mainly by determining at what point adding more partial waves to a pre-existing solution to the coupled equations stopped affecting the previously computed radial functions.

Examples of the flux at $\rho_0 = 120a_0$, shown in Figure 6.2, illustrate the effect that including partial waves with increasingly large values of $L$ in the expansion of $\Psi^+_{sc}$ has on the calculated flux. Flux in Figure 6.2 were calculated for a hyperangle of $45^o$ with the two scattering directions chosen so that the incident direction always bisects the angle between them. The solid line in the upper part of each panel is the flux constructed by keeping partial waves only up to the particular value of $L < 9$ indicated. The dashed line in every panel is the flux calculated when keeping partial waves up to $L = 9$.

Comparing flux calculated using different numbers of partial waves is a good method for measuring the convergence of the flux with respect to adding more partial waves. For each panel the relative difference between the solid and dashed lines in

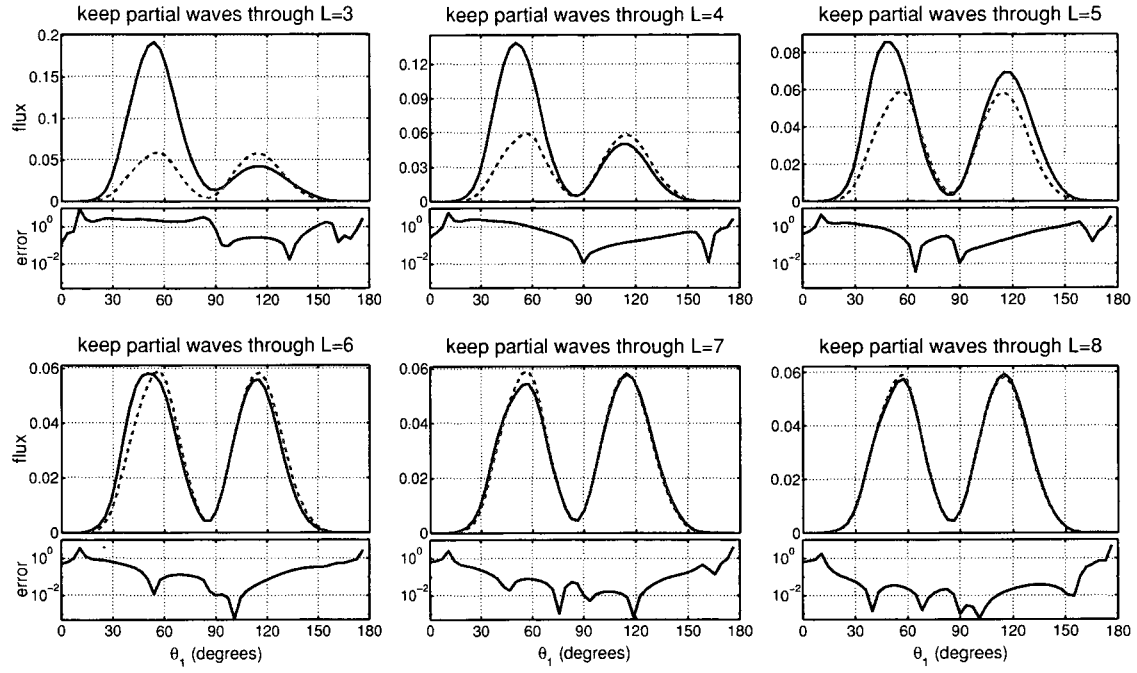


Figure 6.2: Convergence of flux when including partial waves up to increasingly large $L$. Flux at $\rho_0 = 120a_0$ is shown for coplanar geometries with $\theta_2 = -\theta_1$. The dashed line in each panel shows the flux when partial waves up to $L = 9$ are included.

the upper part is plotted on a log scale in the lower part. This gives an indication of the error due to prematurely truncating the expansion in $L$. Convergence in $L$ is very slow when the scattering directions are close together and much more rapid when the electrons are moving directly apart from each other.

## 6.2 Differential Cross Sections for Ionization

The cross section definition in Equation 6.4 requires the $\rho_0 \to \infty$ limit of $\mathsf{f}_{\rho_0}$. Since the wave function calculated under exterior complex scaling is equivalent to the unscaled wave function only on a finite region we can calculate $\mathsf{f}_{\rho_0}$ only for finite $\rho_0$. Thus, in order to obtain differential cross sections for ionization from flux calculations we must use an extrapolation in $\rho_0$ similar to the procedure described in Chapter 4 for calculating single differential cross sections in the Temkin-Poet model.

### 6.2.1 Extrapolating ionization flux

According to the asymptotic form for ionization in Equation 2.11, the ionization flux is expected to approach its asymptotic limit like $\frac{1}{\rho_0}$.

$$\text{large } \rho_0: \qquad \mathsf{f}_\rho(\alpha, \hat{r}_1, \hat{r}_2) \simeq \mathsf{f}_\infty(\alpha, \hat{r}_1, \hat{r}_2) + \mathcal{O}\left(\frac{1}{\rho_0}\right) \tag{6.6}$$

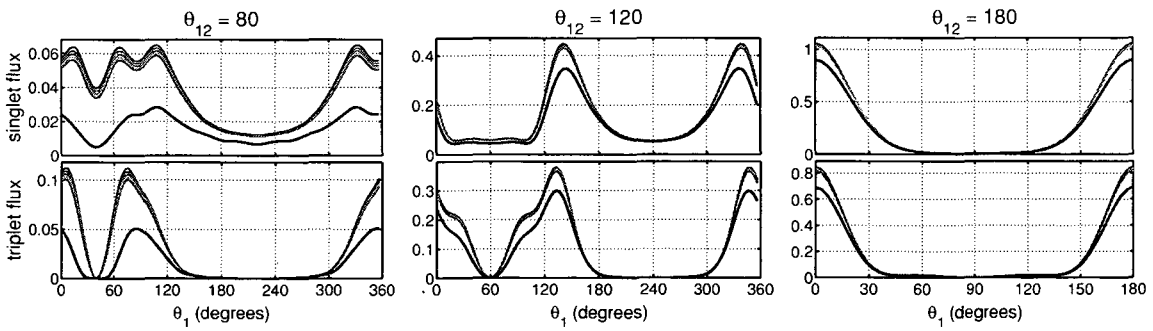


Figure 6.3: Extrapolation in $\rho$ of ionization flux for coplanar geometries with fixed $\theta_{12}$ at 20 eV incident energy. In each panel flux calculated at $\rho = 100, 105, 110, 115$ and $120a_0$ are shown along with the extrapolated flux. The line for the extrapolated flux always lies below the others.

Fitting Equation 6.6 to several $\mathsf{f}_{\rho_0}$ calculated directly from the wave function gives the $\rho_0 \to \infty$ limit of the flux provided that the calculated $\mathsf{f}_{\rho_0}$ are in the region where the flux behaves according to Equation 6.6.

The flux can, of course, be calculated only in the region where both coordinates are not complex-scaled *i.e.*, for $r_1, r_2 < R_0$. That restricts the $\mathsf{f}_{\rho_0}$ used for the extrapolation to those for which $\rho_0 \leq R_0$ if the $\mathsf{f}_{\rho_0}$ are needed over the full range of the hyperangle $\alpha$. However, if the cross section is only needed for values of $\alpha$ near $45^o$ then we can also calculate $\mathsf{f}_{\rho_0}$ for hyperradii in the range $R_0 < \rho_0 < \sqrt{2}R_0$. In Chapter 4 we found that the quality of the extrapolated results depended on the hyperangle $\alpha$ because of contamination from bound states. With a flux that is also a function of the two directions we can expect that the extrapolation behavior will depend upon the four angular coordinates as well.

Three examples of calculated and extrapolated flux for both singlet and triplet spin symmetries with $\alpha = 45^o$, where contamination from bound states has the least effect, are shown in Figure 6.3. These examples are restricted to coplanar geometries (see Figure 6.1) with a fixed angle $\theta_{12}$ between the two scattering directions. In all cases, the line for the extrapolated flux lies below the lines for the flux calculated at finite $\rho_0$. Relative differences between the calculated and extrapolated flux are largest when the angle between the two directions is smallest. This is sensible because a particular hyperradius $\rho_0$ corresponds to a distance of $2\rho_0$ between the two electrons when they are moving directly away from each other whereas the actual distance between the two electrons is smaller when the angle between their directions is less than $180^o$.

A general property of the flux shown in Figure 6.3 is that there are always local minima at $\theta_1 = \frac{1}{2}\theta_{12}$ and $\theta_1 = \frac{1}{2}\theta_{12} + 180^o$. Both of these correspond to cases where the incident direction bisects the angle between the two detectors. In fact, in these cases the Pauli exclusion principle requires that the triplet contribution be identically zero because of the cylindrical symmetry of the system.

### 6.2.2 Triple differential cross section

For large $\rho$ the hyperangle $\alpha$ parametrizes energy sharing between the two electrons as $\varepsilon_1 = E\cos^2\alpha$ and $\varepsilon_2 = E\sin^2\alpha$. It is simple to convert a quantity that is differential in $\alpha$ to one that is differential in the energy of one electron.

$$\left.\frac{d\sigma_{\rm ion}(\varepsilon,\hat{r}_1,\hat{r}_2)}{d\varepsilon d\hat{r}_1 d\hat{r}_2}\right|_{\varepsilon=E\sin^2\alpha} \simeq \lim_{\rho_0\to\infty} \frac{1}{k_i^2 E\sin\alpha\cos\alpha}\,\mathsf{f}_{\rho_0}(\alpha,\hat{r}_1,\hat{r}_2) \tag{6.7}$$

For ionization, the most detailed quantity of interest is the so-called triple differential cross section (TDCS) defined in Equation 6.7. It gives the distribution of the ionization cross section over energy sharing between the two electrons and the two directions $\hat{r}_1$ and $\hat{r}_2$.

The conditional equality in Equation 6.7 was discussed in Chapter 4. We are interested in only the flux due to ionization, but we are calculating flux from the full scattered wave that contains discrete channel components as well as ionization. Thus, the region of validity for the TDCS obtained by extrapolation is limited to the range of $\varepsilon$ (or $\alpha$) where the directly calculated flux $\mathsf{f}_{\rho_0}$ were composed only of ionization. This means that we cannot calculate the TDCS for single-electron energies smaller than 20%, or so, of the total energy.

By convention, the TDCS is normalized so that the total ionization cross section is related to it by integration over the one-electron energy $\varepsilon$ from zero to $E/2$ and integration over the full range of both directions $\hat{r}_1$ and $\hat{r}_2$.

$$\sigma_{\rm ion} = \int_0^{E/2}\int_{4\pi}\int_{4\pi} \frac{d\sigma_{\rm ion}(\varepsilon,\hat{r}_1,\hat{r}_2)}{d\varepsilon d\hat{r}_1 d\hat{r}_2}\, d\hat{r}_1 d\hat{r}_2 d\varepsilon \tag{6.8}$$

Any energy sharing cross-section must be symmetric about $E/2$ because of the impossibility of distinguishing which electron has energy $\varepsilon_1$ and which has energy $\varepsilon_2 = E - \varepsilon_1$. Since the differential cross section is defined for only half the energy range there is a factor of two included in Equation 6.7.

## 6.3 Comparison With Experiment

Measuring the TDCS requires two electron detectors. One is tuned to detect electrons of some energy $\varepsilon_1$ and the other is tuned to detect electrons of energy $\varepsilon_2 = E - \varepsilon_1$. Although the basic experimental apparatus is simple to envisage, accurate and detailed measurements are apparently quite difficult and, unfortunately, there is very little absolute experimental data available.

The best collection of TDCS data for electron-impact ionization of hydrogen at low energies comes from "symmetric, coplanar" measurements performed by Röder *et al.* and published in 1996 [33]. For these measurements both detectors were tuned to detect electrons with energy $E/2$ and arranged in the coplanar geometry depicted in Figure 6.1. In this geometry the electron source, the two detectors, and the interaction region all lie on the same plane. For most of the comparisons presented here the angle

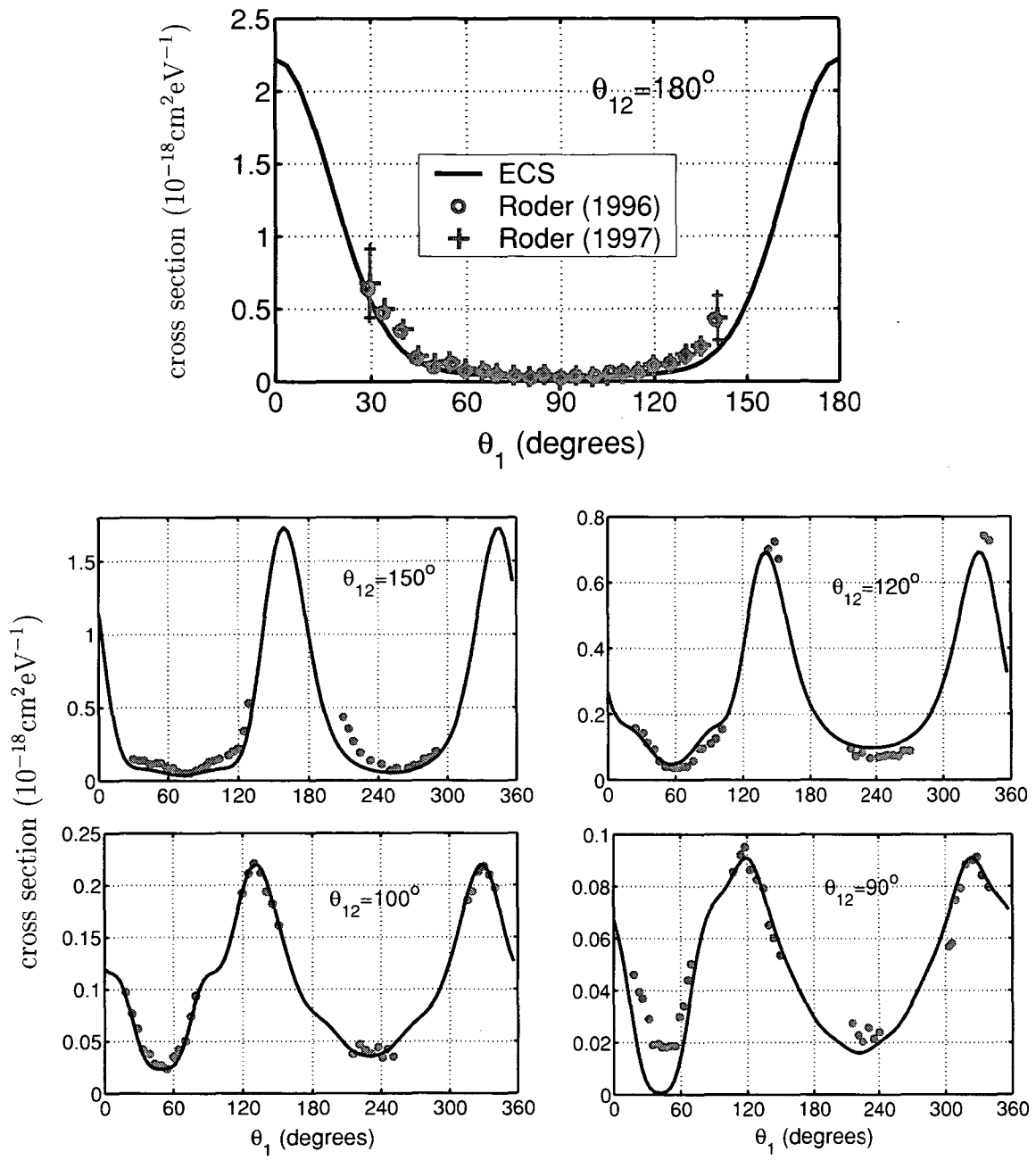


Figure 6.4: Symmetric coplanar TDCS for 17.6 eV incident energy with $\theta_{12}$ fixed. 1996 data [33] normalized by comparison with 1997 data [32] for $\theta_{12} = 180^o$. Normalization factor = 0.23.

$\theta_{12}$ between the two detectors is held fixed while the angles between the detectors and the incident direction are varied. Unfortunately, this data was originally presented in unknown units and must be multiplied by an overall scaling factor to compare with calculated cross sections. This scaling factor is dependent on energy, but supposedly not on the geometry, and is expected to be the same for all data sets of different geometries but the same energy.

### 6.3.1 TDCS for 17.6 eV

Röder *et al.* presented a small set of measurements in 1997 [32] that attempted to put the previously measured TDCS data on an absolute scale. They gave experimentally normalized data for incident energies of 15.6 eV and 17.6 eV, but only for the case where $\theta_{12} = 180^o$. We have calculated wave functions for 17.6 eV incident energy so we can compare with absolute experimental data at this one energy [29]. We normalized the set of 17.6 eV measurements by comparing the $\theta_{12} = 180^o$ data from 1996 to the corresponding data from 1997 and choosing a normalization factor that scales the 1996 data to coincide with the 1997 data.

Absolute data from 1997 and normalized 1996 data with $\theta_{12} = 180^o$ are shown together, along with the TDCS calculated with exterior complex scaling, in the top panel of Figure 6.4. The cross section in this case is strongly peaked at angles of $0^o$ and $180^o$, where one electron is scattered forward and the other "recoils" in the backward direction. Unfortunately, experimental measurements were not possible near these points. A normalization factor of 0.23 scales the 1996 data to coincide with the 1997 data in units of $10^{-18}\text{cm}^2\text{eV}^{-1}$.

The remaining four panels in Figure 6.5 show the calculated TDCS at different $\theta_{12}$ compared with 1996 data using the same normalization factor. Agreement between the calculated TDCS and experimental data is excellent, particularly for $\theta_{12}$ of $120^o$, $100^o$, and $90^o$ where measured values exist for the cross section peaks. The largest discrepancy is at the minimum for $\theta_{12} = 90^o$. Since this is the smallest value of all the data sets we expect the measurement to be less accurate there. Also, converging

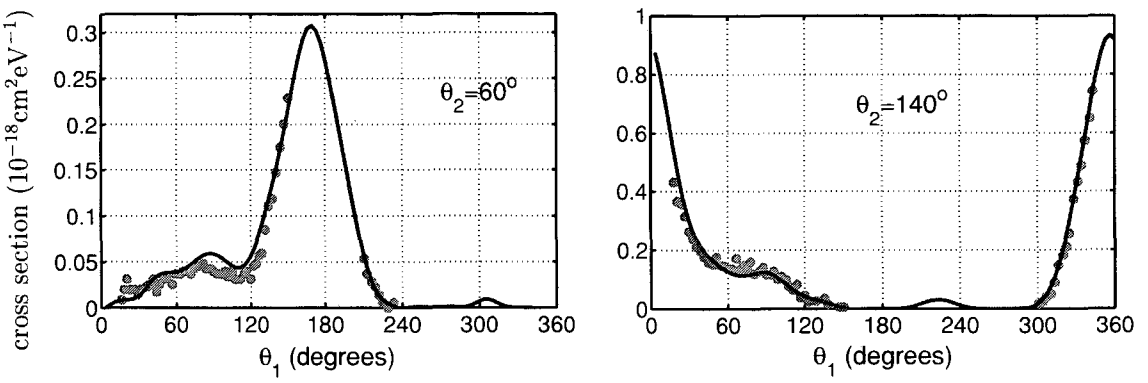


Figure 6.5: Symmetric coplanar TDCS for 17.6 eV incident energy with $\theta_2$ fixed. Measurements [33] scaled to fit calculated cross section. Normalization factor = 1.15.

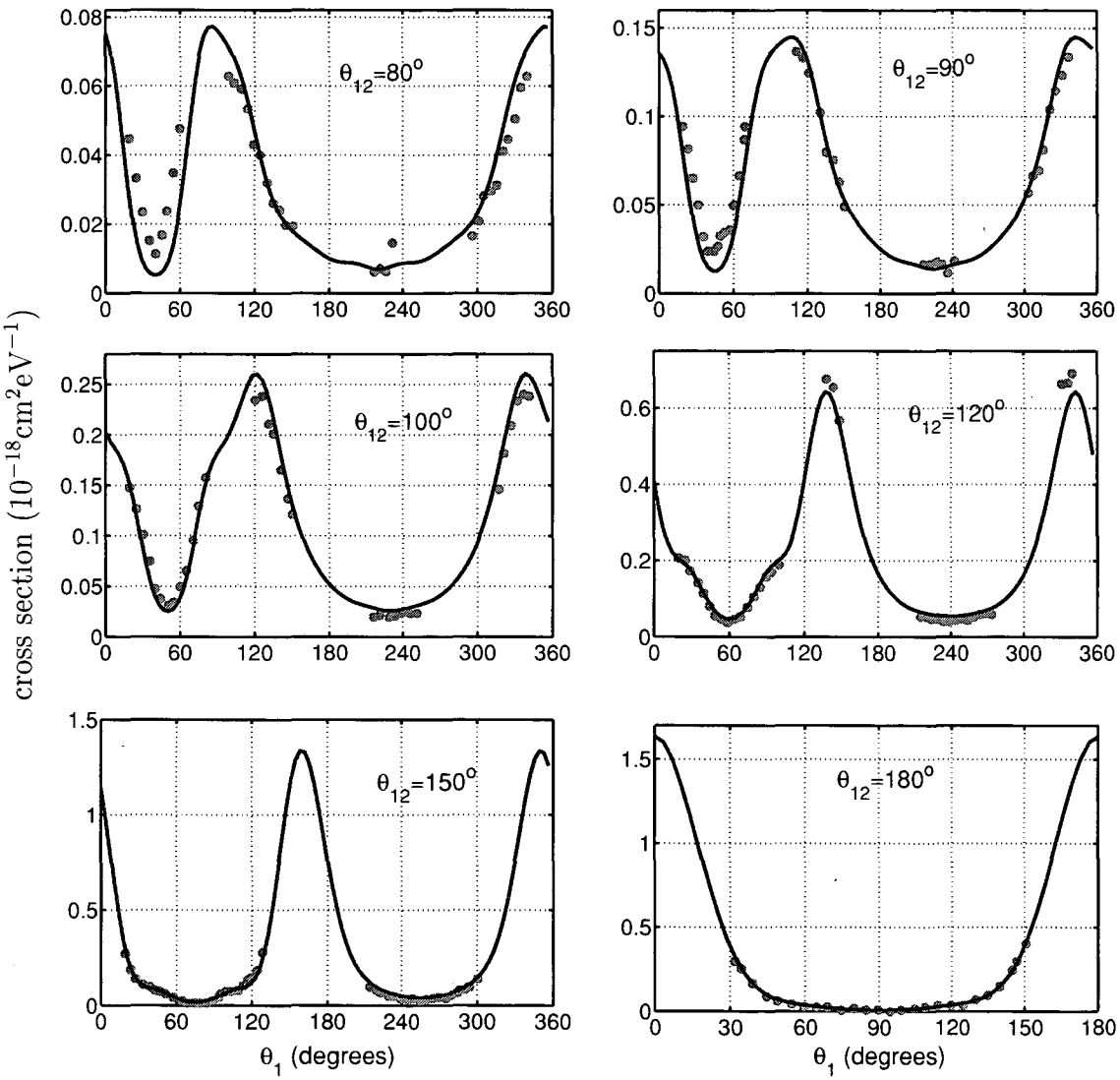


Figure 6.6: Symmetric coplanar TDCS for 20 eV incident energy with $\theta_{12}$ fixed. Measurements [33] scaled to fit calculated cross section. Normalization factor = 0.20.

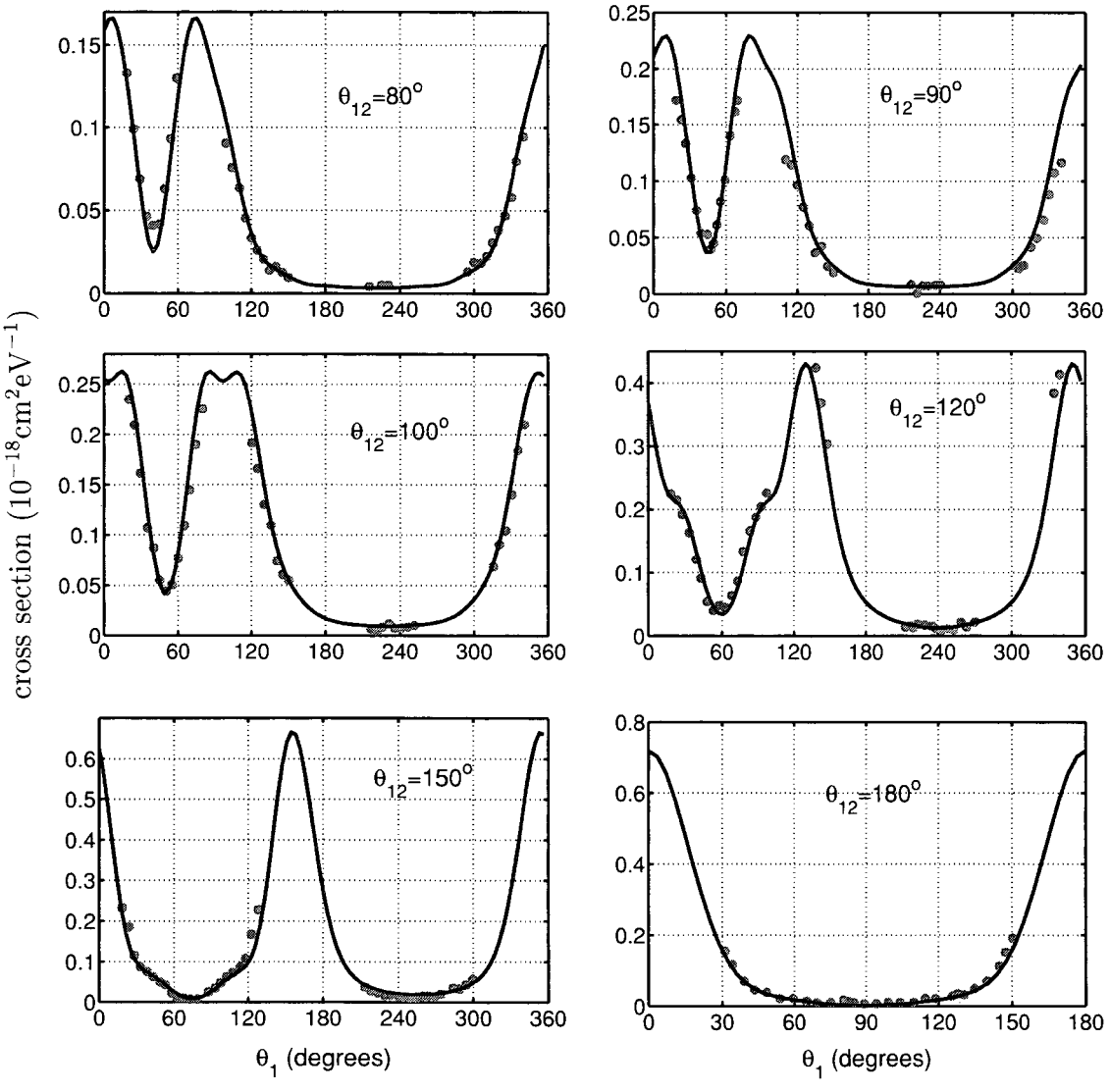


Figure 6.7: Symmetric coplanar TDCS for 25 eV incident energy with $\theta_{12}$ fixed. Measurements [33] scaled to fit calculated cross section. Normalization factor = 0.16

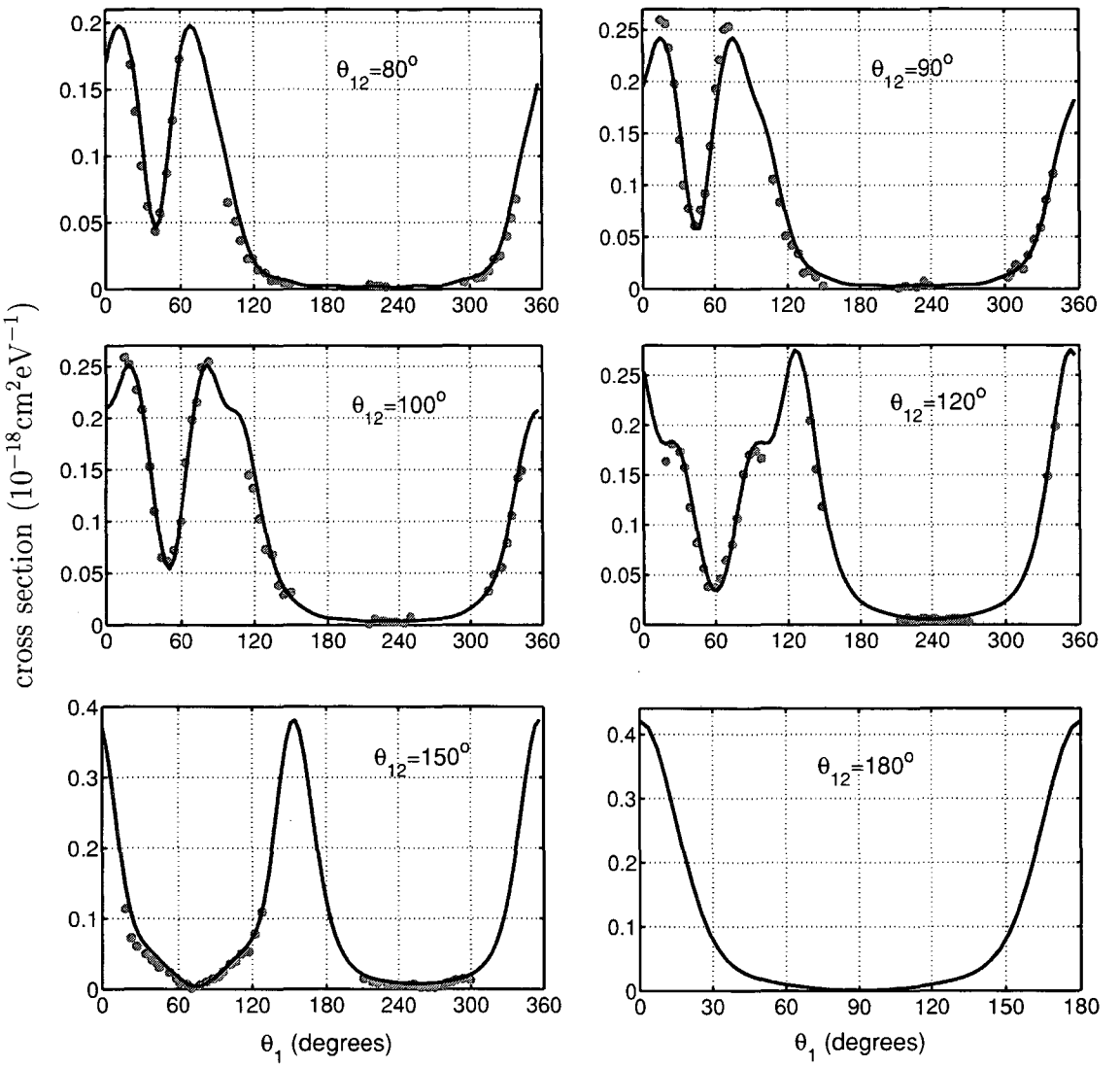


Figure 6.8: Symmetric coplanar TDCS for 30 eV incident energy with $\theta_{12}$ fixed. Measurements [33] scaled to fit calculated cross section. Normalization factor = 0.16

calculated TDCS in terms of partial waves was more difficult for $\theta_{12} = 90$ than for the other geometries.

Additionally, there are two sets of 1996 measurements at 17.6 eV where the position of one detector was held fixed while the other was rotated independently. This data is normalized differently than the fixed $\theta_{12}$ measurements. A single normalization factor for these two sets of data was chosen to give the best fit to the calculated cross section. Normalized experimental data and the calculated TDCS for these two cases are shown in Figure 6.5.

### 6.3.2 TDCS for 20, 25, and 30 eV

Comparisons between the calculated TDCS and measured values for incident energies of 20, 25, and 30 eV are shown in Figures 6.6, 6.7 and 6.8. Experimental values were presented by Röder *et al.* [33]. As with the 17.6 eV measurements, the data is presented in arbitrary units and must be normalized. However, for these energies there are no absolute measurements available with which to normalize the data. Therefore, we normalized the experimental values by choosing a scaling factor for each energy that best fits the experimental data to the calculated cross section.

With these results, experimental data at these energies has been put, for the first time, on an absolute scale. It is important to emphasize that a *single* scaling factor was used for all data at a particular energy. Overall, the agreement between the present calculations and measured values is excellent. The largest discrepancy is for $\theta_{12} = 80^o$ at 20 eV incident energy. We should expect larger disagreement for the smallest value of $\theta_{12}$ because converging the calculated cross section in terms of partial waves is more difficult when the two scattering directions are closer together.

## 6.4 Single Differential Cross Sections

The single differential cross section (SDCS) gives only the energy distribution between the two electrons and is related to the TDCS by integration over the two scattering directions $\hat{r}_1$ and $\hat{r}_2$.

$$\frac{d\sigma_{\rm ion}(\varepsilon)}{d\varepsilon} = \int_{4\pi}\int_{4\pi} \frac{d\sigma_{\rm ion}(\varepsilon, \hat{r}_1, \hat{r}_2)}{d\varepsilon d\hat{r}_1 d\hat{r}_2}\, d\hat{r}_1 d\hat{r}_2 \tag{6.9}$$

Constructing the TDCS from a partial wave expansion requires a double sum over all angular momentum quantum numbers as in Equation 6.5. Because of the orthonormality of the spherical harmonics, $\mathcal{Y}^{L0}_{l_1,l_2}(\hat{r}_1, \hat{r}_2)$, integration over $\hat{r}_1$ and $\hat{r}_2$ collapses this into a single sum over each angular momentum quantum number.

Consequently, the SDCS is a simple sum of partial wave terms for each set of $L, l_1, l_2$ quantum numbers. Each individual term is calculated from a single partial

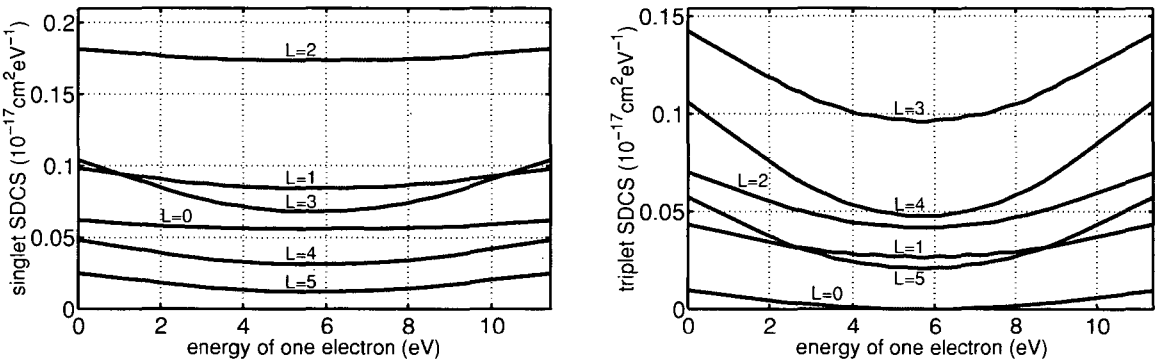


Figure 6.9: Components of the SDCS (with spin factors included) for electron-hydrogen scattering at 25 eV incident energy corresponding to particular total spin and angular momentum quantum numbers.

wave component of the scattered wave.

$$\left.\frac{d\sigma_{\rm ion}(\varepsilon)}{d\varepsilon}\right|_{\varepsilon=E\sin^2\alpha} \simeq \frac{\rho}{k_i E \sin\alpha\cos\alpha} \sum_{L,l_1,l_2} \mathrm{Im}\left\{\left(\psi^L_{l_1 l_2}(r_1,r_2)\right)^\star \frac{d}{d\rho}\left(\psi^L_{l_1 l_2}(r_1,r_2)\right)\right\}\Bigg|_{\rho\to\infty} \tag{6.10}$$

Calculating each term in Equation 6.10 is equivalent to calculating the SDCS in the Temkin-Poet model. So, calculating the SDCS for electron-impact ionization of hydrogen is a trivial extension of the procedure described in Chapter 4.

In general, significantly fewer partial wave terms are needed to converge the SDCS than are needed to converge the TDCS. For the incident energies treated here there is never a need to include contributions for $L > 6$. Also, the number of partial waves needed for any particular $L$ component is generally smaller than the number needed to converge the TDCS. Individual total angular momentum components of the SDCS at 25 eV incident energy are shown in Figure 6.9 for both singlet and triplet spin symmetries. For the singlet case the $L = 2$ component is the most important with the relative importance of each component decreasing with increasing $L$ for $L > 2$. For the triplet case it is the $L = 3$ component that is most important. The $L = 0$ radial functions must all have the same symmetry properties as in the Temkin-Poet model. That means the $L = 0$ component of the triplet SDCS is insignificant because those radial functions must vanish in the middle of the ionization region.

### 6.4.1 Contamination from bound states

At finite $\rho_0$ the discrete channel components of $\Psi^+_{\rm sc}$ extend over a nonzero range of the hyperangle $\alpha$. The discrete channel components of the flux do not behave like Equation 6.6 so the extrapolated flux is not valid over the full range of $\alpha$. For the Temkin-Poet model we found that the asymptotic flux extrapolated from $\rho_0$ near $100a_0$ was valid for $\alpha$ between $15^o$ and $75^o$. We expect the same qualitative behavior here. The range of $\alpha$ over which we may extrapolate the ionization flux is limited

according to which discrete channel components have non-negligible magnitudes. This will be slightly different for each partial wave as can be seen in Figure 5.8.

For the most significant partial waves the discrete channels are still confined within $15^o$ of the edges. Partial waves with larger angular momenta have longer-range discrete channels that are visible. In the cases with the largest angular momenta it is really not even possible to distinguish between ionization and higher excitations. However, the partial waves for which the discrete channels obscure a larger portion of the ionization wave are less significant so we can still assume that the sum of the extrapolated flux for all partial waves is reasonable over the same range of $\alpha$ as was found in the Temkin-Poet model.

We estimate the SDCS over the full range of $\varepsilon$ by using the same extrapolation in energy introduced in Chapter 4 for the Temkin-Poet model. We assume that the SDCS behaves linearly near the edges and replace the calculated values in a small region near $\varepsilon = 0$ (and $\varepsilon = E$) with a linear extrapolation. There is some ambiguity about whether this should be done to each partial wave term individually or whether it should be applied to the sum, but in practice this makes little difference. For the results presented here the extrapolation in energy was applied to $L$-components of the singlet and triplet SDCS. These were formed by adding together all partial wave terms from Equation 6.10 with the same values of $L$ and $S$. End-regions of the $L$-components were then replaced by linear extrapolations in energy, producing SDCS components such as those shown in Figure 6.9.

### 6.4.2 SDCS for 17.6, 20, 25, and 30 eV

Results for the calculated SDCS at all four energies treated here are shown in Figures 6.10 and 6.11. In each case, the singlet and triplet components of the SDCS are shown along with the total SDCS. Spin factors are included in the spin components so the total SDCS is simply the sum of the singlet and triplet SDCS. All of the curves are very smooth and symmetric about $E/2$. Unlike in the Temkin-Poet model, the triplet SDCS is not zero in the middle. The only experimentally determined values

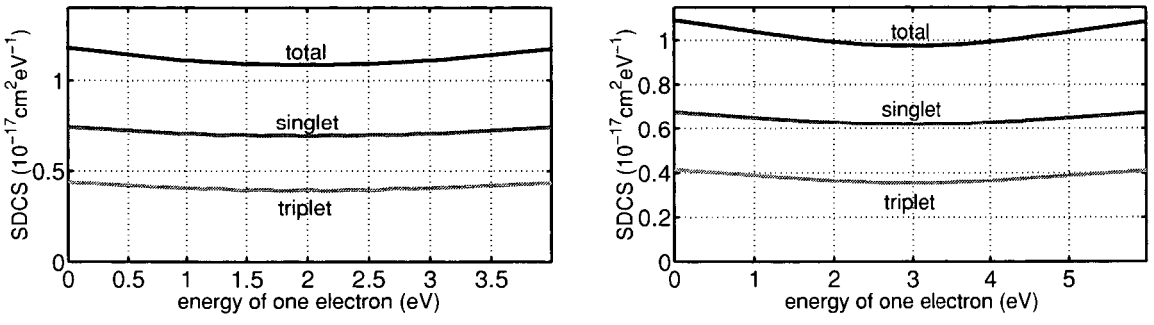


Figure 6.10: Single differential cross sections for electron-hydrogen scattering at 17.6 eV (left) and 20 eV (right) incident energies. The cross sections for singlet and triplet spin symmetries (with spin factors included) are shown along with the total.

| | 17.6 eV | | 20 eV | | 25 eV | | 30 eV | |
|---|---|---|---|---|---|---|---|---|
| $\varepsilon/E$ | $S=0$ | $S=1$ | $S=0$ | $S=1$ | $S=0$ | $S=1$ | $S=0$ | $S=1$ |
| 0.0 | 2.97 | 0.58 | 2.70 | 0.55 | 2.15 | 0.63 | 1.68 | 0.61 |
| 0.1 | 2.90 | 0.57 | 2.64 | 0.53 | 2.02 | 0.54 | 1.53 | 0.49 |
| 0.2 | 2.84 | 0.55 | 2.58 | 0.51 | 1.88 | 0.45 | 1.39 | 0.37 |
| 0.3 | 2.80 | 0.54 | 2.53 | 0.49 | 1.79 | 0.38 | 1.31 | 0.29 |
| 0.4 | 2.78 | 0.53 | 2.49 | 0.48 | 1.74 | 0.34 | 1.25 | 0.24 |
| 0.5 | 2.77 | 0.53 | 2.48 | 0.47 | 1.72 | 0.33 | 1.24 | 0.23 |

Table 6.1: Numerical values for the singlet and triplet components of the SDCS, spin factors are not included, in units of $10^{-17}\text{cm}^2\text{eV}^{-1}$. Values are given at different one-electron energies $\varepsilon$ for incident energies of 17.6, 20, 25, and 30 eV. Total energy $E$ is equal to the incident energy minus 13.6 eV.

for the SDCS are those obtained by Shyn [35] at 25 eV incident energy. They are compared with the calculated SDCS in Figure 6.11. These values were determined by integrating measurements of the double differential cross section that depends upon the polar angle as well as the energy of one electron. Numerical values for the SDCS at all four energies are listed in Table 6.1 for six different ratios of the one-electron energy to the total energy.

## 6.5 Integral Ionization Cross Sections

As a final means of measuring the ionization component present in the wave functions calculated using exterior complex scaling, we will consider spin asymmetries and integral cross sections for ionization. The integral ionization cross section $\sigma_{\text{ion}}$ is obtained by integrating the SDCS. Spin asymmetry is a measure of the relative contributions of the singlet and triplet spin components to $\sigma_{\text{ion}}$. Both are given in terms of the individual ionization cross sections for singlet, $\sigma_S$, and triplet, $\sigma_T$, spin

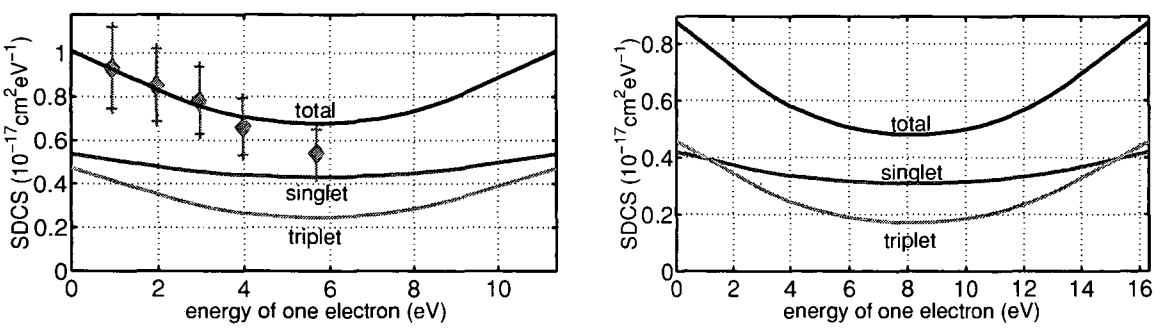


Figure 6.11: Same as Figure 6.10, but for 25 eV (left) and 30 eV (right) incident energies. Experimentally determined values due to Shyn [35] are shown for 25 eV incident energy.

| incident energy | 17.6 eV | 20 eV | 25 eV | 30 eV |
|---|---|---|---|---|
| singlet | 2.027 | 2.741 | 3.807 | 4.036 |
| triplet | 0.389 | 0.538 | 0.885 | 1.047 |
| total | 0.798 | 1.089 | 1.616 | 1.794 |
| asymmetry | 0.513 | 0.506 | 0.452 | 0.416 |

Table 6.2: Singlet, triplet and total ionization cross sections and the spin asymmetry. Cross sections are in units of $a_0^2$, asymmetry is dimensionless. Spin factors are not included in the singlet and triplet cross sections.

symmetries that are defined without including spin statistical factors.

$$\sigma_{\text{ion}} = \frac{1}{4}\left(\sigma_S + 3\sigma_T\right) \qquad \text{Spin Asymmetry} \equiv \frac{\sigma_S - \sigma_T}{\sigma_S + 3\sigma_T} \tag{6.11}$$

Values for $\sigma_S$, $\sigma_T$, $\sigma_{\text{ion}}$, and the spin asymmetry are listed in Table 6.2. The comparisons between measured and calculated TDCS earlier in this chapter indicate that exterior complex scaling is successful in correctly describing the details of at least part of the ionization final state. The values in Table 6.2 provide the coarsest measure of the ionization final state and may be useful for future comparisons with experiment or other theoretical methods.

# Chapter 7

# The Quest for a General Solution to Electron-Impact Ionization

## 7.1 Significance of this work

Electron-impact ionization is the aspect of electron-hydrogen collisions most difficult to treat theoretically and has stood as the last unsolved problem in the quantum mechanics of two-electron systems. With the work reported here, a complete solution to electron-hydrogen scattering above the ionization threshold has finally been realized nearly thirty years after the first meaningful calculations were performed on the system. Triple differential cross sections for electron-impact ionization are now known, for the first time, on an absolute scale. These detailed cross sections can be calculated for a range of geometries and energy sharing ratios where no experimental data is available and that is currently inaccessible to other theoretical methods.

The real impact of this work is that it signifies the first solution to a particular class of fundamental problems in atomic physics. Never before has a detailed description of a quantum mechanical system of three charged particles moving apart been possible. These results enable an understanding of the details of three-body breakup processes that will carry forward to systems more complicated than electron-hydrogen scattering. Combined with the existing formal theory of ionization, they provide a solid basis for thoroughly understanding the dynamics of three-body breakup.

Also, this dissertation provides the first demonstration of exterior complex scaling as a viable approach to electron collision theory. Currently, ECS stands alone in its ability to produce wave functions describing two electrons in the continuum. The spectacular agreement between experimental values and calculated cross sections validates the correctness of these wave functions. This is strong evidence in support of the claim that exterior complex scaling can represent any final scattering state, no matter how complicated the boundary conditions. Unlike other methods proposed to study ionization, this method involves no uncontrolled approximations. Accuracy of the results is limited only by the finite size of the grid used and the number of terms retained in the partial wave expansion.

The wave functions presented in Chapter 5 are the first verified to correctly de-

scribe scattering with two electrons in the continuum. They stand as a benchmark with which to test new methods designed to study breakup in more complicated systems. Developing a methodology suitable for calculating electron-impact ionization cross sections for more complicated atoms and molecules is the real challenge to the electron-scattering theory community. The present work is a significant step toward being able to obtain detailed information for the ionization of multi-electron targets. Other promising methods are currently under development, and the ultimate solution will undoubtedly draw on methods and concepts from several of these efforts.

## 7.2 Shortcomings of this method

Although these calculations were remarkably successful, there is still room for improvement. The most obvious shortcoming is their inability to calculate differential cross sections over the range where one of the outgoing electrons carries most of the total energy. Linear extrapolation, in energy, of the SDCS is only marginally satisfactory, and, that procedure is useless for extending the energy sharing range over which we can calculate the TDCS.

The present method relies too heavily on being able to calculate the wave function at large distances. Extending the energy sharing range over which cross sections can be calculated, or simply improving the accuracy of the results, requires knowing the wave function at even larger distances. This "brute force" approach is unsatisfactory because perceptible improvements in the quality of the results require substantially increasing the size of the calculations.

Knowing the wave function at large distances is necessary mainly because of the extrapolation in the hyperradius used to obtain differential cross sections. Flux used in the extrapolation must be calculated in the near-asymptotic region where the aysmptotic form in Equation 2.11 holds. Furthermore, the procedure for extracting differential ionization cross sections from the wave functions is unable to distinguish between excitation of the atom into higher energy states and ionization with one electron carrying most of the energy. Thus, it relies on a significant portion of the ionization component being spatially separate from the discrete channels at the values of the hyperradius where the flux is actually calculated. Finally, since the procedure is based on direct calculations of the flux rather than integral expressions it is accurate only to first-order in wave function error.

Also, there are limitations to the range of incident energies for which we can calculate wave functions. Calculations for scattering very near the ionization threshold are problematic because all of the difficulties mentioned previously are magnified at lower energies. Numerical error in using finite difference over large distances for incident energies above 50 eV creates an upper bound to the range of energies accessible by the present implementation.

## 7.3 Improving the Method

An integral expression for the ionization flux would significantly improve the method. Some preliminary work toward developing such an expression [34] has already been done. An integral expression has the potential to be variational and, thus, less sensitive to wave function error which might allow the use of numerical methods that produce less accurate wave functions, but require fewer computational resources. A key promise of this approach is the possibility of extracting information only about ionization. Being able to better distinguish between ionization and discrete channels might extend the energy sharing range over which we can calculate differential cross sections. Also, we could expect the cross sections to converge much more rapidly as a function of grid size.

Changing the formalism to reduce the distances over which the wave function must be known is the best path to improving the method. We could also improve the results by using more efficient numerical methods to increase the range over which the wave function can be calculated. One promising approach is to replace finite difference with a finite element method using a set of discrete variable representation (DVR) basis functions. Finite elements have already been shown to work well with exterior complex scaling [20]. A DVR basis will lead to matrices that are smaller than those for finite difference, but with matrix elements that are just as easy to calculate.

Another possibility for increasing the distances at which the wave function can be calculated comes from noting that obtaining ionization cross sections by calculating flux requires the wave function only at large distances. ECS produces an arbitrarily accurate wave function on a finite region. If we want the wave function at larger distances we could employ a "marching" algorithm that uses the wave function already calculated on an interior region as a boundary condition for calculating the wave function on an exterior region. The outgoing nature of the scattered wave should allow for propagating it outward in this manner without significant numerical error.

## 7.4 Going beyond hydrogen

The primary motivation for improving on the present formalism is not to obtain better results for hydrogen but to move toward being able to calculate ionization cross sections for multi-electron atoms and even molecules. Although, in principle, ECS can be applied to arbitrarily complex systems, the present implementation is suitable only for two electron systems. Applying it to the ionization of one-electron ionic targets such as $\mathbf{e}^- + \mathbf{He}^+ \rightarrow 2\mathbf{e}^- + \mathbf{He}^{++}$ requires only straight-forward modifications. To extend it to multi-electron atoms one could treat the atom as having just one "active" electron with the inner electrons accounted for by a pseudo-potential. This approximation will work best for the alkalis, whose inner electrons form a closed shell.

The next great challenge to theoretical treatment of ionizing collisions is the complete solution to a true three-electron system. Simple extension of the methods used here is not feasible because of the increase in dimensionality that comes from adding a third electron. The first step will be solving some three-dimensional radial model

problem analogous to the Temkin-Poet model. Using the methods described in Chapter 3, this means directly solving for the scattered wave onto a three-dimensional grid. With currently available computational hardware, we cannot expect to be able to calculate a three-dimensional wave function, in this way, beyond about $25a_0$.

Another approach to the three-dimensional problem might be to reformulate it as a set of coupled two-dimensional problems where a known square integrable function represents one electron and a two-dimensional scattered wave describes the other two. This requires that we are willing and/or able to ignore double-ionization. Care must be taken to be sure that linear dependence is not introduced into the expansion of the three-dimensional wave function.

Moving from a three-dimensional model problem to a nine-dimensional, three-electron problem will be an imposing computational challenge. Converging the partial wave expansion of a three-electron wave function will probably require retaining many more terms than were necessary for the two-electron system. The barriers to computing three-dimensional radial functions combined with the requirements for converging a three-electron partial wave expansion ensure that calculation of an exact, three-electron scattering wave function will not be possible in the immediate future. The first useful results for electron-impact ionization in a three-electron system may very well come from some sort of coupled-channel approach.

Ultimately, the scattering theory community will develop theoretical methods that can calculate cross sections for electron-impact ionization of molecules. The implementation described here specifically assumes that the nucleus is located at the origin of the coordinate system and it cannot be used for molecular targets. Any method developed for molecules should be designed so that it can be interfaced with an existing quantum chemistry package. This suggests the need for a formalism that can be implemented by a basis set expansion. Sharp exterior complex scaling is incompatible with ordinary basis sets. One alternative is to use a smooth contour, another is to devise a finite element scheme that can be interfaced with quantum chemistry codes but still use a sharp exterior complex scaling contour.

# Bibliography


1. E. O. Alt, A. S. Kadyrov, and A. M. Mukhamedzhanov. Approximate triangle amplitude for three-body charge exchange processes. *Phys. Rev. A*, 53:2438, 1996.

2. N. R. Badnell, M. S. Pindzola, I. Bray, and D. C. Griffin. Time-independent and time-dependent close-coupling methods for electron-impact ionization of $Mg^{+}$, $Al^{2+}$ and $Si^{3+}$. *J. Phys. B*, 31:911, 1998.

3. M. Baertschy, T. N. Rescigno, W. A. Isaacs, and C. W. McCurdy. Benchmark single-differential ionization cross section results for the s-wave model of electron-hydrogen scattering. *Phys. Rev. A*, 60:R13, 1999.

4. R. Barrett, M. Berry, T. Chan, J. Demmel, J. Donato, J. Dongarra, V. Eijkhout, V. Pozo, C. Romine, and H. van der Vorst. *Templates for the Solution of Linear Systems.* SIAM, Philadelphia, 1994.

5. Gy. Bencze and Colston Chandler. Impossibility of distinguishing between identical particles in quantum collision processes. *Phys. Rev. A*, 59:3129, 1999.

6. I. Bray. Close-coupling theory of ionization: Successes and failures. *Phys. Rev. Letts.*, 78:4721, 1997.

7. I. Bray. Reply to "impossibility of distinguishing between identical particles in quantum collision processes". *Phys. Rev. A*, 59:3133, 1999.

8. I. Bray and D. Fursa. Calculation of ionization within close-coupling formalism. *Phys. Rev. A*, 54:2991, 1996.

9. I. Bray and A. T. Stelbovics. Convergent close-coupling calculations of electron-hydrogen scattering. *Phys. Rev. A*, 46:6995, 1992.

10. I. Bray and A. T. Stelbovics. Explicit demonstration of the convergence of the close-coupling method for a coulomb three-body problem. *Phys. Rev. Letts.*, 69:53, 1992.

11. I. Bray and A. T. Stelbovics. Calculation of the total ionization cross section and spin asymmetry in electron-hydrogen scattering from threshold to 500 ev. *Phys. Rev. Letts.*, 70:746, 1993.

12. Igor Bray. Electron-impact ionization of atomic hydrogen from near threshold to high energies. Draft of a manuscript submitted to *J. Phys. B*, April 1999.

13. P. G. Burke, D. F. Gallaher, and S. Geltman. Electron scattering by atomic hydrogen using a pseudo-state expansion I. elastic scattering. *J. Phys. B*, 2:1142, 1969.

14. P. G. Burke and J. F. B. Mitchell. Electron scattering by atomic hydrogen using a pseudo-state expansion IV. the convergence of the $s$-state expansion at intermediate energies. *J. Phys. B*, 6:320, 1973.

15. P. G. Burke and T. G. Webb. Electron scattering by atomic hydrogen using a pseudo-state expansion III. excitation of 2s and 2p states at intermediate energies. *J. Phys. B*, 3:L131, 1970.

16. James W. Demmel. *Applied Numerical Linear Algebra.* SIAM, Philadelphia, 1997.

17. S. Geltman and P. G. Burke. Electron scattering by atomic hydrogen using a pseudo-state expansion II. excitation of 2s and 2p states near threshold. *J. Phys. B*, 3:1062, 1970.

18. W. A. Isaacs, C. W. McCurdy, and T. N. Rescigno. Theoretical support for a ramsauer-townsend minimum in electron-$CF_4$ scattering. *Phys. Rev. A*, 58:309, 1998.

19. Xiaoye S. Li and J. W. Demmel. Making sparse gaussian elimination scalable by static pivoting. In *Proceedings of the ACM/IEEE SC 98 Conference*, Los Alamitos, CA, November 1998. IEEE.

20. C. W. McCurdy, T. N. Rescigno, and D. A. Byrum. Approach to electron-impact ionization that avoids the three-body coulomb asymptotic form. *Phys. Rev. A*, 56:1958, 1997.

21. Albert Messiah. *Quantum Mechanics, Volume II.* North-Holland Publishing Company, Amsterdam, 1961.

22. D. H. Oza. Convergence of pseudostate expansions in electron-hydrogen scattering. *Phys. Rev. A*, 30:1101, 1984.

23. D. H. Oza and J. Callaway. Pseudostate expansion in a simplified model of electron-hydrogen scattering. *Phys. Rev. A*, 27:2840, 1983.

24. I. C. Percival and M. J. Seaton. The partial wave theory of electron-hydrogen atom collisions. *Proc. Cambridge Phil. Soc.*, 53:654, 1957.

25. R. K. Peterkop. *Opt. Spectrosc.*, 13:87, 1962.

26. R. Poet. The exact solution for a simplified model of electron scattering by hydrogen atoms. *J. Phys. B*, 11:3081, 1978.

27. R. Poet. Symmetrically coupled partial differential equations in scattering i. model electron-hydrogen collisions. *J. Phys. B*, 13:2995, 1980.

28. T. N. Rescigno, M. Baertschy, D. Byrum, and C. W. McCurdy. Making complex scaling work for long-range potentials. *Phys. Rev. A*, 55:4253, 1997.

29. T. N. Rescigno, M. Baertschy, W. A. Isaacs, and C. W. McCurdy. Collisional breakup in a quantum system of three charged particles. *Science*, 286:2474, December 24, 1999.

30. T. N. Rescigno, C. W. McCurdy, W. A. Isaacs, and M. Baertschy. Use of two-body close-coupling formalisms to calculate three-body breakup cross sections. *Phys. Rev. A*, 60:3740, 1999.

31. T. N. Rescigno, C. W. McCurdy, A. E. Orel, and B. H. Lengsfield III. The Complex Kohn Variational Method. In Winifred M. Huo and Franco A. Gianturco, editors, *Computational Methods for Electron-Molecule Collisions*. Plenum Press, 1995.

32. J. Röder, H. Ehrhardt, C. Pan, A. F. Starace, I. Bray, and D.V. Fursa. Absolute triply differential $(e, 2e)$ cross section measurements for H with comparison to theory. *Phys. Rev. Lett.*, 79:1666, 1997.

33. J. Röder, J. Rasch, K. Jung, C. T. Whelan, H. Ehrhardt, R.J. Allan, and H.R.J. Walters. Coulomb three-body effects in low-energy impact ionization of H($1s$). *Phys. Rev. A*, 53:225, 1996.

34. M. R. H. Rudge. Theory of ionization of atoms by electron impact. *Rev. Mod. Phys.*, 40:564, 1968.

35. T. W. Shyn. Doubly differential cross sections of secondary electrons ejected from atomic hydrogen by electron impact. *Phys. Rev. A*, 45:2951, 1992.

36. B. Simon. The definition of molecular resonance curves by the method of exterior complex scaling. *Phys. Letts. A*, 71:211, 1979.

37. John R. Taylor. *Scattering Theory: The Quantum Theory of Nonrelativistic Collisions*. Robert E. Krieger Publishing Company, Malabar, FL, 1987.

38. A. Temkin. Nonadiabatic theory of electron-hydrogen scattering. *Phys. Rev.*, 126:130, 1962.

39. R. N. Zare. *Angular Momentum: Understanding Spatial Aspects in Chemistry and Physics*. John Wiley & Sons, 1988.

# Appendix A

# One Dimensional Potential Scattering Examples

Potential scattering provides an simple context for studying the method of exterior complex scaling without the complications from inelastic processes and multiple dimensions. The $l = 0$ components of partial wave expansions for scattering from spherical potentials provide simple test problems for any method in quantum collision theory. There already exist a variety of ways to treat potential scattering that can calculate scattering information to arbitrary accuracy. Thus, we can thoroughly evaluate exterior complex scaling by comparing its results with calculations from other methods. We will examine the effects of changing the complex scaling angle and the complex scaling point for both a short-range and a long-range potential.

## A.1 Potential scattering

One-dimensional potential scattering describes the scattering of two particles interacting via a central potential $V(r)$ that depends on only the inter-particle distance. For incident momentum $\hbar k_i$ we write the wave function $\Psi^+$ as the sum of an outgoing wave $\Psi^+_{\rm sc}$ and a plane wave representing the initial state.

$$\Psi^+(\vec{r}) = e^{ik_i z} + \Psi^+_{\rm sc}(\vec{r}) \tag{A.1}$$

The scattered wave $\Psi^+_{\rm sc}$ is obtained by calculating the radial functions $\psi^+_l(r)$ for each angular momentum quantum number $l$ in a partial wave expansion.

$$\Psi^+_{\rm sc}(\vec{r}) = \sum_{l=0}^{\infty} i^l \frac{\sqrt{4\pi(2l+1)}}{k_i r} Y_{l0}(\hat{r}) \psi^+_l(r) \tag{A.2}$$

With no angular dependence in $V(r)$, the $\psi^+_l$ are all independent of each other. They are outgoing solutions to one-dimensional scattered wave equations with reduced mass $\mu$ and regular Riccati-Bessel functions $\hat{j}_l$ from the expansion of $e^{ik_i z}$.

$$\left[E + \frac{\hbar^2}{2\mu}\frac{d^2}{dr^2} - \frac{\hbar^2}{2\mu}\frac{l(l+1)}{r^2} - V(r)\right] \psi^+_l(r) = V(r)\hat{j}_l(k_i r) \tag{A.3}$$

Each $\psi_l^+$ is a radially outgoing wave that, asymptotically, is proportional to a Hankel function $\hat{h}_l^+ \equiv \hat{n}_l + i\hat{j}_l$ where $\hat{n}_l$ is an irregular Riccati-Bessel function. For $l = 0$, $\hat{h}_0^+(x) = e^{ix}$.

$$\psi_l^+(r) \underset{r\to\infty}{\longrightarrow} e^{i\delta_l} \sin(\delta_l)\, \hat{h}_l^+(k_i r) \tag{A.4}$$

The proportionality factor in the asymptotic form of $\psi_l^+$ has the form given in Equation A.4 where the phase shift $\delta_l$ is a real number.

The total cross section is the sum of partial wave cross sections $\sigma_l$, each of which is directly related to the phaseshift $\delta_l$.

$$\sigma = \sum_{l=0}^{\infty} \sigma_l, \qquad \sigma_l \equiv 4\pi(2l+1)\tfrac{1}{k_i^2} \sin^2(\delta_l) \tag{A.5}$$

Thus, the $\delta_l$ provide a complete description of the final state. We can obtain them from the amplitude $f_l$ defined below.

$$f_l(k_i) = -\frac{2\mu}{\hbar^2 k_i^2} \int_0^{\infty} \hat{j}_l(k_i r) V(r) \left[\hat{j}_l(k_i r) + \psi_l^+(r)\right] dr \tag{A.6}$$

Since $f_l$ is proportional to $e^{i\delta_l} \sin(\delta_l)$ (see, for example, Taylor [37]), the tangent of the phase shift is equal to the imaginary part of $f_l$ divided by the real part.

$$\tan(\delta_l) = \frac{\mathrm{Im}(f_l)}{\mathrm{Re}(f_l)} \tag{A.7}$$

The integral expression in Equation A.6 is less sensitive to wave function error than is directly calculating scattered flux, but still provides complete scattering information.

## A.2 Complex Kohn method

In this appendix we will examine the accuracy of results calculated using complex scaling by comparing with results calculated using the more established complex Kohn [31] variational method. Complex Kohn has been successfully applied to electron-scattering from relatively large molecules [18]. However, like most other methods in scattering theory, it is suited only for discrete scattering processes and can not be applied to ionization.

The complex Kohn method expands the scattered wave in a set of basis functions consisting of one function that has the exact asymptotic form of an outgoing wave $\hat{h}_l^+(k_i r)$ and as many square-integrable functions as needed to converge the calculated wave function. Thus, the complex Kohn method produces the correct scattered wave over all space. We can gauge the accuracy of results in the complex Kohn method by observing the convergence of calculated phase shifts as more square-integrable functions are added to the expansion basis.

To devise one-dimensional scattering problems with which to study and test numerical methods we need consider only the $l = 0$ partial wave. For this case the term

| | $V(r) = \frac{15}{2}r^2e^{-r}$ | | | $V(r) = (1+r)^{-4}$ | | |
|---|---|---|---|---|---|---|
| $N$ | $k = 0.15$ | $k = 0.35$ | $k = 0.55$ | $k = 0.15$ | $k = 0.35$ | $k = 0.55$ |
| 5 | -1.2683674 | 0.3121880 | -0.9936457 | -0.0611095 | -0.1004421 | -0.1187034 |
| 10 | -1.2679899 | 0.3286518 | -1.0021799 | -0.0611092 | -0.1004424 | -0.1187109 |
| 15 | -1.2679887 | 0.3286586 | -1.0021589 | -0.0611095 | -0.1004425 | -0.1187108 |
| 20 | -1.2679887 | 0.3286588 | -1.0021585 | -0.0611095 | -0.1004425 | -0.1187109 |
| 25 | -1.2679887 | 0.3286588 | -1.0021585 | -0.0611095 | -0.1004425 | -0.1187109 |

Table A.1: Convergence, in number of square-integrable basis functions $N$, of $l = 0$ phase shifts calculated with the complex Kohn method.

from the plane wave initial state is $\hat{j}_0(k_i r) = \sin(k_i r)$ and asymptotically the radial function $\psi^+_{l=0}$ is an outgoing spherical wave proportional to $e^{ik_i r}$. For later convenience we will rewrite the expression for the amplitude $f_l$ as the sum of two integrals.

$$f_0(k_i) = -\frac{2\mu}{\hbar^2 k_i^2}\left\{\int_0^\infty \sin^2(k_i r)V(r)dr + \int_0^\infty \sin(k_i r)V(r)\psi^+_{l=0}(r)dr\right\} \tag{A.8}$$

Once $\psi^+_{l=0}$ is calculated by solving Equation A.3 for $l = 0$ we use Equation A.8 to compute $f_0$ and then obtain the $l = 0$ phase shift.

In the remainder of this appendix we will examine the application of complex scaling to potential scattering with a short-range potential, $V(r) = \frac{15}{2}r^2e^{-r}$, and a long-range potential, $V(r) = (1+r)^{-4}$. Values of the phase shifts calculated using the complex Kohn method for both potentials at three different energies are listed in Table A.1. Convergence of the calculated phase shifts as more square-integrable functions are added to the basis is very rapid.

## A.3 Uniform complex scaling

We will first consider the simplest complex contour, $r \to re^{i\eta}$. Under this uniform complex scaling transformation the wave function is complex-scaled everywhere so there is no region where the calculated $\psi^+_l$ is equal to the "physical", unscaled scattered wave function. However, we can can still extract scattering information from it. The first integral in Equation A.8 involves $\sin(k_i r)$ and the potential $V$. It exists provided the potential decays to zero faster than $\frac{1}{r}$ for large $r$. Since the integrand in the first term is a known function, that term can simply be integrated numerically along the real axis. So, no complex scaling should be used for the first term.

The second integral, on the other hand, involves the unknown scattered wave. Again, this integral exists provided the potential goes to zero fast enough. However, if we use complex scaling to evaluate the scattered wave then we know $\psi^+_l$ only on the complex contour and the integration must be done along that contour. Under complex scaling, with a scaling angle $\eta$ in the range $0 < \eta < 90^o$, the scattered wave

decays exponentially, but $\sin(k_i r)$ increases exponentially. The product of the two, however, remains bounded.

$$\sin(k_i r e^{i\eta}) V(r e^{i\eta}) \psi^+_{l=0}(r e^{i\eta}) \underset{r\to\infty}{\longrightarrow} \frac{1}{2i} e^{i\delta_0} \sin(\delta_0) \left[ e^{-2k_i r \sin(\eta)} e^{i2k_i r \cos(\eta)} - 1 \right] V(r e^{i\eta}) \tag{A.9}$$

Asymptotically, the second integrand from Equation A.8 decays exactly as the potential $V$ evaluated on the contour.

Thus, the second integral from Equation A.8 exists along any uniform complex contour provided that $V(re^{i\eta})$ decays sufficiently fast. Since the potential will force the integrand to zero as $r \to \infty$ the integral along any complex contour is identical to the integral along the real axis. Therefore, if we know the scattered wave function along some contour $z(r)$ then we can calculate the correct amplitude by evaluating $\sin(k_i z(r))$ and $V(z(r))$ and then integrating along that contour.

Knowing that the integral involving the scattered wave exists along some complex contour is not useful unless the scattered wave can be calculated on that contour. The scattered wave is obtained by solving the scattered wave equation in Equation A.3 whose driving term, $V(z(r)) \sin(k_i z(r))$, is well behaved only if the potential decays more rapidly than the exponential increase of $\sin(k_i e^{i\eta})$. This requires the potential to be exponentially decreasing. Suppose the potential decays like $e^{-\alpha r}$, then the requirement that $V(re^{i\eta}) \sin(k_i r e^{i\eta})$ go to zero restricts the complex scaling angle to $0 < \tan(\eta) < \frac{\alpha}{k_i}$. So, uniform complex scaling is more problematic at higher energies.

Phase shifts for scattering from a potential with decay constant $\alpha = 1 a_0^{-1}$ that are calculated using several scaling angles are listed in Table A.2. For energies with $k_i$ of 0.15 and 0.35 $a_0^{-1}$ it is possible to use scaling angles as large as $60^o$. However, when $k_i = .55 a_0^{-1}$ a scaling angle of $60^o$ causes numerical instability that comes from having to evaluate $\sin(z)$ for arguments with large imaginary parts. The results are essentially independent of the complex scaling angle, and agree with the correct values calculated using complex Kohn, provided that the angle lies within the allowed range. One caveat is that with smaller scaling angles the scattered wave decays more slowly which requires that it be calculated over a larger range of $r$.

| scaling angle | $k = 0.15$ | $k = 0.35$ | $k = 0.55$ |
|---|---|---|---|
| $20^o$ | -1.2679889 | 0.3286587 | -1.0021581 |
| $40^o$ | -1.2679887 | 0.3286587 | -1.0021584 |
| $60^o$ | -1.2679884 | 0.3286587 | -1.4261539 |
| complex Kohn | -1.2679887 | 0.3286588 | -1.0021585 |

Table A.2: Phase shifts for $V(r) = \frac{15}{2} r^2 e^{-r}$ calculated with uniform complex scaling using different scaling angles.

| scaling point | $k = 0.15$ | $k = 0.35$ | $k = 0.55$ |
|---|---|---|---|
| $0a_0$ | -1.2679887 | 0.3286587 | -1.0021585 |
| $20a_0$ | -1.2679887 | 0.3286588 | -1.0021585 |
| $40a_0$ | -1.2679887 | 0.3286588 | -1.0021585 |
| complex Kohn | -1.2679887 | 0.3286588 | -1.0021585 |

Table A.3: Phase shifts for $V(r) = \frac{15}{2}r^2e^{-r}$ calculated using exterior complex scaling with a scaling angle of $30^o$ and three different complex scaling points.

## A.4 Exterior complex scaling

For exterior complex scaling (ECS) we generalize the definition of the contour so that the coordinates are complex only beyond some distance $R_0$. Uniform complex scaling is then the special case of $R_0 = 0$.

$$z(r) \equiv \begin{cases} r & r < R_0 \\ R_0 + (r - R_0)e^{i\eta} & r \geq R_0 \end{cases} \tag{A.10}$$

The second integral in Equation A.8 is still well-defined on this contour for the same reasons as for uniform complex scaling and it is possible to calculate the phase shift as long as the scattered wave is known on the contour. Since the potential will decrease more rapidly on the real axis than on a complex contour one advantage of using ECS rather than uniform complex scaling is that $R_0$ can be chosen so the potential is already close to zero before the complex scaling begins. Also, ECS allows the use of potentials that are known only numerically for small $r$.

Values of the phase shift for a short-range potential calculated using ECS with different complex scaling points $R_0$ are listed in Table A.3. The accuracy of the results is essentially independent of $R_0$. However, the size of the required calculation does depend on $R_0$. In a finite difference implementation, the extent of the grid needed depends upon the length beyond $R_0$ necessary for the $\psi_l^+(z(r))$ to decay effectively to zero. This distance is independent of $R_0$ so increasing $R_0$ increases the number of real grid points while the required number of complex grid points remains the same.

One advantage of using ECS is that $\psi_l^+(z(r))$ is the same as $\psi_l^+(r)$ between zero and the complex scaling point $R_0$. So, with ECS we obtain the actual wave function, but only on a finite region. Scattered waves calculated with ECS for different $R_0$ are compared, in Figure A.1, with one calculated by the complex Kohn method. In the region where the ECS contour is real the two wave functions are identical within the accuracy of the numerical methods used. The accuracy of the wave function over the region where the coordinates are real is independent of the complex scaling point $R_0$.

## A.5 Long-range potentials

Implementing ECS for potentials that do not decay exponentially is more difficult. The problem is not in calculating the phase shift (the second integral in Equation

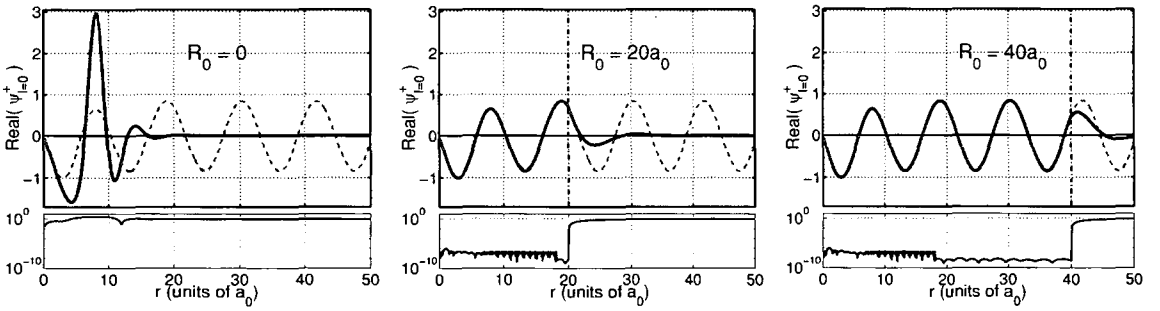


Figure A.1: Scattered waves for $V(r) = \frac{15}{2}r^2e^{-r}$ calculated using ECS for three different $R_0$ compared with one calculated using the complex Kohn method. The incident momentum is $k_i = 0.55a_0^{-1}$ and the complex scaling angle is $30^o$. Differences between ECS and complex Kohn wave functions are plotted on a log scale.

A.8 is still defined on the complex contour) instead the problem is in calculating the scattered wave. With long-range potentials the driving term in Equation A.3 diverges on the contour and the scattered wave equation cannot be solved without modification. In Appendix B it is shown that this limitation can be overcome by truncating the potential at (or before) the complex scaling point $R_0$.

Truncating the potential makes it possible to solve the scattered wave equation on the complex contour, but the potential is now different. Changing the potential will, of course, affect the solution so the calculated wave functions and phase shifts will be less accurate. Accuracy of the calculated phase shifts depends on how close to zero the potential is at $R_0$. As can be seen in Table A.4, the calculated phase shifts for a long-range potential are more sensitive to $R_0$ than they were for short-range potentials. However, they do converge to the correct, "physical" value as $R_0$ increases. The effect of truncating the potential on the calculated wave function is illustrated in Figure A.2 where wave functions calculated with ECS are compared to those calculated by the complex Kohn method.

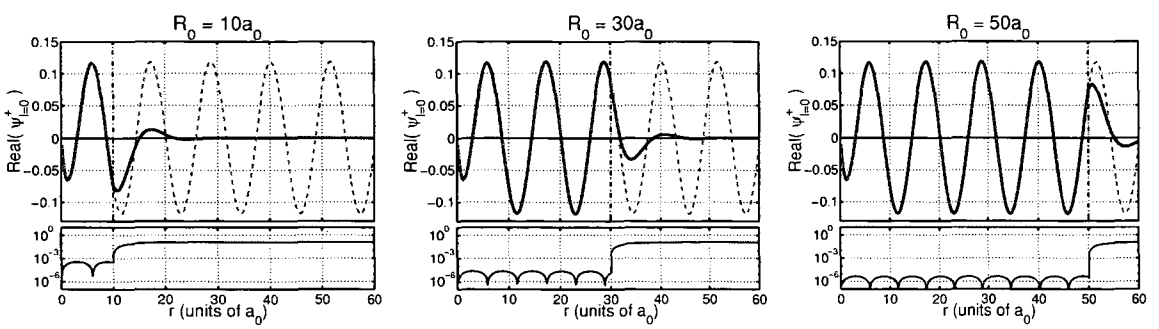


Figure A.2: Scattered waves for $V(r) = (1 + r)^{-4}$ calculated using ECS for three different $R_0$ compared with one calculated using the complex Kohn method. The incident momentum is $k_i = 0.55a_0^{-1}$ and the complex scaling angle is $30^o$. Differences between ECS and complex Kohn wave functions are plotted on a log scale.

| scaling point | $k = 0.15$ | $k = 0.35$ | $k = 0.55$ |
|---|---|---|---|
| $10a_0$ | -0.0562652 | -0.0989343 | -0.1179933 |
| $20a_0$ | -0.0607733 | -0.1002030 | -0.1185759 |
| $30a_0$ | -0.0609288 | -0.1003711 | -0.1186671 |
| $40a_0$ | -0.0610577 | -0.1004141 | -0.1186939 |
| $50a_0$ | -0.0610715 | -0.1004289 | -0.1187025 |
| $60a_0$ | -0.0610932 | -0.1004349 | -0.1187057 |
| $70a_0$ | -0.0610959 | -0.1004378 | -0.1187076 |
| $80a_0$ | -0.0611025 | -0.1004393 | -0.1187088 |
| $90a_0$ | -0.0611033 | -0.1004402 | -0.1187095 |
| complex Kohn | -0.0611095 | -0.1004425 | -0.1187109 |

Table A.4: Phase shifts for $V(r) = (1+r)^{-4}$ calculated using exterior complex scaling with a scaling angle of $30^o$ and several different complex scaling points. In each case, the potential is truncated at the complex scaling point. The complex Kohn values were calculated with a potential truncated at $250a_0$.

# Appendix B

# ECS and Long-Range Potentials

"Making complex scaling work for long-range potentials", originally published in Physical Review A [28], shows that exterior complex scaling can be used to calculate phase shifts for one-dimensional potential scattering with long-range potentials by performing the calculations with the potential truncated at the complex scaling point. The calculated results are meaningful if the complex scaling point is large enough so that the truncated potential is physically indistinguishable from the original long-range potential. Although the potential treated in this article is not as long-range as a Coulomb potential, the ideas developed here laid the groundwork for applying exterior complex scaling to electron-impact ionization. Also, this article demonstrates how to implement exterior complex scaling with an analytic basis set. The "sharp" contour of Equation A.10 is replaced by a "smooth" contour that has continuous first and second derivatives.

# Making complex scaling work for long-range potentials

T. N. Rescigno
*Physics and Space Technology Directorate, Lawrence Livermore National Laboratory, Livermore, California 94550*

M. Baertschy and D. Byrum
*Department of Applied Science, University of California, Davis, Livermore, California 94550*

C. W. McCurdy
*Computing Sciences Directorate, Lawrence Berkeley National Laboratory, Berkeley, California 94720*
(Received 23 December 1996)

We examine finite basis set implementations of complex scaling procedures for computing scattering amplitudes and cross sections. While ordinary complex scaling, i.e., the technique of multiplying all interparticle distances in the Hamiltonian by a complex phase factor, is known to provide convergent cross-section expressions only for exponentially bounded potentials, we propose a generalization, based on Simon's exterior complex scaling technique, that works for long-range potentials as well. We establish an equivalence between a class of complex scaling transformations carried out on the time-independent Schrödinger equation and a procedure commonly referred to as the method of complex basis functions. The procedure is illustrated with a numerical example. [S1050-2947(97)07406-4]

PACS number(s): 34.80.Bm, 03.65.Nk

## I. INTRODUCTION

The method of complex coordinates or complex scaling (i.e., the idea of treating the Hamiltonian as a function of complex position variables) is well known in physics. The idea was first used over 30 years ago in the theory of potential scattering to extend the region of analyticity of the Jost function into the lower half $k$ plane [1]. It also has a long history in atomic and molecular physics as the basis for various methods used in computational scattering theory dating back to the early seventies [2,3]. Most of the applications have centered on the calculation of resonances in atoms and molecules whose energies and lifetimes, under complex scaling, are related to the real and imaginary parts of the discrete eigenvalues of an analytically continued Hamiltonian [4]. Nevertheless, as Reinhardt pointed out in his 1982 review [5], it is important to bear in mind that the original motivation for interest in the method, and indeed the principal motivation for this study, was the prospect of calculating scattering cross sections without explicit enforcement of asymptotic boundary conditions. In contrast to the development of "direct" methods for evaluating resonances based on complex scaling [6], this other aspect has received far less attention [7,8] and, apart from applications to photoionization [9–12], has met with only partial success. The reason? A solution of the full scattering problem requires matrix elements of the resolvent between continuum functions. Unfortunately, the method of complex scaling as originally presented only provides convergent expressions for these quantities in the case of interaction potentials that fall off exponentially [2,13], which would appear to exclude most of the problems encountered in atomic and molecular physics. Although methods based on complex scaling or, more accurately, on the use of complex basis functions [8] have been proposed to tackle this harder problem, it is probably fair to say that, after many years, no definitive method for entirely circumventing the specification of boundary conditions has emerged.

One notable extension of the complex coordinate method was Simon's exterior complex scaling procedure [14], in which the coordinates are only scaled outside a (hyper)-sphere of radius $|\mathbf{r}|=R_0$. The motivation for this development was the desire to treat Hamiltonians that have nonanalyticities in the interior region, such as the Born-Oppenheimer Hamiltonian whose electron-nuclear attraction terms are not dilatation analytic when viewed solely as a function of the electronic coordinates [15]. In computational applications, exterior complex scaling has been used mainly in direct numerical integration methods [16–18], although there have been a few attempts, in connection with resonance evaluations, to implement the method in a basis [19–21].

The purpose of this paper is to show that exterior scaling can be used to formulate a procedure for solving the full scattering problem using only square-integrable functions and that, unlike the original complex scaling method, the method is not restricted to exponentially bounded potentials. To be able to implement the method with arbitrary basis functions, we have found it necessary to generalize Simon's procedure to a broader class of transformations, where the transition from real to scaled coordinates is smoothly carried out over a finite range.

The method is outlined in the following sections, after a brief review of the earlier techniques. We then make some comments on the connection between complex scaling and complex basis function methods. Section V presents some numerical examples and Sec. VI has some concluding remarks.

## II. COMPLEX SCALING

For notational simplicity, we will use the symbol $r$ to refer collectively to all the interparticle coordinates in an

$N$-body system. The starting point for a definition of the complex coordinate method is to introduce a scaling of $r$ by a real factor $e^{\theta} \in R$ under which the wave function is mapped as

$$\Psi(r) \rightarrow e^{N\theta/2}\Psi(e^{\theta}r), \tag{1}$$

where the factor $e^{N\theta/2}$ must be included to preserve the normalization of the wave function. Since $\theta$ is real, this corresponds to a unitary transformation of the Hamiltonian, $H_{\theta} = U(\theta)HU^{-1}(\theta)$, and the spectrum of $H_{\theta}$ is independent of $\theta$.

The complex coordinate method analytically continues $H_{\theta}$ by considering a broader class of (nonunitary) scaling transformations $e^{\theta}, \theta \in C$. In this paper, we use the terms "uniform" or "ordinary" complex scaling to denote this transformation which scales all interparticle coordinates by a complex constant. There is a considerable literature on the properties of the Hamiltonian under this (nonunitary) transformation for the class of *dilatation analytic* potentials [5,22], the principal results of which can be summarized as follows.

(1) The bound-state eigenvalues of $H_{\theta}$ are the same as those of $H$ for $|\arg\theta| \leq \pi/2$.

(2) The segments of the continuous spectrum of $H_{\theta}$ beginning at each scattering threshold are rotated into the lower half plane by an angle $2\,\mathrm{Im}\theta\,(\mathrm{Im}\theta > 0)$.

(3) $H_{\theta}$ may have isolated complex eigenvalues (resonances), and corresponding $L^2$ eigenfunctions, in the wedge formed by the continuous spectra of $H$ and $H_{\theta}$. They are independent of $\theta$ as long as they are not covered by branches of the continuous spectrum of $H_{\theta}$.

Property 3 has accounted for the attractiveness of uniform complex scaling as a means for finding resonances. Consider, for example, the case of $s$-wave scattering from a spherically symmetric potential $V(r)$. One simply chooses a basis of $L^2$ functions, forms a (complex symmetric) matrix representation of the operator

$$H_{\theta}(r) = -\frac{1}{2}e^{-2\theta}\frac{d^2}{dr^2} + V(re^{\theta}), \tag{2}$$

diagonalizes it and varies $\theta$ to find those eigenvalues which are roughly independent of the scaling angle. In practice, the eigenvalues may depend strongly on the rotation angle for basis sets that are not carefully optimized and modifications of the method, which need not concern us here, are needed to make the method practical for many-electron systems [23]. We refer the interested reader to several reviews for further details [5,6,24].

It is property 2 that has stimulated interest in complex scaling as a way to implement scattering theories that do not rely on explicit enforcement of asymptotic boundary conditions. The idea is to express the quantity of interest, such as a scattering amplitude, as a matrix element of the resolvent or full Green's function $\lim_{\varepsilon \to 0}(E - H + i\varepsilon)^{-1}$ and to use the fact that the latter can be approximated as the inverse of the matrix representation of $E - H_{\theta}$ in an $L^2$ basis, i.e., as $(\tilde{E} - \tilde{H}_{\theta})^{-1}$ [2,8]. Because the continuous spectrum of $H_{\theta}$ has been rotated off the real axis, the matrix $(\tilde{E} - \tilde{H}_{\theta})^{-1}$ is a meaningful approximation to the resolvent *for real values of* $E$. To evaluate the scattering amplitude or $T$ matrix, we require matrix elements of the resolvent between continuum functions. Specifically, what is required is $\lim_{\varepsilon \to 0}\langle \psi_0 | V(E - H + i\varepsilon)^{-1} V | \psi_0 \rangle$, where $\psi_0$ is a continuum function. Unfortunately, with ordinary complex scaling, these so-called "free-free" elements only converge for exponentially bounded potentials $V$ [2,13]. Our main purpose here will be to show how such a construction can be made to work even in the case of a Hamiltonian with long-range interactions.

The method of exterior complex scaling was proposed by Simon [14] as a logical extension of uniform complex scaling to deal with potentials that may have interior nonanalyticities, but are well behaved outside some (hyper)sphere of finite volume [25]. Specifically, Simon suggested the mapping

$$Q_{R_0,\phi}(r) = \begin{cases} r, & r < 0 \\ R_0 + (r - R_0)e^{i\phi}, & r \geq R_0 \end{cases} \tag{3}$$

The spectral properties of the Hamiltonian under this more general scaling transformation are the same as those listed above for uniform complex scaling. The particular example that prompted Simon's work was the Born-Oppenheimer Hamiltonian with fixed, real nuclear coordinates. The nonanalyticity of the electron-nuclear attraction terms spell trouble for uniform scaling [15], but are readily accommodated under exterior complex scaling.

The slope of the contour defined by Simon's exterior complex scaling changes discontinuously at $R_0$, which can complicate its implementation in certain applications [26]. We will therefore first consider a more general class of transformations which pass smoothly from real to complex $r$ and then return to exterior complex scaling as a limiting case. We will use the term smooth exterior scaling to distinguish this class of mappings from Simon's original prescription, which we call sharp exterior scaling, while the term "complex scaling" without modifiers can refer to any method which allows the position variables to take on complex values.

Consider some smooth complex contour $R(r)$ which has the properties

$$R(r) = \begin{cases} r, & r \rightarrow 0 \\ re^{i\phi}, & r \rightarrow \infty \end{cases} \tag{4}$$

but is otherwise arbitrary. We first need to determine the explicit form of the transformed Schrödinger equation as a function of the real coordinate $r$.

The implementation of complex scaling requires that one take into account the metric which accompanies the scaling operator. In analogy with Eq. (1), we define the operator that does the scaling as

$$U\Psi(r) = J(r)\Psi(R(r)), \tag{5}$$

where the Jacobian is

$$J(r) = \left(\frac{dR}{dr}\right)^{1/2} \tag{6}$$

and the scaled Schrödinger equation is

$$UHU^{-1}U\Psi = EU\Psi. \tag{7}$$

The inverse of $U$ is given by

$$U^{-1}\Psi = \frac{1}{J(R^{-1}(r))}\Psi(R^{-1}(r)), \tag{8}$$

where $R^{-1}(r)$ is the inverse of the function defining the contour.

Next, we need an expression for the radial kinetic-energy operator under this transformation. The algebra simplifies considerably if we represent the contour in the following form [26]:

$$R(r) = \int_0^r q(r')dr', \tag{9}$$

with

$$q(r) = \begin{cases} 1, & r \to 0 \\ e^{i\phi}, & r \to \infty \end{cases} \tag{10}$$

so that

$$J(r) = q^{1/2}(r) \tag{11}$$

for functions $q$ that are continuous. Finally, if we define $\varphi(r)$ as the original wave function on the contour, i.e.,

$$U\Psi(r) \equiv J(r)\varphi(r) = q^{1/2}(r)\varphi(r), \tag{12}$$

then it can be shown that

$$U\frac{d^2}{dr^2}U^{-1}(r)q^{1/2}(r)\varphi(r) = \frac{1}{q^2}q^{1/2}\varphi'' - \frac{q'}{q^3}q^{1/2}\varphi', \tag{13}$$

where the primes denote differentiation with respect to the real coordinate $r$. The transformed radial Schrödinger equation $\hat{H}\varphi(r) = E\varphi(r)$ involves the Hamiltonian operator

$$\hat{H}(r) = -\frac{1}{2}\left[\frac{1}{q^2}\frac{d^2}{dr^2} - \frac{q'}{q^3}\frac{d}{dr}\right] + V(R(r)). \tag{14}$$

This representation of the second derivative operator now allows us to derive a symmetric matrix representation of the scaled Schrödinger equation in a basis. The idea is to expand just $\varphi(r) \equiv \Psi(R(r))$, and not $U\Psi(r)$ which contains the Jacobian factor, in a basis

$$\varphi(r) = \sum_n C_n \chi_n(r). \tag{15}$$

Inserting this expression into Eq. (14), multiplying from the left with $q(r)\chi_m(r)$ and integrating over $r$ gives

$$\sum_n \tilde{H}_{mn}C_n = E\sum_n \tilde{S}_{mn}C_n, \tag{16}$$

with

$$\tilde{S}_{mn} = \int_0^\infty \chi_m(r)\chi_n(r)q(r)dr, \tag{17}$$

$$\tilde{H}_{mn} = \tilde{T}_{mn} + \tilde{V}_{mn}, \tag{18}$$

$$\tilde{V}_{mn} = \int_0^\infty \chi_m(r)V(R(r))\chi_n(r)q(r)dr, \tag{19}$$

$$\tilde{T}_{mn} = -\frac{1}{2}\int_0^\infty \chi_m(r)\left[\frac{1}{q(r)}\chi_n''(r) - \frac{q'(r)}{q^2(r)}\chi_n'(r)\right]dr, \tag{20a}$$

$$= \frac{1}{2}\int_0^\infty \chi_m'(r)\frac{1}{q(r)}\chi_n'(r)dr, \tag{20b}$$

where the last expression comes from integration by parts and the assumption that the basis functions vanish at the origin and infinity. Note that the kinetic-energy elements given by Eq. (20b) obviously define a *complex symmetric* matrix.

Equations (17)–(20) which, together with the transformed Hamiltonian in Eq. (14), are the principal results of this section, show how to represent the transformed radial Schrödinger equation in a basis. In the limiting case of sharp exterior scaling, $q(r)$ changes discontinuously from 1 to $e^{i\phi}$ at $r = R_0$ and some care is needed to properly define the kinetic-energy elements. It can be shown that Eq. (20b) still gives the correct representation of the kinetic-energy operator in this instance. Note that, unlike Kurasov, Scrinzi, and Elander [26], we have not included the Jacobian factor $\sqrt{q(r)}$ in the definition of the scaled wave function in Eq. (5) so that, under sharp exterior scaling, $\Psi(R(r))$ is *not* discontinuous at $R_0$. However, the derivatives of $\Psi(R(r))$ (with respect to $r$) are discontinuous. The implication is that, even with the kinetic-energy operator properly defined via Eq. (20b), an analytic basis set cannot give uniform convergence with sharp exterior scaling because such an expansion cannot represent the cusp discontinuity in the wave function at $R_0$.

## III. COMPLEX SCALING VS COMPLEX BASIS FUNCTIONS

At this point, it is possible to establish a connection between complex scaling and another class of techniques commonly referred to as complex basis function methods. For some implementations of complex scaling, it is possible to reinterpret the prescription of using real $L^2$ functions in connection with a complex Hamiltonian as being entirely equivalent to using complex basis functions with a real Hamiltonian. For example, with uniform scaling, we have $q(r) = e^{i\phi} \forall r$ and thus have to construct matrix elements of the form

$$I = e^{i\phi}\int_0^\infty \chi_m(r)H(re^{i\phi})\chi_n(r)dr. \tag{21}$$

It is easy to see that if we make the change of variable $r \to re^{-i\phi}$ in the above integral and use Cauchy's theorem to distort the integration contour back to the real axis, we get

$$I = \int_0^\infty \chi_m(re^{-i\phi})H(r)\chi_n(re^{-i\phi})dr, \tag{22}$$

so that we can view the case of uniform scaling as being equivalent to using a real Hamiltonian and working with

complex basis functions $\chi_n(re^{-i\phi})$ and a scalar product defined without complex conjugation of the radial functions. While complex scaling and complex basis functions are equivalent in this simple case, the complex basis function interpretation turned out to be more flexible, since it allowed one to mix real and complex basis functions in many-body problems where the wave functions are represented as orbital products. The inner-core orbitals in a heavy atom become highly oscillatory under uniform complex scaling which causes severe convergence problems. With complex basis function methods, one can use real basis functions to expand the core orbitals and complex functions only for the outer orbitals [23]. The method is then no longer the same as uniform complex scaling and may well not correspond to an easily derived variable scaling of the Hamiltonian operator. The "method of complex basis functions" [23,24] played an important role in the evolution of numerical scattering methods, since it enabled practical calculations to be performed on many-electron atoms as well as molecules. In fact, some progress was made in establishing a relationship (but not an identity) between computations carried out with complex basis functions and the exterior complex scaling concept [27].

The development of the preceding section enables us to make a clearer connection between complex scaling and complex basis functions. The matrix elements we have to consider [Eqs. (17), (19), and (20)] have the form

$$\tilde{H}_{mn} = \int_0^\infty \chi_m(r) H(R(r)) \chi_n(r) q(r) dr = \int_0^\infty \chi_m(r) H(R(r)) \chi_n(r) \frac{dR}{dr} dr. \quad (23)$$

If we can construct $R^{-1}$, the inverse of the function which defines the contour, then we can make the change of variable from $r$ to $x$, where $r = R^{-1}(x)$ and again use Cauchy's theorem to carry out the integration along the real $x$ axis. The result is

$$\tilde{H}_{mn} = \int_0^\infty \chi_m(R^{-1}(x)) H(x) \chi_n(R^{-1}(x)) dx, \quad (24)$$

which establishes the desired connection between complex scaling and an equivalent complex basis. For the case of uniform complex scaling, as well as sharp exterior scaling, the inverse map is simply $R^{-1}(r) = r^*$. In fact, any smooth mapping that satisfies

$$R^{-1}(x) = \begin{cases} x, & x \to 0 \\ xe^{-i\phi}, & x \to \infty \end{cases} \quad (25)$$

and has a smooth inverse can be used to define a set of complex basis functions to use in Eq. (24). Note that with exterior scaling, there is no need for mixing real and complex basis functions; the inner-core orbital problem in many-electron systems is automatically handled in a natural way, since tight functions that do not extend beyond $R_0$ are effectively left real.

## IV. SCATTERING

We will next investigate the question of applying the formalism outlined above to a collision problem. For simplicity, we will consider the case of $s$-wave scattering from a spherically symmetric potential. The scattering cross section is proportional to the squared modulus of the $T$ matrix, which is defined as

$$T(E) = \int_0^\infty \psi_0(r) V(r) \psi^\dagger(r) dr \equiv \int_0^\infty \psi_0(r) V(r) (\psi_0(r) + \psi^{\text{scat}}(r)) dr, \quad (26)$$

where $\psi^{\text{scat}}(r)$ is the scattered wave part of the full scattering wave function. The $T$ matrix can also be expressed in terms of the full Green's function

$$T(E) = \int_0^\infty \psi_0(r)(V(r) + V(r) G^+(r,r') V(r')) \psi_0(r) dr\, dr' = \lim_{\varepsilon \to 0} \langle \psi_0 | V + V(E + i\varepsilon - H)^{-1} V | \psi_0 \rangle, \quad (27)$$

with

$$\psi_0 = \sqrt{2/k} \sin(kr), \quad E = k^2/2. \quad (28)$$

Note that with these definitions, $T = e^{i\delta} \sin\delta$, where $\delta$ is the phase shift. The scattered wave part of the $T$-matrix is now approximated as

$$\langle \psi_0 | V(E + i\varepsilon - H)^{-1} V | \psi_0 \rangle \approx \bar{f} \cdot (E\bar{S} - \bar{H}_\theta)^{-1} \cdot \bar{f}, \quad (29)$$

where the matrices $\bar{S}$ and $\bar{H}$ are defined in Eqs. (17)–(20) and $\bar{f}$ is a vector with elements

$$f_m = \sqrt{2/k} \int_0^\infty \chi_m(r) V(R(r)) \sin(kR(r)) q(r) dr, \quad (30)$$

Since the continuous spectrum of $H_\theta$ has been rotated into the lower half plane, this representation should converge for real $E$ if $V$ is sufficiently well behaved. Unfortunately, as Baumel, Crocker, and Nuttall [13] have pointed out, $V(r)$ must be exponentially bounded for Eq. (29) to converge since $\sin(kr)$ diverges exponentially under coordinate rotation. This will be formally true both for uniform scaling or exterior scaling. With exterior complex scaling, however, there is a way around this problem.

Although the development to this point allows any switching function $q(r)$ that satisfies Eq. (10), we will see that there are distinct advantages to having a contour that coincides *exactly* with the real axis over a finite range $0 \leq r \leq R_0$. We can then replace the original potential $V(r)$ by a finite range potential $V_{R_0}(r)$ that vanishes beyond $R_0$ and is identical to $V(r)$ for $r < R_0$

$$V_{R_0}(r) = \begin{cases} V(r), & r \leq R_0 \\ 0, & r > R_0 \end{cases}. \quad (31)$$

We can use exterior scaling to calculate the $T$ matrix corresponding to this potential $T_{R_0}$ relying on Eq. (29) to approxi-

mate the scattered wave part in a basis set of $N$ square-integrable functions with Eqs. (17)–(20) defining the required matrix elements. Since $V_{R_0}(r)$ is a finite-range potential, the method will converge for any value of $R_0$ if $N$ is large enough. This truncation of the potential allows us to define a process that limits to the correct physical result as $R_0 \to \infty$. Thus, by choosing the *interior* region large enough, we can insure that the truncated potential differs insignificantly from the physical potential under consideration [28].

We can contrast the above procedure to the situation that pertains to uniform complex scaling with a truncated long-range potential. In the latter case, it is convenient to use the "complex basis set" interpretation of uniform scaling [i.e., Eq. (22)], so that we can continue to use the same real, finite-range potential $V_{R_0}(r)$. The matrix elements of the potential would then be of the form

$$I_{R_0} = \int_0^{R_0} \chi_m(re^{-i\phi}) V(r) \chi_n(re^{-i\phi}) dr. \tag{32}$$

In contrast to the case of exterior scaling with $V_{R_0}(r)$, uniform scaling will not yield physically meaningful results as $R_0$ is increased. Indeed, in the limit $R_0 \to \infty$, the matrix elements defined in Eq. (32) become, after the change of variable $r \to re^{i\phi}$

$$\lim_{R_0 \to \infty} I_{R_0} = e^{i\phi} \int_0^{\infty} \chi_m(r) V(re^{i\phi}) \chi_n(r) dr, \tag{33}$$

which is precisely the case that Baumel, Crocker, and Nuttall [13] showed to be divergent.

We will now give the specific form of the transformation we used to implement smooth exterior scaling. We chose

$$q(r) = \begin{cases} 1, & r < R_0 - h \\ f(r), & R_0 - h < r < R_0 + h, \\ e^{i\phi}, & r > R_0 + h \end{cases} \tag{34}$$

where $f(r)$ is a smooth switching function defined on $[R_0 - h < r < R_0 + h]$. To insure uniform convergence with an analytic basis, we want $f(r)$ to be continuously differentiable at $r = R_0 \pm h$. We thus chose $f(r)$ to be the lowest order polynomial needed to make $q(r)$ and $q'(r)$ continuous at $R_0 - h$ and $R_0 + h$. If we define

$$f(r) = 1 + (e^{i\phi} - 1) P\left(\frac{r - R_0}{h}\right), \tag{35}$$

then the requirement is that $P(-1) = 0$, $P(1) = 1$, $P'(-1) = 0$ and $P'(1) = 0$. These conditions uniquely define $P(x)$

$$P(x) = \tfrac{1}{4}(2 + 3x - x^3). \tag{36}$$

The truncated potential $V_{R_0}$ is defined as

$$V_{R_0} = \begin{cases} V(R(r)) = V(r), & r < R_0 - h \\ 0, & r \geq R_0 - h \end{cases} \tag{37}$$

We reiterate that by zeroing the potential on the complex portion of the contour, we eliminate any numerical difficulties associated with a less than exponential fall off of the potential at large distances, but have no measurable effect on the cross section.

We do not expect this remedy to come without a price. It's obvious that the basis set one chooses must have elements that extend beyond the complex turning point $R_0$; if not, the eigenvalues of $\bar{H}_\theta$ would effectively be real and Eq. (29) would not yield a sensible result. Even for a short-ranged potential then, we expect that a larger number of

TABLE I. Phase shift for $s$-wave scattering by an exponential potential. $N$ refers to the number of Laguerre-type functions used in the calculation. Results are given for both uniform complex scaling and smooth exterior scaling. See text for basis set and contour parameters.

| $N$ | Uniform | Smooth Exterior |
|---|---|---|
| | $k = 0.15$ | |
| 5 | −0.898 511 72 | −0.000 003 17 |
| 10 | −1.046 153 20 | 0.548 948 06 |
| 15 | −1.058 928 49 | −0.950 252 63 |
| 20 | −1.047 232 52 | −1.027 465 88 |
| 25 | −1.051 195 81 | −1.062 783 68 |
| 30 | −1.050 256 94 | −1.046 716 28 |
| 35 | −1.050 417 02 | −1.051 224 59 |
| 40 | −1.050 403 38 | −1.050 281 54 |
| 45 | −1.050 400 37 | −1.050 404 85 |
| 50 | −1.050 402 26 | −1.050 406 59 |
| 55 | −1.050 401 68 | −1.050 400 28 |
| 60 | −1.050 401 80 | −1.050 402 73 |
| | $k = 0.35$ | |
| 5 | 1.423 933 79 | 0.000 008 38 |
| 10 | 1.460 337 20 | 0.212 813 71 |
| 15 | 1.461 222 77 | 1.436 323 77 |
| 20 | 1.461 247 16 | 1.455 724 39 |
| 25 | 1.461 247 57 | 1.461 076 10 |
| 30 | 1.461 247 56 | 1.461 245 73 |
| 35 | 1.461 247 56 | 1.461 248 05 |
| 40 | 1.461 247 56 | 1.461 248 37 |
| | $k = 0.35$ | |
| 45 | 1.461 247 56 | 1.461 248 45 |
| 50 | 1.461 247 56 | 1.461 247 59 |
| 55 | 1.461 247 56 | 1.461 247 64 |
| 60 | 1.461 247 56 | 1.461 247 59 |
| | $k = 0.55$ | |
| 5 | 1.155 837 18 | −0.000 027 24 |
| 10 | 1.144 127 89 | 0.226 360 78 |
| 15 | 1.144 235 25 | 0.922 345 22 |
| 20 | 1.144 234 35 | 1.141 723 79 |
| 25 | 1.144 234 36 | 1.142 999 29 |
| 30 | 1.144 234 36 | 1.144 086 07 |
| 35 | 1.144 234 36 | 1.144 226 53 |
| 40 | 1.144 234 36 | 1.144 232 62 |
| 45 | 1.144 234 36 | 1.144 232 18 |
| 50 | 1.144 234 36 | 1.144 234 34 |
| 55 | 1.144 234 36 | 1.144 234 16 |
| 60 | 1.144 234 36 | 1.144 234 22 |

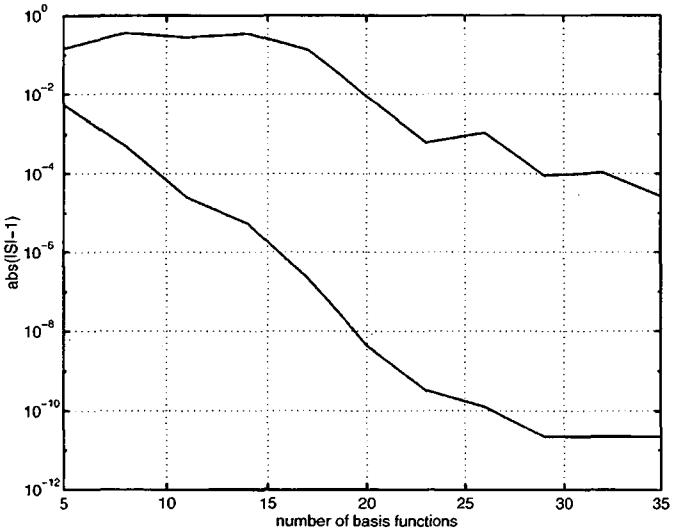


FIG. 1. Unitarity of the calculated $S$ matrix ($S \equiv e^{2i\delta}$) for $s$-wave scattering by an exponential potential at $k=0.55$. Upper curve is for smooth scaling; lower curve is for exterior scaling.

functions will be required to achieve a given level of accuracy with exterior scaling than with uniform scaling and that the number of functions required will grow as $R_0$ increases.

We can recover Simon's original exterior complex scaling contour by letting $h \to 0$ in Eq. (34), in which case $q$ changes discontinuously at $R_0$. Equation (20b) can still be used to define the kinetic-energy matrix, but analytic basis functions will not give uniform convergence with this prescription since the derivative of the wave function (with respect to $r$) is discontinuous at $R_0$. However, the cusp discontinuity in the wave function at the point $R_0$ that occurs with sharp exterior scaling can be accommodated by using a nonanalytic set of basis functions that are only defined on finite intervals. The continuous variable $r$ is replaced by a grid of nodes $0<r_1<r_2<\cdots<r_n<\infty$. Finite element basis functions $\zeta_{i,m}(r)$ are defined to be identically zero outside a given interval

$$\zeta_{i,m}(r)=0 \quad r \notin [r_i, r_{i+1}], \quad i=1,\ldots,n. \tag{38}$$

We use the label $m$ to indicate the boundary conditions imposed on the basis functions at the nodes, for example, zero or unity at the right or left end of the interval. The finite element functions are then combined into a smaller set of continuous basis functions on which the Hamiltonian is projected. To accommodate exterior scaling, we simply require the point $R_0$ to coincide with one of the nodes. To construct the required Hamiltonian matrix elements, we have to consider terms of the form

$$\int_0^\infty \zeta_{i,m}(r) H(R(r)) \zeta_{j,n}(r) q(r) dr$$

$$= \delta_{i,j} \int_{r_i}^{r_{i+1}} \zeta_{i,m}(r) H(R(r)) \zeta_{i,n}(r) \frac{dR}{dr} dr, \tag{39}$$

where, by construction, the point $R_0$ never lies *within* the interval $[r_i, r_{i+1}]$ and, hence, $R(r)$ is always smooth over the integration range. To underscore the fact that the finite element basis functions depend explicitly on the interval boundaries, we write them as $\zeta_{i,j}(r) \equiv f_j(r, r_i, r_{i+1})$. In our implementation of the method, we used Hermite interpolating polynomials $f_j(r, r_i, r_{i+1})$, which are uniquely defined on the interval $[r_i, r_{i+1}]$ from the conditions

$$\frac{d^k}{dr^k} f_j(r, r_i, r_{i+1}) = \delta_{j,k}, \quad r=r_i,$$

$$\frac{d^k}{dr^k} f_j(r, r_i, r_{i+1}) = 0, \quad r=r_{i+1}. \tag{40}$$

For these functions, there is a simple proportionality between $f_j(r, r_i, r_{i+1})$ and $f_j(R(r), R(r_i), R(r_{i+1}))$, where $R(r)$ is any linear function of $r$. Since the exterior scaling contour is a linear transformation on $r$, we can thus write

$$\int_0^\infty \zeta_{i,m}(r) H(R(r)) \zeta_{j,n}(r) q(r) dr \propto \delta_{i,j}$$

$$\times \int_{R(r_i)}^{R(r_{i+1})} f_m(R(r), R(r_i), R(r_{i+1}))$$

$$\times H(R(r)) f_n((r), R(r_i), R(r_{i+1})) dR. \tag{41}$$

This relation is remarkable for two reasons. Firstly, it shows that the finite elements naturally scale onto the rotated contour and thus can handle any step discontinuity in the wave function at the point $R_0$. Moreover, if analytic forms are available for the matrix elements for real intervals, then the right-hand side of Eq. (41) shows that those same formulas, evaluated for complex nodal points, give the correct values for the matrix elements of the Hamiltonian on the complex part of the contour. This would not be true if the turning point $R_0$ fell between two nodes. It is important to bear in mind that the identity expressed in Eq. (41) does not in any sense represent a contour distortion of the integral defined in Eq. (39).

## V. EXAMPLES

In this section we will illustrate some of the ideas we have outlined with several numerical examples. We will first report the results of calculations using analytic basis functions on a smoothly scaled contour. To examine questions of convergence, it is convenient to work with a set of $L^2$ functions that can be systematically increased toward completeness without running into problems of numerical linear dependence. We chose the set of functions

$$\chi_{n,\lambda}(r)=\frac{\lambda^{3/2}}{[(n+1)(n+2)]^{1/2}}\,re^{-\lambda r/2}L_n^2(\lambda r), \tag{42}$$

where $L_n^2(\lambda r)$ is an associated Laguerre polynomial. These functions are orthonormal on $[0,\infty]$ and give simple analytic expressions for matrix elements of the $s$-wave kinetic energy

$$T_{m,n}\equiv -\tfrac{1}{2}\int_0^\infty \chi_{m,\lambda}(r)\frac{d^2}{dr^2}\chi_{n,\lambda}(r)dr$$
$$=\lambda^2\left[-\delta_{m,n}/8+\frac{(2m^3+9m^2+13m+6)}{12\sqrt{(n+1)(n+2)(m+1)(m+2)}}\right]. \tag{43}$$

These analytic formulas can even be used to simplify the evaluation of matrix elements carried out on a complex contour where numerical quadrature is required, i.e., where we use

$$\int \chi_{m,\lambda}(r)H(R(r))\chi_{n,\lambda}(r)q(r)dr$$
$$\approx\sum_i \chi_{m,\lambda}(r_i)H(R(r_i))\chi_{n,\lambda}(r_i)q(r_i)w_i. \tag{44}$$

We can make use of the fact that $q(r)=e^{i\phi}$ for $r>R_0+h$ to simplify evaluation of the overlap and kinetic-energy matrix elements. In the case of the overlap matrix, for example, we write

$$\int_0^\infty \chi_{m,\lambda}(r)\chi_{n,\lambda}(r)q(r)dr$$
$$=\int_0^{R_0+h}\chi_{m\lambda}(r)\chi_{n,\lambda}(r)q(r)dr+e^{i\phi}\left[\int_0^\infty \chi_{m,\lambda}(r)\right.$$
$$\left.\times\chi_{n,\lambda}(r)dr-\int_0^{R_0+h}\chi_{m,\lambda}(r)\chi_{n,\lambda}(r)dr\right]$$
$$\approx e^{i\phi}\delta_{m,n}+\sum_j \chi_{m,\lambda}(r_j)\chi_{n,\lambda}(r_j)(q(r_j)-e^{i\phi})w_j, \tag{45}$$

where the quadrature points only cover the interval $[0,R_0+h]$.

We first considered $s$-wave scattering from the short-range potential

$$V(r)=-e^{-r} \tag{46}$$

TABLE II. Phase shift for $s$-wave scattering by truncated long range potential. $N$ refers to the number of Laguerre-type functions used in a smooth exterior scaling calculation. See text for basis set and contour parameters.

| $N$ | $R_0=25$ | $R_0=35$ |
|---|---|---|
| | $k=0.15$ | |
| 10 | −0.010 800 94 | −0.000 000 15 |
| 20 | −0.069 561 68 | −0.164 917 53 |
| 30 | −0.060 820 42 | −0.061 410 67 |
| 40 | −0.060 917 40 | −0.060 926 53 |
| 50 | −0.060 944 40 | −0.061 025 23 |
| 60 | −0.060 945 59 | −0.061 030 83 |
| 70 | −0.060 945 56 | −0.061 030 78 |
| 80 | −0.060 945 58 | −0.061 030 78 |
| 90 | −0.060 945 59 | −0.061 030 79 |
| 100 | −0.060 945 59 | −0.061 030 78 |
| | $k=0.35$ | |
| 10 | −0.000 384 21 | −0.000 000 01 |
| 20 | −0.099 657 09 | −0.037 669 36 |
| 30 | −0.100 319 07 | −0.100 177 26 |
| 40 | −0.100 336 19 | −0.100 404 43 |
| 50 | −0.100 336 28 | −0.100 411 17 |
| 60 | −0.100 336 39 | −0.100 410 98 |
| 70 | −0.100 336 48 | −0.100 410 97 |
| 80 | −0.100 336 48 | −0.100 410 97 |
| 90 | −0.100 336 48 | −0.100 411 06 |
| 100 | −0.100 336 49 | −0.100 411 09 |
| | $k=0.55$ | |
| 10 | −0.000 361 34 | −0.000 000 01 |
| 20 | −0.132 563 05 | −0.043 013 91 |
| 30 | −0.118 845 09 | −0.114 737 08 |
| 40 | −0.118 665 69 | −0.118 511 86 |
| 50 | −0.118 658 89 | −0.118 669 29 |
| 60 | −0.118 658 68 | −0.118 689 69 |
| 70 | −0.118 658 54 | −0.118 691 13 |
| 80 | −0.118 658 59 | −0.118 691 33 |
| 90 | −0.118 658 57 | −0.118 691 37 |
| 100 | −0.118 658 56 | −0.118 691 29 |

and compared the results obtained from uniform complex scaling, i.e., $H(r)\to H(re^{i\phi})$, with smooth exterior scaling $H(r)\to H(R(r))$. The contour used the polynomial switching function described in Sec. IV. For these calculations, we chose $R_0=20.0$ and $h=4.0$. The Laguerre scale factor $\lambda$ was set to 2.0 and the rotation angle was 30° for both sets of calculations. Table I shows the behavior of the $s$-wave phase shift (defined here as the phase of the calculated $T$ matrix) for several values of $k$. The convergence is faster with uniform scaling than with smooth exterior scaling, as we conjectured, because with smooth exterior scaling one first needs to span the region from the origin to $R_0$ before one begins to see convergence. This can be seen in Fig. 1, which compares uniform and smooth exterior scaling for $k=0.55$. The measure of convergence for this comparison is the unitarity of the $S$ matrix ($S=e^{2i\delta}$), which is computed from the $T$ matrix as $S=1+2iT$.

The next case we consider is $s$-wave scattering from the long-range potential

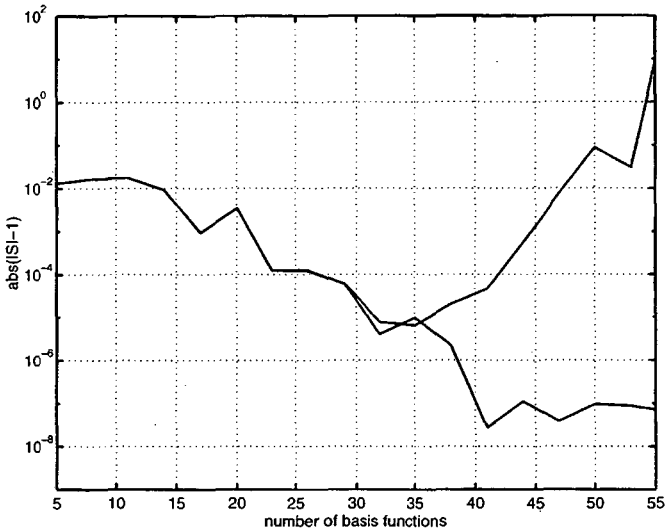


FIG. 2. Unitarity of the calculated $S$ matrix ($S \equiv e^{2i\delta}$) for $s$-wave scattering by a long-range potential at $k=0.55$. The divergent upper curve is for a potential which is not truncated on the complex part of the integration contour.

$$V(r)=\frac{1}{(1+r)^4}, \tag{47}$$

for which uniform complex scaling diverges. We again studied convergence with the smooth exterior scaling transformation, this time zeroing the potential beyond $R_0-h$, where the contour begins to turn off the real axis. Results are shown in Table II for several $k$ values and two different values of $R_0$. All other parameters of the contour and basis are the same as in the preceding case. The rate of convergence is similar to what was found with the exponential potential, but the converged phase shifts show a slight dependence on $R_0$, reflecting their dependence on the point beyond which the potential is truncated. For comparison, we also show, in Fig. 2, the results of a calculation in which the long-range potential is not truncated. It is noteworthy that calculations using the untruncated potential can provide useful results for a range of basis set values, before they ultimately begin to diverge.

We also implemented sharp exterior scaling in a finite element basis of fifth-order Hermite interpolating polynomials. In each interval $[r_i, r_{i+1}]$, we can uniquely define six independent polynomials $P_{j,i}(r)$ and $Q_{j,i}(r)$, $j=0,1,2$ from the conditions

$$\begin{matrix} \dfrac{d^k}{dr^k} P_{j,i}(r_i)=\delta_{j,k} \\ \dfrac{d^k}{dr^k} P_{j,i}(r_{i+1})=0 \end{matrix} \quad , \quad j,k=0,1,2$$

$$\begin{matrix} \dfrac{d^k}{dr^k} Q_{j,i}(r_{i+1})=\delta_{j,k} \\ \dfrac{d^k}{dr^k} Q_{j,i}(r_i)=0 \end{matrix} \quad , \quad j,k=0,1,2 \tag{48}$$

The explicit formulas for the $P_{j,i}$ are

$$P_{0,i}(r)=\left(\frac{r-r_{i+1}}{r_i-r_{i+1}}\right)^3\left[6\left(\frac{r-r_{i+1}}{r_i-r_{i+1}}\right)^2-15\left(\frac{r-r_{i+1}}{r_i-r_{i+1}}\right)+10\right],$$

$$P_{1,i}(r)=(r_{i+1}-r_i)\left(\frac{r-r_{i+1}}{r_i-r_{i+1}}\right)^2\left[3\left(\frac{r-r_{i+1}}{r_i-r_{i+1}}\right)^2-7\left(\frac{r-r_{i+1}}{r_i-r_{i+1}}\right)+4\right],$$

$$P_{2,i}(r)=\frac{1}{2}(r_i-r_{i+1})^2\left(\frac{r-r_{i+1}}{r_i-r_{i+1}}\right)^3\left[\left(\frac{r-r_{i+1}}{r_i-r_{i+1}}\right)-1\right], \tag{49}$$

for $r_i \le r \le r_{i+1}$ and zero elsewhere. The functions $Q_{j,i}$ are obtained by interchanging $r_i$ and $r_{i+1}$ in the formulas for $P_{j,i}$.

We can use these polynomials to define three basis functions at each node $r_i$ which span the interval $[r_{i-1}, r_{i+1}]$, and have vanishing value, first and second derivative at the end points. The basis functions are defined as

$$\chi_{j,i}(r) \equiv (P_{j,i}(r)+Q_{j,i-1}(r)) \tag{50}$$

and are plotted in Fig. 3. It is obvious from Eq. (49) that the basis functions defined in Eq. (50) scale onto the contour as described in Sec. IV. In particular, at the point $r_i=R_0$, we see that

$$\lim_{\varepsilon\to 0}(\chi_{j,i}(R_0+\varepsilon)=(e^{i\phi})^j\chi_{j,i}(R_0-\varepsilon)). \tag{51}$$

Thus the function $\chi_{0,i}$ guarantees continuity of the wave function at $r_i=R_0$, while $\chi_{1,i}$ and $\chi_{2,i}$ impose the proper discontinuity conditions on the first and second derivatives, respectively. To impose boundary conditions that the wave function vanish at the origin and last grid point, we simply omit the functions $\chi_{0,1}$ and $\chi_{0,N}$ and remove $P_{j,1}$ and $Q_{j,N}$, $j=1,2$ from the definition of the basis functions.

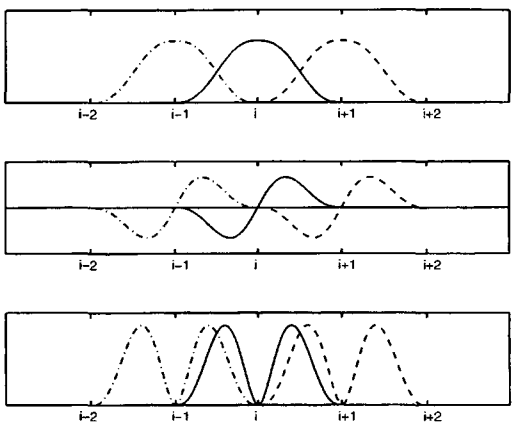


FIG. 3. Basis functions for finite element calculations. Upper panel: $\chi_{j,0}$; center panel: $\chi_{j,1}$; lower panel: $\chi_{j,2}$. See text for definition of the functions.

The exterior scaled finite element method was also applied to the long-range potential problem previously considered. For these calculations, the grid points were evenly spaced from 0 to $r_N=100$ with $R_0$ fixed at 25 and the rotation angle was set at 20°. Once again, the potential was set equal to zero along the complex portion of the contour. Table III shows the behavior of the computed phase shifts at several energies as a function of the grid spacing. Evidently, the method converges very rapidly.

TABLE III. Phase shift for $s$-wave scattering by truncated long-range potential. Results from exterior scaling calculations using finite elements.

| Nodal spacing | $k=0.35$ | $k=0.55$ |
|---|---|---|
| 12.5 | −0.099 959 82 | −0.104 554 62 |
| 5.0 | −0.100 403 13 | −0.118 680 40 |
| 2.0 | −0.100 394 47 | −0.118 675 91 |
| 1.0 | −0.100 391 89 | −0.118 673 24 |
| 0.5 | −0.100 396 82 | −0.118 673 16 |
| 0.25 | −0.100 396 82 | −0.118 673 16 |

## VII. DISCUSSION

We have shown that, with exterior complex scaling, we can answer the question posed by the title of this paper in the affirmative. Exterior complex scaling was originally introduced as a generalization of uniform complex scaling to deal with potentials that suffered interior nonanalyticities, but were analytic outside a sphere of finite radius. What we have shown is that by making this radius large enough so that the potential can be truncated at this distance without physical consequence, then exterior scaling can be implemented in an $L^2$ basis and provides a method for solving the full scattering problem without explicitly enforcing asymptotic boundary conditions, even in cases involving long-range potentials where uniform scaling diverges. For analytic basis functions, we use smooth exterior scaling to assure uniform convergence; for sharp exterior scaling, finite element basis sets can be employed. These developments allow the method to be applied to the kinds of nonresonant scattering problems encountered in atomic and molecular physics. The fact that the interaction region is represented in real coordinates also obviates the need for the mixtures of real and complex basis functions that have previously been used to treat many-electron systems. We can also show that the present development allows us to make contact with other formulations of scattering in which cross sections are evaluated by calculating the flux through a surface outside the interaction region. This will be the subject of another study.

## ACKNOWLEDGMENTS

This work was performed under the auspices of the U.S. Department of Energy by the Lawrence Livermore National Laboratory under Contract No. W-7405-Eng-48. Computer time was supplied by the National Energy Research Scientific Computing Center.

[1] T. Regge, Nuovo Cimento **14**, 951 (1959); **18**, 947 (1960).
[2] J. Nuttall and H. L. Cohen, Phys. Rev. **188**, 1542 (1969).
[3] T. N. Rescigno and W. P. Reinhardt, Phys. Rev. A **8**, 2828 (1973); **10**, 158 (1974).
[4] G. Doolen, J. Nuttall, and R. Stagat, Phys. Rev. A **10**, 1612 (1974).
[5] W. P. Reinhardt, Ann. Rev. Phys. Chem. **33**, 223 (1882).
[6] C. W. McCurdy, in *Resonances in Electron-Molecule Scattering, van der Waal Complexes and Reactive Chemical Dynamics*, edited by D. G. Truhlar (American Chemical Society, Washington, D.C., 1984), Vol. 263, p. 17.
[7] B. R. Johnson and W. P. Reinhardt, Phys. Rev. A **28**, 1930 (1983); **29**, 2933 (1984).
[8] T. N. Rescigno and C. W. McCurdy, Phys. Rev. A **31**, 624 (1985); Chem. Phys. Lett. **140**, 232 (1987).
[9] T. N. Rescigno and V. McKoy, Phys. Rev. A **12**, 522 (1975).
[10] C. W. McCurdy and T. N. Rescigno, Phys. Rev. A **21**, 1499 (1980).
[11] T. N. Rescigno, Phys. Rev. A **31**, 607 (1984).
[12] S. Yabushita, C. W. McCurdy, and T. N. Rescigno, Phys. Rev. A **36** 3146 (1987).
[13] R. T. Baumel, M. C. Crocker, and J. Nuttall, Phys. Rev. A **12**, 486 (1975).
[14] B. Simon, Phys. Lett. A **71**, 211 (1979).
[15] C. W. McCurdy and T. N. Rescigno, Phys. Rev. Lett. **41**, 14364 (1978).
[16] J. Turner and C. W. McCurdy, Chem. Phys. **71**, 127 (1982); C. W. McCurdy, C. K. Stroud, and M. K. Wisinski, Phys. Rev. A **43**, 5980 (1991).
[17] M. Rittby, N. Elander, and E. Brändas, Int. J. Quantum Chem. **23**, 865 (1983); Chem. Phys. **87**, 55 (1984).
[18] R. Lefebvre, J. Phys. Chem. **88**, 4839 (1984).

[19] N. Lipkin, N. Moiseyev, and E. Brändas, Phys. Rev. A **40**, 549 (1989).
[20] N. Rom, E. Engdahl, and N. Moiseyev, J. Chem. Phys. **93**, 3413 (1990).
[21] A. Scrinzi and N. Elander, J. Chem. Phys. **98**, 3866 (1993).
[22] E. Balslev and J. M. Combes, Commun. Math. Phys. **22**, 280 (1971); B. Simon, Commun. Math. Phys. **27**, 1 (1972).
[23] T. N. Rescigno, C. W. McCurdy, and A. E. Orel, Phys. Rev. A **17**, 1931 (1978).
[24] B. R. Junker, Adv. At. Mol. Phys. **18**, 207 (1982).
[25] Although it has become customary to cite the work of Simon when discussing exterior scaling, the idea of using a path which is part real and part complex had been suggested earlier. Gyarmati and Vertse [Nucl. Phys. A **160**, 523 (1971)] had suggested such a path in connection with the normalization of resonance wave functions for charged systems, and similar ideas are discussed in J. Taylor, *Scattering Theory* (Wiley, New York, 1972), pp. 221 and 222.
[26] P. B. Kurasov, A. Scrinzi, and N. Elander, Phys. Rev. A **49**, 5095 (1994).
[27] C. W. McCurdy, Phys. Rev. A **21**, 464 (1980).
[28] This discussion assumes that the potential falls off more rapidly than $|1/r|$ at infinity.

# Appendix C

# Finite Difference Formulas

Using finite difference approximations of derivatives has the advantage of producing very sparse matrices whose matrix elements are trivial to evaluate. Additionally, finite difference is one of the few numerical methods than can handle a non-analytic exterior complex scaling contour such as the one defined in Equation 3.12. Seven-point finite difference approximations of the second derivative give significantly more accurate solutions than the standard three-point formulas, particularly when multiple grid spacings and/or exterior complex scaling are used. Formulas for three, five and seven-point finite difference approximations are listed in this appendix. Derivations of just the three-point formulas are presented to illustrate the general procedure for generating finite difference formulas and applying them to exterior complex scaling.

## C.1 Uniform grid spacing

Consider an evenly spaced grid with grid points $x_n \equiv nh$ where $h$ is the spacing between grid points. Let $f_n$ be the values of some function $f(x)$ such that $f_n = f(x_n)$. Now suppose we wish to approximate $f_n^{ii} \equiv \frac{d^2}{dx^2} f(x)|_{x=x_n}$, the second derivative of $f$ at the point $x_n$. The values of $f(x)$ at the grid points on either side of $x_n$ can be expressed with a Taylor series in terms of $f(x)$ and its derivatives evaluated at $x_n$.

$$f_{n\pm1} = f_n \pm h f_n^i + \frac{1}{2}h^2 f_n^{ii} \pm \frac{1}{6}h^3 f_n^{iii} + \frac{1}{24}h^4 f_n^{iv} + ... \tag{C.1}$$

When the Taylor series expansions of $f_{n+1}$ and $f_{n-1}$ are added together the first derivative terms cancel.

$$f_{n-1} + f_{n+1} = 2f_n + h^2 f_n^{ii} + \frac{1}{12}h^4 f_n^{iv} + ... \tag{C.2}$$

Equation C.2 can be rearranged to give a formula for $f_n^{ii}$ that uses the function value at three grid points ($f_{n-1}$, $f_n$ and $f_{n+1}$) as well as higher derivatives evaluated at $x_n$.

$$f_n^{ii} = \frac{1}{h^2}(-2f_n + f_{n+1}) - \frac{1}{12}h^2 f_n^{iv} + ... \tag{C.3}$$

| $h^2 f_n^{ii} \approx$ | error term |
|---|---|
| $f_{n-1} - 2f_n + f_{n+1}$ | $\frac{1}{12}h^2 f_n^{iv}$ |
| $-\frac{1}{12}f_{n-2} + \frac{4}{3}f_{n-1} - \frac{5}{2}f_n + \frac{4}{3}f_{n+1} - \frac{1}{12}f_{n+2}$ | $\frac{1}{90}h^4 f_n^{vi}$ |
| $\frac{11}{12}f_{n-1} - \frac{5}{3}f_n + \frac{1}{2}f_{n+1} + \frac{1}{3}f_{n+2} - \frac{1}{12}f_{n+3}$ | $\frac{1}{12}h^3 f_n^{v}$ |
| $\frac{1}{90}f_{n-3} - \frac{3}{20}f_{n-2} + \frac{3}{2}f_{n-1} - \frac{49}{18}f_n + \frac{3}{2}f_{n+1} - \frac{3}{20}f_{n+2} + \frac{1}{90}f_{n+3}$ | $\frac{69}{25200}h^6 f_n^{viii}$ |

Table C.1: Finite difference formulas for evenly spaced grids.

Equation C.3 is a three-point formula for the second derivative with a leading error term that is second order in the grid spacing $h$. By following the same procedure, but using more grid points on either side of $x_n$, we can derive more accurate formulas for the second derivative. A five-point formula with fourth order error and a seven-point formula with sixth order error are listed in Table C.1. An "asymmetric" five-point formula is also given in Table C.1. This formula is used for grid points adjacent to the boundary *i.e.*, $n = 1$, (see Figure 3.3) and approximates the second derivative to third order in the grid spacing $h$.

## C.2 Two different grid spacings

The formulas in Table C.1 require that the grid be evenly spaced. In practice, we may wish to use different spacings in different regions of the grid. Suppose that a grid consists of two different grid spacings $g$ and $h$ with a uniform spacing of $g$ to the left of the point $x_p$ and a uniform spacing of $h$ to the right of the point $x_p$. For any grid point $x_n$ where $n \neq p$ we can use the formula in Equation C.3 with grid spacing $g$ for $n < p$ and grid spacing $h$ for $n > p$. However, we need a new formula to approximate the second derivative at the interface point $x_p$.

Consider the Taylor series expansions for $f_{p+1}$ and $f_{p-1}$ about the point $x_p$.

$$\begin{aligned} f_{p+1} &= f_p + hf_p^i + \frac{1}{2}h^2 f_p^{ii} + \frac{1}{6}h^3 f_p^{iii} + \ldots \\ f_{p-1} &= f_p - gf_p^i + \frac{1}{2}g^2 f_p^{ii} - \frac{1}{6}g^3 f_p^{iii} + \ldots \end{aligned} \tag{C.4}$$

We now add these two formulas together after multiplying each by the appropriate grid spacing such that the first derivative terms cancel.

$$hf_{p-1} + gf_{p+1} = (g+h)f_p + \frac{1}{2}gh(g+h)f_p^{ii} - \frac{1}{6}gh(g^2 - h^2)f_p^{iii} + \ldots \tag{C.5}$$

As before we rearrange to get a formula for $f_p^{ii}$. Now the first nonzero higher derivative

| | $n = p-1$ | $n = p$ | $n = p+1$ |
|---|---|---|---|
| $f_{n-2}$ | $\frac{-1}{3g(3g+h)}$ | $\frac{h(2h-3g)}{2g^2(2g+h)(g+h)}$ | $\frac{-2h^2}{g(g+h)(g+2h)(g+3h)}$ |
| $f_{n-1}$ | $\frac{3g+h}{g^2(2g+h)}$ | $\frac{4h(3g-h)}{g^2(g+2h)(g+h)}$ | $\frac{h+3g}{3gh^2}$ |
| $f_n$ | $\frac{-(3g+2h)}{g^2(g+h)}$ | $\frac{2h^2+2g^2-9gh}{2g^2h^2}$ | $\frac{-(3h+2g)}{h^2(g+h)}$ |
| $f_{n+1}$ | $\frac{g+3h}{3g^2h}$ | $\frac{4g(3h-g)}{h^2(h+2g)(g+h)}$ | $\frac{3h+g}{h^2(2h+g)}$ |
| $f_{n+2}$ | $\frac{-2g^2}{h(g+h)(h+2g)(h+3g)}$ | $\frac{g(2g-3h)}{2h^2(2h+g)(g+h)}$ | $\frac{-1}{3h(3h+g)}$ |
| error | $\frac{1}{60}g^2hf^v_{n-1}$ | $\frac{1}{10}gh(g-h)f^v_n$ | $\frac{1}{60}h^2(g-h)f^v_{n+1}$ |

Table C.2: Five-point finite difference formulas for the "interface" between two different grid spacings. Special formulas are needed for the second derivative at the interface point $x_p$ as well as the point on either side. The three columns of the table give the coefficients needed to approximate $f^{ii}_n$ for $n = p-1$, $n = p$ and $n = p+1$.

term is $f^{iii}_n$ rather than $f^{iv}_n$ so the leading error term is *first* order in $(g-h)$.

$$f^{ii}_p = \frac{2}{gh(g+h)}\left(hf_{p-1} - (g+h)f_p + gf_{p+1}\right) + \frac{1}{6}(g-h)f^{iii}_p + \ldots \qquad \text{(C.6)}$$

It is generally true that finite difference formulas that straddle two regions of different grid spacings will be less accurate by one order than their uniform grid counterparts. For the three-point approximations we need a special formula only for the derivative at $x_p$. The five and seven-point approximations sample from a wider area so they require special formulas for one and two points, respectively, on either side of the interface point $x_p$. Special formulas for five-point approximations near an interface are listed in Table C.2 and the seven-point formulas are listed in Table C.3.

## C.3 Application to exterior complex scaling

Applying the finite difference formulas to exterior complex scaling is straightforward. The same formulas are used but grid spacings in the region where the coordinates are complex are multiplied by $e^{i\eta}$ where $\eta$ is the complex scaling angle. In the cases where the finite difference formulas straddle the complex scaling point $R_0$ some of the grid "spacings" will be real and some will be complex. This means that even for an evenly spaced grid the specialized finite difference formulas in Equation C.6 or in Tables C.2 and C.3 are necessary for implementing exterior complex scaling. Finite difference is well-suited to handle the non-analyticity of the exterior complex scaling contour provided that $R_0$ is one of the grid points. The transition from a real to a complex grid at $R_0$ does mean that the error in the finite difference formulas

Table C.3: Seven-point finite difference formulas for two grid spacings

| | $n = p-2$ | $n = p-1$ | $n = p$ | $n = p+1$ | $n = p+2$ |
|---|---|---|---|---|---|
| $f_{n-3}$ | $\frac{1}{15g(5g+h)}$ | $\frac{3g^2+3gh-2h^2}{24g^2(2g+h)(4g+h)}$ | $\frac{2(11g-9h)h^2}{9g^2(g+h)(3g+h)(3g+2h)}$ | $\frac{h^3(5g-h)}{4g^2(g+h)(2g+h)(g+2h)(3h+2g)}$ | $\frac{8h^4}{g(g+h)(2h+g)(3h+g)(4h+g)(5h+g)}$ |
| $f_{n-2}$ | $\frac{-(8g+h)}{12g^2(4g+h)}$ | $\frac{-(5g^2+6gh-2h^2)}{3g^2(3g+h)(3g+2h)}$ | $\frac{-3(11g-8h)h^2}{2g^2(g+h)(2g+h)(2g+3h)}$ | $\frac{-2h^3(10g-h)}{g^2(g+h)(2h+g)(3h+g)(4h+g)}$ | $\frac{-(4h+5g)}{60gh^2}$ |
| $f_{n-1}$ | $\frac{2(7g+2h)}{3g^2(3g+h)}$ | $\frac{13g^2+21gh+2h^2}{4g^2(g+h)(2g+h)}$ | $\frac{6(11g-5h)h^2}{g^2(g+h)(g+2h)(g+3h)}$ | $\frac{22g^2+15gh-h^2}{24g^2h^2}$ | $\frac{5h+4g}{3h^2(g+h)}$ |
| $f_n$ | $\frac{-(34g+15h)}{6g^2(2g+h)}$ | $\frac{-(9g^2+30gh+10h^2)}{3g^2(g+h)(g+2h)}$ | $\frac{36g^2-121gh+36h^2}{18g^2h^2}$ | $\frac{-(9h^2+30gh+10g^2)}{3h^2(g+h)(h+2g)}$ | $\frac{-(34h+15g)}{6h^2(2h+g)}$ |
| $f_{n+1}$ | $\frac{5g+4h}{3g^2(g+h)}$ | $\frac{22h^2+15hg-g^2}{24g^2h^2}$ | $\frac{6g^2(11h-5g)}{h^2(g+h)(2g+h)(3g+h)}$ | $\frac{13h^2+21gh+2g^2}{4h^2(g+h)(2h+g)}$ | $\frac{2(7h+2g)}{3h^2(3h+g)}$ |
| $f_{n+2}$ | $\frac{-(4g+5h)}{60g^2h}$ | $\frac{-2g^3(10h-g)}{h^2(g+h)(2g+h)(3g+h)(4g+h)}$ | $\frac{-3g^2(11h-8g)}{2h^2(g+h)(g+2h)(3g+2h)}$ | $\frac{-(5h^2+6gh-2g^2)}{3h^2(3h+g)(3h+2g)}$ | $\frac{-(8h+g)}{12h^2(4h+g)}$ |
| $f_{n+3}$ | $\frac{8g^4}{h(g+h)(2g+h)(3g+h)(4g+h)(5g+h)}$ | $\frac{g^3(5h-g)}{4h^2(g+h)(2g+h)(g+2h)(3g+2h)}$ | $\frac{2g^2(11h-9g)}{9h^2(g+h)(g+3h)(2g+3h)}$ | $\frac{3h^2+3gh-2g^2}{24h^2(2h+g)(4h+g)}$ | $\frac{1}{15h(5h+g)}$ |
| error | $\frac{-1}{630}g^4(g-h)f_n^{vii}$ | $\frac{-1}{2520}g^3(7g+10h)(g-h)f_n^{vii}$ | $\frac{-11}{420}g^2h^2(g-h)f_n^{vii}$ | $\frac{1}{2520}h^3(10g+7h)(h-g)f_n^{vii}$ | $\frac{1}{630}h^4(h-g)f_n^{vii}$ |

Seven-point finite difference formulas for the "interface" between two different grid spacings. Special formulas are needed for the second derivative at the interface point $x_p$ as well as two points on either side. The five columns of the table give the coefficients needed to approximate $f_n^{ii}$ for $n = p \pm 2$, $n = p \pm 1$ and $n = p$.

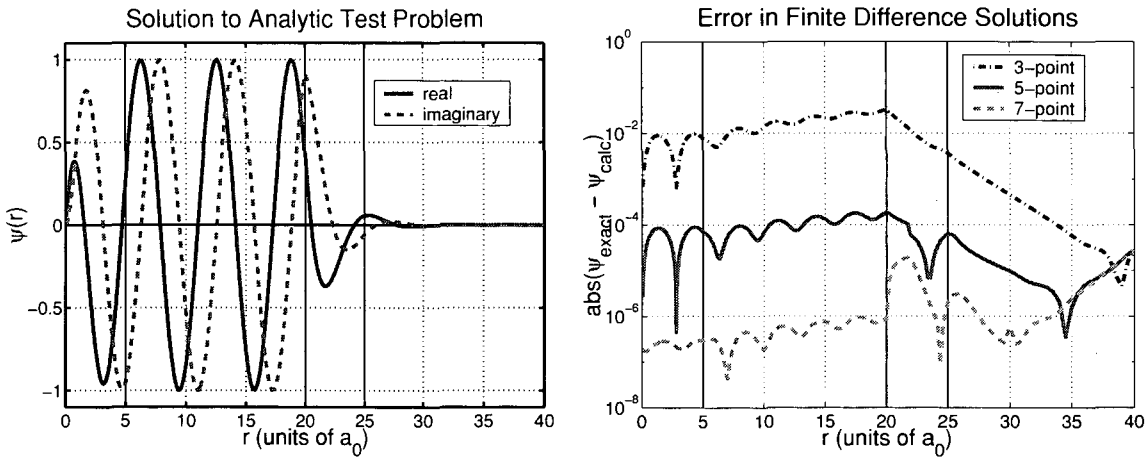


Figure C.1: On the left is the analytic function given in Equation C.7 evaluated on a grid that is complex beyond $R_0 = 20a_0$ with a scaling angle of $30^o$. On the right is the numerical error in wave functions calculated by solving Equation C.8 using 3-point, 5-point and 7-point finite difference formulas. In this example the grid spacing was $0.05a_0$ between $r = 0$ and $r = 5a_0$, $0.2a_0$ between $r = 5a_0$ and $r = 25a_0$, and $0.5a_0$ beyond $r = 25a_0$.

will be larger than for a real, uniformly spaced grid. For this reason, the higher-order seven-point finite difference formulas should be used.

## C.4 Analytic example

We can test finite difference applied to exterior complex scaling by solving an inhomogeneous differential equation that is similar to a one-dimensional scattered wave equation but has a known analytic solution.

$$\psi(r) = \left(1 - e^{-\alpha r}\right) e^{ikr} \tag{C.7}$$

The function defined in Equation C.7 is an outgoing radial wave similar to a scattered wave for one-dimensional potential scattering such as the examples in Appendix A. It is a solution to an inhomogeneous differential equation of the form $\left(\hat{H} - E\right)\psi(r) = \chi(r)$ with an attractive exponential potential.

$$\frac{1}{2}\left(-\frac{d^2}{dr^2} - \alpha^2 e^{-\alpha r} - k^2\right)\psi = \left(\frac{\alpha^2}{2}e^{-\alpha r} - 2i\alpha k\right) e^{-\alpha r} e^{ikr} \tag{C.8}$$

The exact solution to Equation C.8, evaluated on a contour that is complex beyond $R_0 = 20a_0$, is shown in the left panel of Figure C.1. In this example $k = \alpha = 1a_0^{-1}$ and the complex scaling angle is $30^o$. The grid extends to $40a_0$ which is far enough that $\psi$ is effectively zero at the end of the grid.

Most of the grid has a grid spacing of $0.2a_0$ which is sufficient to describe an oscillatory function with this wavelength. A much smaller grid spacing of $0.05a_0$ is

used for small $r$. The smaller grid spacing is unnecessary for this example but it is needed when Coulomb potentials are involved. For large $r$ at some distance beyond the scaling point $R_0$ the wave function is sufficiently damped that representing it accurately is unnecessary so we can use a larger grid spacing of $0.5a_0$ at the large $r$ end of the grid. The numerical errors in the calculated solutions for three, five and seven-point finite difference formulas are shown on the right in Figure C.1. The effect of using higher-order finite difference formulas is clearly evident. In particular, using a higher-order formula makes the calculated solution more accurate on the real part of the grid even if there is little or no improvement in the solution on the complex part of the grid.

# Appendix D

# *LU* Factorization of Sparse Matrices Using SuperLU

The finite difference matrix representations of the Hamiltonian consist mostly of matrix elements that are zero. We can greatly improve the computational efficiency of the methods for solving the scattered wave equation by taking advantage of the sparsity of the matrices. Packed array storage schemes for sparse matrices minimize the amount of memory required to store a sparse matrix. Specialized routines for matrix operations involving sparse matrices minimize the number of required floating point operations. An essential component to the completion of the calculations for this thesis was a software package called SuperLU which solves a matrix equation for a sparse matrix very efficiently by *LU* factorization.

## D.1 Two-dimensional finite difference matrices

Only a small fraction of the matrix elements in the finite different matrix representation of the Hamiltonian are nonzero. The sparsity structure for the two-dimensional Temkin-Poet matrices are shown in Figure D.1. Each row or column corresponds to a particular point on the grid. The same number of grid points is used for both radial coordinates so the dimension of the matrix is $N = n_g^2$ with the wave function represented by an array of $N$ numbers corresponding to the value of the wave function at each grid point. Potentials are represented by matrices whose diagonal matrix elements are the values of the potential at each grid point and whose off-diagonal matrix elements are zero. The finite difference formulas link each grid point to one or more neighboring grid points on all sides.

All of the nonzero off-diagonal elements of the Hamiltonian matrix are due to the finite difference formulas. The number of nonzero elements for any row of the matrix is determined by the number of points used in the two-dimensional finite difference stencil (see Figure 3.3) centered at the grid point corresponding to that row. The low-order finite difference matrix, based on three-point formulas, has at most five nonzero matrix elements on each row and the high-order matrix, based on seven-point formulas, is limited to 13 nonzeros per row. Rows of the matrix that

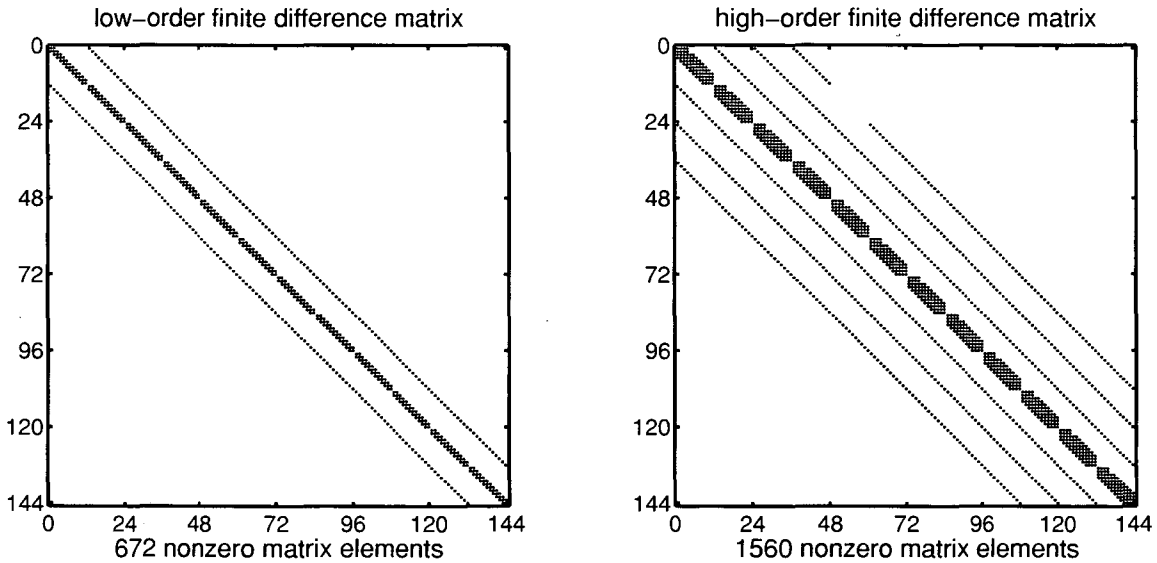


Figure D.1: Sparsity structure of the finite difference matrix representations of the two-dimensional Hamiltonian in the Temkin-Poet model. On the left is the low-order matrix which uses 3-point formulas for the second derivates. On the right is the high-order matrix which uses 7-point formulas. These examples are very small (144 total gridpoints extending only to $2a_0$) so that the basic structure can be seen.

correspond to points near an edge of the grid will have fewer nonzero elemnts. The total number of nonzero matrix elements is given in Equation D.1.

$$\text{number of nonzeros} = \begin{cases} n_g(n_g + 2n_g(2n_g - 2)) & \text{3-point formulas} \\ n_g(n_g + 6n_g(2n_g - 4)) & \text{7-point formulas} \end{cases} \tag{D.1}$$

Both matrices pictured in Figure D.1 have a very particular structure. The two-dimensional grid points are ordered such that the grid points for a fixed $r_2$ are contiguous. Each of the $n_g$ groups of $n_g$ fixed $r_2$ points is ordered from smallest $r_2$ to largest $r_2$. Within each group the points are ordered from smallest $r_1$ to largest $r_1$. Finite difference formulas in $r_1$ connect neighboring points in $r_1$. These fill out the seven inner-most diagonals for the high-order matrix and the three inner-most diagonals for the low-order matrix. Neighboring points in $r_2$ are $n_g$ apart in the matrix ordering so the $r_2$ finite difference formulas form nonzero diagonals at $n_g$ intervals.

The low-order matrix has nonzeros on the three inner diagonals and on the $n_g^{th}$ super and sub-diagonals with an overall bandwidth of $2n_g - 1$. The high-order matrix has nonzeros on the seven inner diagonals and at three super and sub-diagonals at strides of $n_g$ with an overall bandwidth of $7n_g - 1$. The notch visible in the $3n_g^{th}$ super-diagonal is due to using five-point finite difference formulas for grid points that are two points from the edge. There are no "missing" super-diagonals for the grid points right next to the edge because a "lop-sided" five-point formula was used. This same feature exists on the inner diagonals which also have a segmented appearance marking the separations between groups of fixed $r_2$ points.

## D.2 Storing sparse matrices

We substantially reduce the amount of computer memory used to store a sparse matrix by storing only the nonzero matrix elements. A sparse matrix is stored in an array of length $nnz$ where $nnz$ is the number of nonzero matrix elements. The number of nonzero elements scales linearly with the dimension of the matrix $N$ (less than $5N$ for the low-order and $13N$ for the high-order matrices) compared with $N^2$ total matrix elements so the savings in memory increases rapidly with matrix size.

The cost of this savings is that row and column index information for each nonzero matrix element must also be stored. The simplest way to do this would be to also store two arrays of length $nnz$ for the row and column indices of each nonzero matrix element. We can achieve a further savings in memory by using a packed storage scheme. Row indices are still stored in a length $nnz$ array, but column index information is stored implicitly by requiring that all nonzero matrix elements from a particular column be stored together. An array of length $N+1$ denotes the beginning and end of each column's group of matrix elements. A simplistic algorithm for storing a matrix in this way is provided on page 111. That algorithm is for illustrative purposes only and should never be used in practice because it is extremely inefficient.

The sparse matrix storage scheme also provides for a significant savings in computer time by reducing the number of floating point calculations required to perform matrix operations. For instance, a matrix-vector multiply involving a dense matrix of order $N$ requires $N^2$ individual multiplications. If the matrix is sparse then we can eliminate all of the mulitplications for matrix elements that are zero so that only $nnz$ individual multiplications are required. In cases like the finite difference matrices where the number of nonzero elements per row is fixed the cost of matrix-vector multiplies is linear rather than quadratic in $N$. This fact is very important when iterative methods are used for solving large matrix equations.

## D.3 *LU* factorization of sparse matrices

Gaussian elimination is the canonical method for solving a matrix equation of the form $\mathbf{Ax} = \mathtt{b}$. The majority of the operations in Gaussian elimination depend only on the matrix $\mathbf{A}$ and not on the righthand side $\mathtt{b}$. These operations turn out to be identical to factoring the matrix into the product of an upper-triangular matrix $\mathbf{U}$ and a lower-triangular matrix $\mathbf{L}$ so that $\mathbf{A} = \mathbf{LU}$. *LU* factorization algorithms solve linear matrix equations by first factoring the matrix into its $\mathbf{L}$ and $\mathbf{U}$ factors and then solving two linear equations with the triangular matrices $\mathbf{L}$ and $\mathbf{U}$.

The factorization step accounts for the vast majority of the required calculations. Assuming no sparsity in the matrix $\mathbf{A}$, the number of operations in the factorization step scales like $N^3$ while those for the triangular solves scale like $N^2$. The advantage of *LU* factorization comes in to play when linear equations with the same matrix $\mathbf{A}$ must be solved many times. The *LU* factors can be reused each time so that the cost of solving linear equations with the same matrix multiple times is relatively low.

Writing *LU* factorization algorithms for sparse matrices is very difficult because

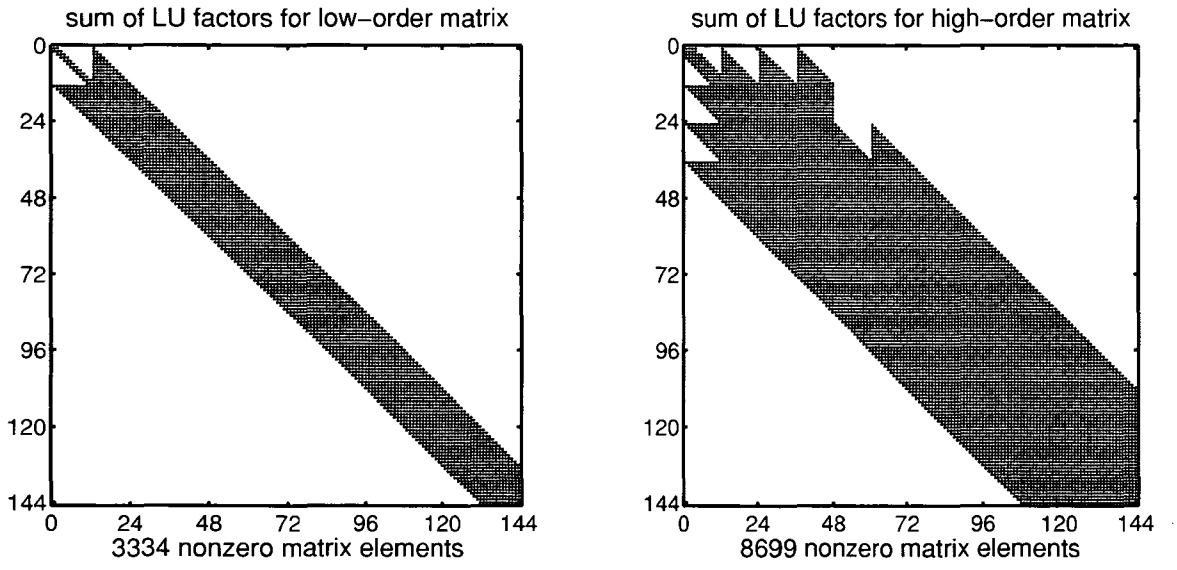


Figure D.2: Sparsity structure of the $LU$ factors of the matrices in Figure D.1. The factors $U$ and $L$ are upper and lower-triangular matrices, respectively. The sparsity of the sum $L + U$ is shown here.

the **L** and **U** matrices will not have the same sparsity structure as **A**. In general, the combination of **L** and **U** will have many more nonzero matrix elements than **A**. Figure D.2 shows the sparsity structure of $\mathbf{L} + \mathbf{U}$ for both matrices pictured in Figure D.1. Basically, factorization has filled in all of the zeros between the outermost nonzero diagonals. This is typical of the "fill" that occurs in $LU$ factorization. Storing the $LU$ factors requires significantly more computer memory for the high-order than for the low-order finite difference matrix.

Currently, the only available software package that can $LU$ factor a sparse matrix with complex matrix elements is SuperLU [19] written by Xiaoye "Sherri" Li. This package takes a matrix stored in the packed array storage scheme described previously and decomposes it into its **L** and **U** factors that are also stored as sparse matrices. It then performs triangular solves with these factors to solve the original matrix equation. SuperLU is parallelized so that it can simultaneously utilizes several CPUs on a massively parallel computer. Also, SuperLU includes a re-ordering step which permutes the matrix **A** in such way as to reduce the amount of storage required for the $LU$ factors. Some time and memory usage information with the two types of finite difference matrices are listed in Figure E.1.

**Simplistic Algorithm for Storing a Sparse Matrix**

N = dimension of matrix

dimension of storage arrays:

(integer nnz is the number of nonzero matrix elements)

**integer** rowind(1:nnz)

**integer** colptr(0:N)

**complex** values(1:nnz)

nnz = 0

$$\text{colptr}(0) = \begin{cases} 1 & \text{one-based indexing} \\ 0 & \text{zero-based indexing} \end{cases}$$

**for** $j = 1$ to N

colptr($j$) = 0

**for** $i = 1$ to N

compute $\mathbf{A}(i, j)$

**if** abs($\mathbf{A}(i, j)$) $> 0$ **then**

nnz = nnz + 1

values(nnz) = $\mathbf{A}(i, j)$

$$\text{rowind(nnz)} = \begin{cases} i & \text{one-based indexing} \\ i - 1 & \text{zero-based indexing} \end{cases}$$

colptr($j$) = colptr($j$) + 1

**endif**

**end**

colptr($j$) = colptr($j$) + colptr($j - 1$)

**end**

Figure D.3: SuperLU uses a packed storage scheme that stores only the nonzero elements of a matrix. This simplistic algorithm will create the appropriate packed storage structure for any matrix. It is extremely inefficient because it loops over every matrix element (including those that are zero) and is provided for illustrative purposes only. In practice, the loop structure should be designed so that the algorithm tests only those matrix elements which are expected to be nonzero.

# Appendix E

# Conjugate Gradient Squared Iterative Algorithm

The conjugate gradient squared (CGS) iterative algorithm was used to solve the linear equations arising from the scattered wave equation. Iterative algorithms attempt to arrive at a solution to a linear system $\mathbf{Ax} = \mathbf{b}$ using a series of matrix-vector multiplies rather than by using a "direct" method such as Gaussian elimination. If an iterative algorithm converges for some matrix $\mathbf{A}$ then it may require significantly less computer time and memory than do direct methods. However, iterative algorithms are guarunteed to converge to the solution only for certain special cases. For "ill-conditioned" matrices, such as those produced by exterior complex scaling, another matrix $\mathbf{M}$ is needed as a "pre-conditioner" to make iterative algorithms converge.

## E.1 Convergence of iterative algorithms

The measure of an iterative algorithm's effectiveness is the rate at which it converges (assuming that it does converge) to the correct solution. Let $\mathbf{x}^{(i)}$ be the approximate solution vector computed in the $i^{th}$ iteration. To measure how close $\mathbf{x}^{(i)}$ is to the exact solution we substitute it for $\mathbf{x}$ in the system of equations $\mathbf{b} - \mathbf{Ax} = 0$. The norm of the residual $\mathbf{r}^{(i)} \equiv \mathbf{b} - \mathbf{Ax}^{(i)}$ will be zero if $\mathbf{x}^{(i)}$ is the exact solution.

$$\text{error} = \left\|\mathbf{r}^{(i)}\right\| = \left\|\mathbf{b} - \mathbf{Ax}^{(i)}\right\| \tag{E.1}$$

The rate of convergence is then the rate at which $\left\|\mathbf{r}^{(i)}\right\|$ approaches zero. Iterative algorithms are preferable to Gaussian elimination if they converge and the rate of convergence is reasonably fast.

For a system of $N$ linear equations the number of numerical operations required for a matrix-vector multiply scales as $N^2$ while Gaussian elimination scales as $N^3$. Thus, if the number of matrix-vector multiplies required for the iterative solution does not increase significantly with increasing $N$ then it is guarunteed that for sufficiently large $N$ an iterative algorithm will take less time than Gaussian elimination. The time savings are even more significant if the matrix is sparse *i.e.*, most of the matrix

elements are zero. Calculating the matrix-vector product $\mathbf{Ax}$ for a sparse matrix $\mathbf{A}$ requires many fewer numerical operations. In the case of a finite difference matrix, the number of nonzero matrix elements per row is fixed and the matrix-vector multiply scales linearly with $N$.

Krylov subspace methods are a class of iterative algorithms designed to rapidly converge to a solution. The most efficient and best understood of these algorithms is the conjugate gradient (CG) method (see, for example, reference [16] section 6.6.3). The CG method is guarunteed to converge only for symmetric, positive definite matrices. The finite difference matrix representation of $(E - \hat{H})$ with exterior complex scaling is complex non-symmetric and non-Hermitian. There are several Krylov subspace methods designed for this more general class of matrices. Whether or not these methods work for a particular matrix and how fast they converge depends on the eigenvalue spectrum of the matrix and cannot, in general, be predicted. If the spectrum covers a large region in the complex plane then an iterative algorithm will converge slowly or possibly not at all. Such a matrix is said to be "ill-conditioned".

## E.2 Pre-conditioners

If a matrix $\mathbf{A}$ is ill-conditioned then an iterative algorithm might be made to converge or to converge more rapidly by using a "pre-conditioner" matrix $\mathbf{M}$ chosen so that the matrix product $\mathbf{M}^{-1}\mathbf{A}$ is better conditioned than the matrix $\mathbf{A}$. The solution to $\mathbf{Ax} = \mathbf{b}$ is then obtained by instead solving the pre-conditioned equation $\mathbf{M}^{-1}\mathbf{Ax} = \mathbf{M}^{-1}\mathbf{b}$. Within the algorithms the pre-conditioner is actually applied by solving linear equations with the matrix $\mathbf{M}$ rather than $\mathbf{A}$. In order for a pre-conditioned iterative algorithm to still be preferable to Gaussian elimination it is necessary that solving linear systems with the matrix $\mathbf{M}$ require significantly fewer computations than solving linear systems with $\mathbf{A}$. We can see how this works by looking at a very simple (not a Krylov subspace method) iterative algorithm.

In this simple example we start with an initial guess of zero *i.e.*, $\mathbf{x}^{(0)} = 0$. At each iteration we update the approximate solution vector by adding the residual vector.

$$\mathbf{x}^{(i+1)} = \mathbf{x}^{(i)} + \mathbf{r}^{(i)} = \mathbf{b} + (1 - \mathbf{A})\,\mathbf{x}^{(i)} \tag{E.2}$$

In this case we can write down an exact algebraic expression for the $i^{th}$ solution vector and the $i^{th}$ residual vector.

$$\mathbf{r}^{(i)} = (1 - \mathbf{A})^i\,\mathbf{b} \tag{E.3}$$

Clearly this algorithm will converge if and only if the eigenvalues of $\mathbf{A}$ lie inside a unit circle centered at 1. To remove this restriction we instead solve the pre-conditioned equation $\mathbf{M}^{-1}\mathbf{Ax} = \mathbf{M}^{-1}\mathbf{b}$. By appropriate substitution into Equation E.3 we directly write down an algebraic solution for the $i^{th}$ residual vector in this case.

$$\mathbf{r}^{(i)} = \left(1 - \mathbf{M}^{-1}\mathbf{A}\right)^i \mathbf{M}^{-1}\mathbf{b} \tag{E.4}$$

Now the requirement for convergence is that the eigenvalues of the matrix product $\mathbf{M}^{-1}\mathbf{A}$ lie within a unit circle centered at 1. In other words, we require that $\mathbf{M} \approx \mathbf{A}$.

The degree to which $\mathbf{M}$ approximates $\mathbf{A}$ determines the rate of convergence of the simple algorithm. If $\mathbf{M}$ were exactly equal to $\mathbf{A}$ then the algorithm would converge in just one iteration, but it would reduce to a direct solution of the original matrix equation so no savings in time or memory would have been achieved. The goal is to find a pre-conditioner $\mathbf{M}$ that produces a reasonable rate of convergence but for which solving linear systems with $\mathbf{M}$ is substantially easier than solving linear systems with $\mathbf{A}$. For Krylov subspace methods the effect of the pre-conditioner is more complicated, but the basic ideas are the same. In general, choosing $\mathbf{M}$ to approximate $\mathbf{A}$ is one way, but not the only way, to form a pre-conditioner.

## E.3 Conjugate gradient squared for ECS

The eigenvalue spectrum of an exterior complex scaled Hamiltonian populates much of the lower half of the complex plane. Thus, the matrix representation of $\left(E - \hat{H}\right)$ is very ill-conditioned and finding an iterative method that will solve the scattered wave equation involves testing various algorithms and pre-conditioners to see which converge. Various iterative algorithms were tested with one-dimensional potential scattering problems such as those in Appendix A. Exterior complex scaled finite difference matrices for a one-dimensional problem are relatively simple and small but they are ill-conditioned in the same manner as the Temkin-Poet matrices of Chapter 3 and the electron-Hydrogen matrices of Chapter 5.

Every known iterative algorithm failed to converge for these test problems without pre-conditioning. Furthermore, all pre-conditioners created by standard methods in numerical linear algebra failed to cause any of the iterative algorithms to converge. The only successful pre-conditioner was the low-order finite difference matrix representation of the same operator. Using the low-order matrix as a pre-conditioner for solving the high-order matrix equation caused a few of the Krylov subspace methods (CGS, Bi-CGStab, and GMRES) to converge.

All had about the same stability and convergence rate when using this pre-conditioner. In fact, this pre-conditioner caused even the simple iterative algorithm in the previous section to converge, although much more slowly than the Krylov subspace methods. The CGS algorithm, given in Figure E.2 on page 116, was chosen because it required the least amount of computer memory to implement.

Solving the scattered wave equation (Equation 3.5) for the Temkin-Poet model problem is a more concrete and pertinent example. Let the matrix $\mathbf{A}$ represent the two-dimensional operator $\left(E - \hat{H}\right)$ using "high-order", 7-point finite difference formulas for the second derivatives and let the matrix $\mathbf{M}$ be the "low-order", 3-point finite difference representation of the same operator. The driving vector `b` is the function $\left(\hat{H} - E\right)\psi^0_{k_i}$ evaluated on the grid. The vector `x` will be the scattered wave $\psi^+_{\mathrm{TP}}$ on the grid, we'll choose $\mathbf{x}^{(0)} = 0$ as the starting guess for the iterative algorithm.

As shown in Figure E.1, the rate of convergence for the algorithm in Figure E.2 applied to the Temkin-Poet mode is fairly rapid and well-behaved. Each CGS iteration requires two matrix-vector multiplies with the matrix $\mathbf{A}$ and two applications of the pre-conditioner $\mathbf{M}$. The matrix-vector multiplies were performed without explic-

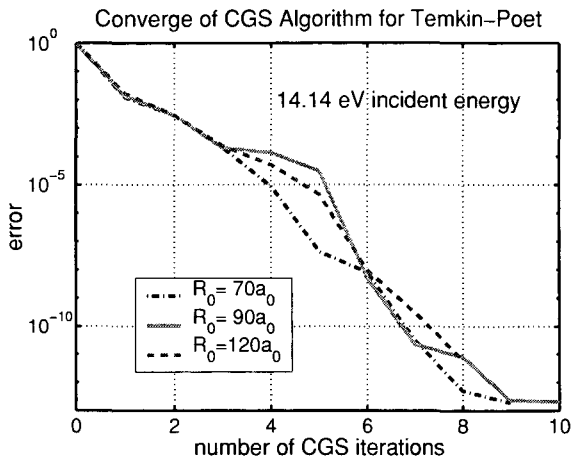


Iterative Algorithm

| | | |
|---|---|---|
| factorization time: | 379.4 | seconds |
| single solve time: | 5.51 | seconds |
| solves required: | 14 | |
| iteration time: | 85.9 | seconds |
| total time: | 464 | seconds |

Direct Solution

| | | |
|---|---|---|
| factorization time: | 1464 | seconds |
| solve time: | 12.9 | seconds |
| total time: | 1477 | seconds |

Figure E.1: Convergence of the CGS algorithm for the Temkin-Poet model for three grids which are real out to different values of $R_0$ is shown on the left. The time required for the $R_0 = 70a_0$ calculation on a 332Mhz Power2 CPU is shown on the top right. In this case, the grid extends to $95a_0$ and the total number of grid points (and matrix dimension) is 114,244. The pre-conditioner is applied by first factoring the matrix $\mathbf{M}$ and then solving with the $LU$-factors twice in each CGS iteration. So, the total number of solves is twice the number of iterations. The time required to factor the matrix $\mathbf{A}$ and solve $\mathbf{Ax} = \mathtt{b}$ directly is shown on the bottom right.

itly storing $\mathbf{A}$. This provides a significant savings in memory compared to a direct solution which requires enough memory to both store the matrix and perform Gaussian elimination. Application of the pre-conditioner means solving linear equations with the matrix $\mathbf{M}$. Here we have no choice but to solve the system directly. This is done via an $LU$-factorization (see Appendix D) of $\mathbf{M}$. By saving the $LU$ factors of $\mathbf{M}$ repeated applications of the pre-conditioner are fairly inexpensive.

For comparison, the time required for a direct solution via an $LU$-factorization of $\mathbf{A}$ is also shown. In this example the iterative solution took 31% of the time that the direct solution did. This is because the factorization of $\mathbf{M}$ takes significantly less time than does the factorization of $\mathbf{A}$. A single solve using the $LU$ factors takes much less time for $\mathbf{M}$ than for $\mathbf{A}$. However, the total time spent in the CGS algorithm *after* the $LU$-factorization of $\mathbf{M}$ is larger than the solve time using the $LU$ factors of $\mathbf{A}$. This means that if many solutions to an equation of the form $\mathbf{Ax} = \mathtt{b}$ are required then the iterative algorithm is actually more time consuming than direct solution. However, there is still a significant savings in memory using the iterative algorithm.

**Preconditioned Conjugate Gradient Squared Method**

Start with initial guess $\mathbf{x}^{(0)}$

Compute $\mathbf{r}^{(0)} = \mathbf{b} - \mathbf{A}\mathbf{x}^{(0)}$

**for** $i = 1$ to max_iterations

  $\rho_{i-1} = \mathbf{b}^T \mathbf{r}^{(i-1)}$

  **if** $\rho_{i-1} = 0$ method fails

  **if** $i = 1$ **then**

    $\mathbf{u}^{(1)} = \mathbf{r}^{(0)}$

    $\mathbf{p}^{(1)} = \mathbf{r}^{(0)}$

  **else**

    $\beta_{i-1} = \rho_{i-1}/\rho_{i-2}$

    $\mathbf{u}^{(i)} = \mathbf{r}^{(i-1)} + \beta_{i-1}\mathbf{q}^{(i-1)}$

    $\mathbf{p}^{(i)} = \mathbf{u}^{(i)} + \beta_{i-1}\left(\mathbf{q}^{(i-1)} + \beta_{i-1}\mathbf{p}^{(i-1)}\right)$

  **endif**

  solve $\mathbf{M}\hat{\mathbf{p}} = \mathbf{p}^{(i)}$

  $\hat{\mathbf{v}} = \mathbf{A}\hat{\mathbf{p}}$

  $\alpha_i = \rho_{i-1}/\mathbf{b}^T\hat{\mathbf{v}}$

  $\mathbf{q}^{(i)} = \mathbf{u}^{(i)} - \alpha_i\hat{\mathbf{v}}$

  solve $\mathbf{M}\hat{\mathbf{u}} = \mathbf{u}^{(i)} + \mathbf{q}^{(i)}$

  $\mathbf{x}^{(i)} = \mathbf{x}^{(i-1)} + \alpha_i\hat{\mathbf{u}}$

  $\mathbf{r}^{(i)} = \mathbf{b} - \mathbf{A}\mathbf{x}^{(i)}$

  error $= \|\mathbf{r}^{(i)}\|$

  **if** error $<$ tolerance **exit**

**end**

Figure E.2: The preconditioned conjugate gradient squared algorithm based on the one given in *Templates for the Solution of Linear Sytems* [4], page 26. The arbitrary vector $\tilde{\mathbf{r}}$ in [4] is defined here to be the driving term $\mathbf{b}$. Also the full residual $\mathbf{r}^{(i)}$ is computed in each iteration rather than updating the previous residual.

# Appendix F

# Expansions in Spherical Harmonics

The calculations described in this dissertation all involved partial wave expansions of wave functions in terms of spherical harmonics. Some properties of both the ordinary and coupled spherical harmonics that are important to the derivations presented in the preceding chapters are given in this appendix.

## F.1 Spherical Harmonics

One-electron functions are expanded in terms of ordinary spherical harmonics $\mathrm{Y}_{l,m}$ defined in Equations F.1 and F.2 where the $P_l^m$ are associated Legendre functions.

$$\mathrm{Y}_{l,m}(\theta,\phi) \equiv (-1)^m \sqrt{\tfrac{(2l+1)(l-m)!}{4\pi(l+m)!}} P_l^m(\cos\theta) e^{im\phi} \quad , \qquad m \geq 0 \tag{F.1}$$

$$\mathrm{Y}_{l,m}(\theta,\phi) \equiv (-1)^m \mathrm{Y}^{\star}_{l,-m}(\theta,\phi) \tag{F.2}$$

The $\mathrm{Y}_{l,m}(\theta,\phi)$ are orthonormal functions of the usual spherical polar angles $\theta$ and $\phi$ and are eigenfunctions of the total angular momentum quantum number $l$ and its projection $m$ along the $z$ axis.

$$\nabla^2 \left(f(r)\mathrm{Y}_{l,m}(\theta,\phi)\right) = \left(\frac{l(l+1)}{r^2} f(r) - \frac{1}{r}\frac{\partial^2}{\partial r^2}\left(r f(r)\right)\right) \mathrm{Y}_{l,m}(\theta,\phi) \tag{F.3}$$

Two-electron functions are expanded in terms of coupled spherical harmonics $\mathcal{Y}^{LM}_{l_1,l_2}(\theta_1,\phi_1,\theta_2,\phi_2)$ that are functions of two spherical polar angles for each electron.

$$\mathcal{Y}^{LM}_{l_1,l_2}(\theta_1,\phi_1,\theta_2,\phi_2) = \sum_{m_1,m_2} \langle l_1 l_2 m_1 m_2 | LM \rangle \mathrm{Y}_{l_1 m_1}(\theta_1,\phi_1) \mathrm{Y}_{l_2 m_2}(\theta_2,\phi_2) \tag{F.4}$$

The $\mathcal{Y}^{LM}_{l_1,l_2}$ can be written as a finite sum of products of $\mathrm{Y}_{l,m}$, as shown in Equation F.4, where the $\langle l_1 l_2 m_1 m_2 | LM \rangle$ are the well-known Clebsch-Gordan coefficients. Procedures for calculating Clebsch-Gordan coefficients can be found in standard references such as Messiah [21] and Zare [39].

From Equation F.4, it is obvious that the $\mathcal{Y}^{LM}_{l_1,l_2}$ are eigenfunctions of the individual angular momenta $l_1$ and $l_2$ for each electron. Clebsch-Gordan coefficients are real

numbers chosen so the $\mathcal{Y}^{LM}_{l_1,l_2}$ are also orthonormal eigenfunctions of the total angular momentum $L$ of the two-electron system and its projection $M$ along the $z$ axis.

$$\langle l_1' l_2' L' M' | l_1 l_2 L M \rangle = \delta_{l_1',l_1} \delta_{l_2',l_2} \delta_{L',L} \delta_{M',M} \tag{F.5}$$

The orthonormality of the $\mathcal{Y}^{LM}_{l_1,l_2}$ is expressed in Equation F.5 using Dirac braket notation with the scalar product denoting integration over all four angular coordinates.

Clebsch-Gordan coefficients are zero unless $m_1 + m_2 = M$. So, the double sum over $m_1$ and $m_2$ in Equation F.4 could be rewritten as a single sum over either $m_1$ or $m_2$. Also, only terms for which $|m_1| \leq l_1$ and $|m_2| \leq l_2$ are nonzero. These restrictions can be used to specify the summation limits.

In this dissertation only $M = 0$ partial waves were necessary. For these coupled spherical harmonics the expansion in Equation F.4 can be simplified.

$$\mathcal{Y}^{L0}_{l_1,l_2}(\theta_1, \phi_1, \theta_2, \phi_2) = \sum_m \langle l_1 l_2 m - m | L M \rangle \mathrm{Y}_{l_1 m}(\theta_1, \phi_1) \mathrm{Y}_{l_2 - m}(\theta_2, \phi_2) \tag{F.6}$$

The limits in the summation over $m$ in Equation F.6 are $\pm\min(l_1, l_2)$. We can see the cylindrical symmetry in an $M = 0$ system (such as an electron scattering from a spherically symmetric target) by using the explicit forms for the $\mathrm{Y}_{l,m}$ from Equations F.1 and F.2 in Equation F.6. Dependence on the azimuthal angles $\phi_1$ and $\phi_2$ in the $m^{th}$ term simplifies to $e^{im\Delta\phi}$ where $\Delta\phi \equiv \phi_1 - \phi_2$. The $\mathcal{Y}^{L0}_{l_1,l_2}$ are not functions of the $\phi_1$ and $\phi_2$ independently. Instead, they are functions of the relative angle $\Delta\phi$.

Clebsch-Gordan coefficients obey the following symmetry relation with respect to interchange of the single-particle quantum numbers.

$$\langle l_1 l_2 m_1 m_2 | L M \rangle = (-1)^{l_1 + l_2 + L} \langle l_2 l_1 m_2 m_1 | L M \rangle \tag{F.7}$$

An important symmetry relation for the $\mathcal{Y}^{LM}_{l_1,l_2}$ follows immediately from Equation F.7 and the expansion in Equation F.4.

$$\mathcal{Y}^{LM}_{l_1,l_2}(\theta_2, \phi_2, \theta_1, \phi_1) = (-1)^{l_1 + l_2 + L} \mathcal{Y}^{LM}_{l_2,l_1}(\theta_1, \phi_1, \theta_2, \phi_2) \tag{F.8}$$

When the sum $l_1 + l_2 + L$ is even the $\mathcal{Y}^{LM}_{l_1,l_2}$ are said to have even parity and when it is odd they are said to have odd parity. This property is important because only partial waves with the same parity will be coupled by the two-electron potential.

## F.2 Two-Electron Potential

Of particular relevence to the topic of this dissertation are matrix elements of the two-electron potential $\frac{e^2}{|\vec{r}_1 - \vec{r}_2|}$ between two $\mathcal{Y}^{L0}_{l_1,l_2}$.

$$\langle l_1 l_2 L0 | \frac{e^2}{|\vec{r}_1 - \vec{r}_2|} | l_1' l_2' L0 \rangle \equiv \int_{4\pi} \int_{4\pi} \mathcal{Y}^{L0}_{l_1,l_2}(\hat{r}_1, \hat{r}_2)^\star \frac{e^2}{|\vec{r}_1 - \vec{r}_2|} \mathcal{Y}^{L0}_{l_1',l_2'}(\hat{r}_1, \hat{r}_2) d\hat{r}_1 d\hat{r}_2 \tag{F.9}$$

These form the two-dimensional potentials in the coupled equations (Equation 5.6) and are functions of the radial coordinates $r_1$ and $r_2$. Formal expressions were worked out by Percival and Seaton [24] and are also given in Application 4 of Zare [39].

Deriving formulas for these matrix elements can be done using an expansion of $\frac{e^2}{|\vec{r}_1-\vec{r}_2|}$ that makes use of the spherical harmonic addition theorem.

$$\frac{e^2}{|\vec{r}_1-\vec{r}_2|} = e^2 \sum_{\lambda=0}^{\infty} \frac{r_<^\lambda}{r_>^{\lambda+1}} \left(\frac{4\pi}{2\lambda+1}\right) \sum_{q=-\lambda}^{\lambda} (-1)^q Y_{\lambda,-q}(\hat{r_1}) Y_{\lambda,q}(\hat{r_2}) \tag{F.10}$$

The radial dependence is then contained in the non-analytic factors $\frac{r_<^\lambda}{r_>^{\lambda+1}}$ where $r_>$ is the larger and $r_<$ is the smaller of $r_1$ and $r_2$. From Equation F.10 it is clear that the matrix elements have the following form, previously given in Equation 5.5.

$$\langle l_1 l_2 L0 | \frac{e^2}{|\vec{r}_1-\vec{r}_2|} | l_1' l_2' L0 \rangle = e^2 \sum_{\lambda} C^{L,\lambda}_{l_1 l_2 l_1' l_2'} \frac{r_<^\lambda}{r_>^{\lambda+1}} \tag{F.11}$$

The values of $\lambda$ over which the $C^{L,\lambda}_{l_1 l_2 l_1' l_2'}$ are nonzero range from $\max(|l_1-l_1'|, |l_2-l_2'|)$ to $\min((l_1+l_1'), (l_2+l_2'))$. Specifically, the $C^{L,\lambda}_{l_1 l_2 l_1' l_2'}$ are equal to the following integral.

$$C^{L,\lambda}_{l_1 l_2 l_1' l_2'} = \sum_{q=-\lambda}^{\lambda} (-1)^q \int_{4\pi}\int_{4\pi} \mathcal{Y}^{L0}_{l_1,l_2}(\hat{r}_1,\hat{r}_2)^\star Y_{\lambda,-q}(\hat{r_1}) Y_{\lambda,q}(\hat{r_2}) \mathcal{Y}^{L0}_{l_1',l_2'}(\hat{r}_1,\hat{r}_2) d\hat{r}_1 d\hat{r}_2 \tag{F.12}$$

This integral can be expressed in terms of Clebesch-Gordan coefficients and the so-called Racah coefficients [24]. These formulas will not be given here, but one consequence of the Clebesch-Gordan factors involved is that matrix elements between $\mathcal{Y}^{LM}_{l_1,l_2}$ of different parity (see Equation F.8) are zero. For this reason, there is no coupling between partial waves of different parity. One special case where we can easily evaluate Equation F.11 is when all quantum numbers are zero. This gives the two-electron potential used in the Temkin-Poet model.

$$\langle 0000 | \frac{e^2}{|\vec{r}_1-\vec{r}_2|} | 0000 \rangle = \frac{e^2}{r_>} \tag{F.13}$$

## F.3 Partial wave expansions

We use the various spherical harmonics for partial wave expansions of the wave functions. The multipole expansion of a plane wave is expanded in terms of the ordinary spherical harmonics.

$$e^{ik_i z} = \sum_{l=0}^{\infty} i^l \sqrt{4\pi(2l+1)} \frac{\hat{j}_l(k_i r)}{k_i r} Y_{l0}(\hat{r}) \tag{F.14}$$

The $\hat{j}_l$ are regular Riccati-Bessel functions. By choosing the momentum vector to be along the $z$ axis, only terms for which $m = 0$ are included in the expansion.

Next we will consider the type of partial wave expansion needed for the "initial state" $\Psi^0_{k_i}(\vec{r}_1,\vec{r}_2)$ defined in Equation 2.5. This wave function is made of two terms with the form $e^{ik_i z_1} f(r_2)$ where $f$ has no angular dependence. To expand a function

like this, it is necessary to evaluate Clebsch-Gordan coefficients for the cases where either $l_1$ or $l_2$ is equal to $L$ and the other is zero.

$$\langle L0M0|LM\rangle = \langle 0L0M|LM\rangle = 1 \tag{F.15}$$

An immediate consequence of Equation F.15 is that the $\mathcal{Y}^{LM}_{l_1,l_2}$ with either $l_1$ or $l_2$ equal to $L$ have a very simple form.

$$\mathcal{Y}^{LM}_{L,0}(\hat{r_1},\hat{r_2}) = \mathrm{Y}_{LM}(\hat{r_1})\mathrm{Y}_{00}(\hat{r_2}) \qquad \mathcal{Y}^{LM}_{0,L}(\hat{r_1},\hat{r_2}) = \mathrm{Y}_{00}(\hat{r_1})\mathrm{Y}_{LM}(\hat{r_2}) \tag{F.16}$$

Since $\mathrm{Y}_{0,0}(\theta,\phi) = \frac{1}{\sqrt{4\pi}}$ we can write $f(r) = \sqrt{4\pi}f(r)\mathrm{Y}_{0,0}(\theta,\phi)$. Using Equations F.16 and F.14 it is trivial to write down the partial wave expansion of $e^{ik_iz_1}f(r_2)$ in terms of coupled spherical harmonics.

$$e^{ik_iz_1}f(r_2) = \sum_{L=0}^{\infty} i^L 4\pi\sqrt{(2L+1)}\frac{\hat{j}_L(k_ir_1)}{k_ir_1}f(r_2)\mathcal{Y}^{L0}_{L0}(\hat{r}_1,\hat{r}_2) \tag{F.17}$$

Only $M = 0$ terms are included in Equation F.17 because only $m = 0$ terms exist in the multipole expansion of the plane wave and in the function $f(r)$. This basic derivation leads directly from the definition of $\Psi^0_{k_i}$ in Equation 2.5 to its partial wave expansion in Equation 5.2.

One feature of Equation F.17 is that it contains only terms with even parity ($l_1 + l_2 + L = L + 0 + L = 2L$). Since the two-electron potential only couples partial waves with the same values of $L$ and $M$ and the same parity the scattered wave $\Psi^+_{\mathrm{sc}}$ will contain only terms with the parity and values of $L$ and $M$ that exist in the expansion of $\Psi^0_{k_i}$. For this reason, the partial wave expansion of $\Psi^+_{\mathrm{sc}}$ in Equation 5.3 contains only terms with $M = 0$ and for which $l_1 + l_2 + L$ is an even integer. Consequently, the symmetry relation given in Equation 5.8 for the partial wave radial functions in the expansion of $\Psi^+_{\mathrm{sc}}$ follows directly from Equation F.8.

ERNEST ORLANDO LAWRENCE BERKELEY NATIONAL LABORATORY
ONE CYCLOTRON ROAD | BERKELEY, CALIFORNIA 94720

Prepared for the U.S. Department of Energy under Contract No. DE-AC03-76SF00098